

On-line Nonlinear Characterization of Anisotropic Materials

Jan Wei Pan

Dissertation submitted to the faculty of the Virginia Polytechnic Institute and State University in partial fulfillment of the requirements for the degree of

Doctor of Philosophy
In
Mechanical Engineering

Tomonari Furukawa
Romesh C. Batra
John C. Duke
Daniel J. Inman
Ranga Pitchumani

December 20th, 2010
Blacksburg, VA

Keywords: On-line Characterization, Anisotropic Materials, Stochastic, Full-field Measurements, Nonlinear Behavior

Copyright 2010

On-line Nonlinear Characterization of Anisotropic Materials

Jan Wei Pan

ABSTRACT

This dissertation proposes a new framework to characterize the nonlinear behavior of anisotropic materials in an on-line manner. The proposed framework applies recursive estimation and a multi-linear model to characterize the nonlinear behavior of anisotropic materials on-line using full-field strains, which are capable of capturing the multi-axial information of anisotropic materials.

A stochastic method is developed to characterize the linear behavior of anisotropic materials under the influence of full-field strain measurement noise. This method first derives stochastic equations based on the formulas of energy-based characterization that utilizes the principle of energy conservation, and then recursively estimates elastic constants at every acquisition of measurement using a Kalman filter (KF). Since the measurement model is expressed nonlinearly, the KF utilizes a Kalman gain, which is newly derived in this dissertation through variance minimization, to achieve optimal characterization. The aforementioned method, namely stochastic linear characterization in this dissertation, becomes a basis of the multi-linear characterization method. This method utilizes a multi-linear model, which is defined by partitions, to characterize the nonlinear constitutive relations. The multi-linear characterization scales up the number of estimates and identifies the coefficients of each linear partition using the previously derived KF. The recursive updates in measurements not only removes uncertainty through sensor measurements, but also enables the on-line capability of the nonlinear characterization of anisotropic materials.

A series of numerical and experimental studies were performed to demonstrate the performance of the proposed framework in characterizing the nonlinear behavior of anisotropic materials. The validity and applicability of the proposed framework were confirmed by the comparison with the known values of the characterized constitutive relations. It was found that the proposed framework identified elastic constants that were in good agreement with known values irrespective of the specimen geometry. The results of the multi-linear characterization method were well correlated with known nonlinear stress-strain relations and concluded that the proposed framework is capable of characterizing adequate nonlinear behavior on-line.

Acknowledgement

Prof. Tomonari Furukawa has been a strong and supportive advisor throughout my graduate school career. He has always taken time to introduce me to people within the discipline; has always shown faith in my work and has always been a strong advocate for me. Tomo, I owe you my deepest gratitude for being my advisor. There are simply no words to express the gratitude I feel for the persistent guidance and advice you have given during my study. I thank you with all my heart.

I am also indebted to Drs John Michopoulos, Athanasios Iliopoulos and John Hermanson for their invaluable time and great advices to my questions during my visits to NRL. Your feedback and discussions have lifted conceptual issues into the realm of practicality. I would like to thank my committee members, Professors Dan Inman, Romesh Batra, John Duke and Ranga Pitchumani, who have been always there to listen and give advice. I am deeply grateful for our discussions that helped me sort out the technical details of my work.

I especially thank Dr. Jinquan Cheng for his patience, warmth, and for helping me with the discipline of my writings and critical thinking skills. Drs. Hou Man and Shen Hin Lim set a great example of grace and good humor and I thank you both for welcoming me during odd hours on many occasions for discussions. I have been especially fortunate to get to know Dr. Heather Chemistruck, Joshy Caffee and William Kirchner. Your various forms of support during my graduate study have been great assets to me. On top of that, I greatly value Zach, Willie, Shawn, Gordon, Alex Y., Xianqiao, Sreenath, Drs. Chung, Mak and Kellermann for their friendships.

I am also thankful to the Furukawa Family for letting my wife and me to stay with them when we first came to the States. Thank you, Tomomi, Minami and Kasumi for the warmth and enjoyable moments at Danville. I am very fortunate to meet the Smith family, who has been treating my wife and I being part of the family. Thank you, Charlotte, Tim, Sarah, Mandy, Jess and Trey, for all the heartfelt prayers and blessings.

Finally, I appreciate the financial support from the Program Managers, Dr. Ignacio Perez from ONR and Ms. Diane Hoyns from NAVAIR, who have funded the research discussed in this dissertation.

Dedication

This dissertation is dedicated to my parents, Sze Kim Pan and Toe Boi Chan, who brought me up with their endless love and encouraged me to pursue advanced degrees; my elder sister and brother, Yet Ping Pan and Jan Lik Pan, for their concern and caring during difficult times; and most importantly to my wife, Swee Lee Low, who has accompanied me through the tough times with her love, sacrifice, unlimited patience and kind indulgence. Without their continuing support, I would never be able to accomplish this work.

Table of Contents

Abstract.....	ii
Acknowledgement	iii
Dedication	iv
Table of Contents	v
List of Figures.....	viii
List of Tables	xi
Nomenclature	xiii
Chapter 1 Introduction.....	1
1.1 Background.....	2
1.2 Objective.....	4
1.3 Approach	4
1.4 Principal Contributions.....	6
1.5 Publications	6
1.6 Organization	9
Chapter 2 Literature Review	11
2.1 On-line Evaluation based on Vibration Testing	11
2.2 Nonlinear Characterization based on Mechanical Testing	14
2.3 Characterization based on Full-field Measurements	18
2.4 Implicit Modeling of Nonlinear Behavior	21
2.5 Summary.....	23
Chapter 3 Energy-based Characterization and Full-field Measurements	25
3.1 Derivation of Energy-based Characterization	26
3.1.1 Elastic Moduli of Anisotropic Materials	26
3.1.2 Principle of Energy Conservation	28
3.2 Full-field Measurements.....	31
3.2.1 Homography Transformation.....	32

3.2.2 Full-field Displacements and Strains	33
3.3 Deterministic Energy-based Characterization Approach	34
3.3.1 Pseudo-inverse Calculation	34
3.3.2 Quantification.....	35
3.3.3 Process Diagram.....	36
3.4 Summary.....	37
Chapter 4 Stochastic Linear Characterization of Anisotropic Materials.....	38
4.1 State Transition Model and Measurement Model	39
4.2 Prediction and Correction.....	40
4.3 Numerical Implementation	42
4.4 Numerical Examples.....	43
4.4.1 Concept Proving by Algebraic Problem.....	43
4.4.2 Identification of Elastic Constants	51
4.5Summary.....	55
Chapter 5 Multi-camera Data Fusion for Probabilistic Full-field Measurements	56
5.1 Product of Gaussian Distributions	57
5.2 Propagation of Uncertainties	59
5.3 Numerical Implementation	62
5.4 Numerical Studies.....	63
5.4.1 Concept Proving of Full-field Measurements	63
5.4.2 Application to the Characterization of Anisotropic Materials	70
5.5 Summary.....	75
Chapter 6 Stochastic Multi-linear Characterization of Anisotropic Materials	76
6.1 Nonlinear Energy-based Characterization Framework	77
6.1.1 Multi-linear Constitutive Model.....	77
6.1.2 Principle of Energy Conservation	80
6.2 Stochastic Estimation using Kalman Filter.....	82
6.2.1 State Transition and Measurement Models	82
6.2.2 Prediction and Correction.....	82

6.2.3 Quantification.....	83
6.3 Numerical Studies.....	84
6.3.1 Estimation of Multi-linear Coefficients (Example 1)	85
6.3.2 Certainty of Multi-linear Coefficients under Various Noises (Example 2)	89
6.4 Summary.....	90
Chapter 7 Experimental Studies.....	92
7.1 Experimental Characterization Procedures	92
7.1.1 System	94
7.2 Experimental Results.....	95
7.2.1 Stochastic Linear Characterization (Experiment 1)	95
7.2.2 Stochastic Multi-linear Characterization (Experiment 2)	105
7.3 Summary.....	109
Chapter 8 Conclusions and Future Work	111
8.1 Conclusions	111
8.2 Future Work.....	113
8.3 Closing remarks	114
Bibliography	115
Appendix 1 Kalman Filter.....	126
A1.1 State Transition Model and Measurement Model	126
A1.2 Prediction.....	126
A1.3 Correction	127
Appendix 2 Experimental Modules.....	130
A2.1 Preprocessing Module	130
A2.2 Full-field Measurement Module	130

List of Figures

Figure 1 Elastic body subjected to surface force f_i	28
Figure 3 Specimen deformed from time step 1 to time step k	32
Figure 4 Schematic diagram of the deterministic energy-based characterization process.	37
Figure 5 Numerical implementation of the stochastic linear characterization method.	43
Figure 6 Transition of constants identified by the characterization method and the deterministic approach.....	46
Figure 7 Covariance updated by the Kalman gain.....	46
Figure 8 RMS distribution at different noise amplitudes by the characterization method.	48
Figure 9 RMS distribution with different noise amplitudes by the conventional deterministic approach.....	48
Figure 10 Distribution of mean and variance computed with different prior means.....	50
Figure 11 Distribution of mean and variance computed with different prior variances.....	51
Figure 12 Experimental setup.	52
Figure 13 Elastic constants identified.	54
Figure 14 Variances computed.	54
Figure 15 Schematic diagram of the multi-camera data fusion setup.....	57
Figure 16 Numerical implementation of the data fusion technique.....	63
Figure 17 Specimen configuration for concept proving.	64
Figure 18 Comparison of full-field displacement measurements at the gauge location.	65
Figure 19 Comparison of full-field strain measurements at the gauge location (Test 1).	66
Figure 20 Error of gauge location from multiple cameras with different covariance, $\forall l \in \{1, \dots, 50\}$ (Test 2).	67
Figure 21 Case studies of the estimated means of fused full-field displacement measurements at the gauge location (Test 3).....	68
Figure 22 Case studies of the estimated means of fused full-field strain measurements at the gauge location (Test 3).....	68

Figure 23 Propagated variance of displacement in all three cases, $\forall i \in \{x, y\}$ (Test 3).....	69
Figure 24 Propagated variance of full-field strain in all three cases (Test 3)	69
Figure 25 Propagated variance, $P_{g_i}^k, \forall i \in \{1, \dots, 4\}$, in all three cases (Test 3).....	70
Figure 26 Specimen configuration for the estimation of elastic constants.	71
Figure 27 Comparison of measured full-field displacements at gauge locations.	72
Figure 28 Comparison of measured full-field strains at gauge locations.	73
Figure 29 Elastic constants identified and compared.	74
Figure 30 Variance computed and compared.	74
Figure 31 Schematic diagram of the multi-linear partitions on each material axis of an element e in a deforming elastic body.....	77
Figure 32 Boundary conditions and geometry details of the AS4D/9310 specimen.....	85
Figure 33 Transition of the estimated multi-linear coefficients using 3 partitions.....	87
Figure 34 Diagonal terms of estimated covariance of multi-linear coefficients.....	88
Figure 35 Comparison of the estimated stress-strain relations and the differential entropy of the first example.....	89
Figure 36 Comparison between the error analysis and information entropy of the estimation results at the 200 th step.....	90
Figure 37 Overview of the experimental characterization procedures.	93
Figure 38 Developed experimental system for the proposed on-line nonlinear framework.....	95
Figure 39 Types of specimen shape used in mechanical tests: Open-hole (Test 1), Single-notch (Test 2) and Double-notch (Test 3).....	96
Figure 40 Boundary conditions of the specimen and the comparison between the measured force-displacement data and the FEA solutions.	97
Figure 41 Test 1: Full-field measurements (left) and FEA solutions (right) after 83 loading steps, and the transition of computed strain variances.....	98
Figure 42 Test 2: Full-field measurements (left) and FEA solutions (right) after 89 loading steps, and the transition of computed strain variances.....	99
Figure 43 Test 3: Full-field measurements (left) and FEA solutions (right) after 91 loading steps, and the transition of computed strain variances.....	99

Figure 44 Transition of the estimated mean.	101
Figure 45 Differential entropy of each test.	101
Figure 46 Transition of the estimated elastic moduli (Experiment 1).	102
Figure 47 Performance of the proposed framework under different standard deviation of strains after 100 measurements.	104
Figure 48 Deformed specimen and the boundary force-displacement of Experiment 2.	105
Figure 49 Full-field strain measurements after 190 measurements in Experiment 2.	106
Figure 50 Number of partitions in Experiment 2.....	107
Figure 51 Comparison of the estimated and referenced [136] tensile stress-strain relations.	108
Figure 52 Multi-linear model estimated by the proposed framework (Experiment 2).	109
Figure 53 Full-field measurement module in the developed experimental method.	131

List of Tables

Table 1 Parameters commonly used in the parametric studies of characterization method	44
Table 2 Parameters for test investigating transitional performance.....	45
Table 3 Parameters for tests investigating noise effect ($x \in [0, 40]$, $y \in [0, 40000]$).....	47
Table 4 Parameters for tests investigating prior means ($\Delta q^{0 0} \in [0, 2000]$).....	49
Table 5 Parameters for tests investigating prior variances ($\Delta P^{0 0} \in [0, 2000]$).	50
Table 6 Material properties of AS4/3506-1 specimen.....	52
Table 7 Parameters for the identification of elastic constants ($\forall i \in \{1, \dots, 4\}$)	52
Table 8 Elastic constants identified after 400 measurements.	54
Table 9 Parameters commonly used to create measurements in Tests 1-3.....	64
Table 10 Covariance of every j^{th} centroid observed by camera $c_l, \forall l \in \{1, 2, 3\}$, in Test 1.....	64
Table 11 Mean error percentage of the fused measurements (Test 1).	66
Table 12 Parameters for estimation using multiple cameras with different covariance, $\forall l \in \{1, \dots, 50\}$ (Test 2).	66
Table 13 Parameters for the data fusion technique, $\forall l \in \{1, \dots, 4\}$, and $n_c = 4$ (Test 3).....	68
Table 14 Material parameters of AS4D/9310 graphite/epoxy lamina.	70
Table 15 Parameters for the estimation of elastic constants using $n_c = 4$ cameras.	71
Table 16 Parameters for the estimation of elastic constants using $n_c = 4$ cameras.	74
Table 17 Use of parameters in defining a specific partition.	77
Table 18 Material parameters of the AS4D/9310 graphite/epoxy laminated specimen for numerical examples.	84
Table 19 Incremental partition value of each strain quantity for numerical examples.....	84
Table 20 Incremental partition values used for Example 1.	85
Table 21 Measurement covariance and prior knowledge used in Example 1 ($n_p=3$).	86
Table 22 Parameters for the reliability study of nonlinear characterization method.....	89

Table 23 Equipment models and their settings used in the developed experimental system.	94
Table 24 Material parameters of the specimens (Experiment 1).	96
Table 25 Geometry details of the specimens	96
Table 26 Prior and empirical knowledge for Test 1, 2 and 3.....	100
Table 27 Error of the estimated elastic parameters in each test (Experiment 1).	102
Table 28 Standard deviations of full-field strains with respect to different camera resolutions (Experimental data obtained from [141]).	103
Table 29 Parameters for the noise study ($\forall i \in \{1, 2, 6\}$)	103
Table 30 Projected accuracy of the proposed framework with respect to different camera resolution.....	105
Table 31 Incremental partition values used for Example 2.	106
Table 32 Prior knowledge of means used in Experiment 2, where $n_p=3$	107
Table 33 Final estimates after 190 measurements (Experiment 2).....	109

Nomenclature

Abbreviations

FEA	Finite element analysis
FEM	Finite element method
PDF	Probability density function
SVD	Singular value decomposition
CFRP	Carbon fiber re-inforced polymer
ANN	Artificial neural network
KF	Kalman filter

Notation

$(\cdot)^\top$	Transpose of (\cdot)
$\Delta(\cdot)$	Increment of (\cdot) in discrete time steps
$(\cdot)_\Delta$	Multiplication of $\Delta(\cdot)$ in discrete time steps
$(\tilde{\cdot})$	Measured value of (\cdot) with no modeled noise
(\cdot)	(\cdot) that is associated to multi-linear constitutive model
$\Delta(\cdot)$	Incremental strain value in a multi-linear constitutive model
$^e(\cdot)$	Quantity (\cdot) of an element e
$(\cdot)^+$	Pseudoinverse of (\cdot)
$(\cdot)_M$	(\cdot) in the material coordinate system
$^{I_l}(\cdot)$	(\cdot) that is derived from the I_l^{th} image that is corresponding to the c_l^{th} camera
$(\cdot)_j$	Quantity (\cdot) of the j^{th} centroid
$^d(\cdot)$	Data fusion results of (\cdot)

Specific Symbol Usage

E_1	Young's Moduli along the principal axis 1
E_2	Young's Moduli along the principal axis 2
G_{12}	Shear modulus
ν_{12}	Poisson's ratio
σ	Mechanical stress vector
ε	Mechanical strain vector
\mathbf{u}	Boundary displacement vector
\mathbf{f}	Boundary force vector
\mathbf{g}	Strain energy coefficient
\mathbf{h}	Transformation vector
\mathbf{H}	Transformation matrix
\mathbf{L}	Indicator for stress-strain relationship
α	Multi-linear partition indicator for ε_1
β	Multi-linear partition indicator for ε_2
γ	Multi-linear partition indicator for ε_6
n_A	Total number of multi-linear partition α
n_B	Total number of multi-linear partition β
n_G	Total number of multi-linear partition γ
k	Time step
n_m	Number of full-field measurement points
n_t	Number of centroids derived from the dots marked on specimen
n_b	Number of points on the loading boundary of specimen
W_Δ	Incremental external work
U_Δ	Incremental strain energy
ν_W	Uncertainties in external work measurements
ν_ε	Uncertainties in full-field strain measurements

L	Indicator for stress-strain relationship
θ	Fiber orientation angle
V	Geometric volume
A	Geometric area
t	Geometric thickness
k	Loading step
k	Kalman gain vector
P	Covariance matrix
\mathbf{x}_{c_l}	Location of the c_l^{th} camera in a global coordinate system
\mathbf{x}_c	States of all cameras in a global coordinate system
Q	Constitutive model
q	Constitutive parameters
U	Strain energy
W	External work

Chapter 1

Introduction

The concept of anisotropy has rapidly advanced the development of new materials technology with many emerging applications. As the material's directional dependence of a physical property is adjustable during the manufacturing stage, new materials that are much stronger than steel, while weighing substantially less, have recently increased their popularity in structural applications. This has sparked the advancement of the industrial age to the age of high-performance materials. Exploration and development of new anisotropic materials has provided extensive new materials technology by combining the strength and stiffness of steels with other properties, such as electro-conductivity and the ability to deform plastically. One example of these new materials is composite materials. The widespread use of composite materials in structures is a tribute to the forty plus years of research and development into these materials during which time the mathematics of the mechanics of materials have become well understood. This has led to research focused on material characterization. Characterization of material properties significantly contributes to the understanding of the future potentials of any new materials.

This dissertation presents an on-line framework for characterizing the nonlinear behavior of anisotropic materials. The on-line term is described here as a capability to analyze data moments after the data is collected. The characterization is performed on a macroscopic level. This framework includes a stochastic linear characterization method and stochastic nonlinear characterization method formulation through the development of a modified Kalman filter. This modified Kalman filter recursively updates the material parameters at each loading step and minimiz-

es the uncertainties in full-field measurements and measurements such as external work. In this Chapter, the background leading up to the recent interest in composites and the current state of knowledge are briefly reviewed, followed by the primary objective of this dissertation. The framework taken to achieve this objective is then presented, and the principal contributions arising from this work are summarized. Finally the contents of the remaining chapters in this dissertation are outlined.

1.1 Background

The founding and understanding of a new unknown material has led the human civilization as it evolved from the Stone Age to the Iron Age and then to the contemporary period, so-called the “Space Age”. Since 1957, the “Space Age” started with the development of high performance materials that are both strong and lightweight. Such high performance materials include composite materials, and have been added as the tool kit to replace customary metals in many applications, particularly in the aerospace industry. The advantages of composites can be seen in the composition of materials that is formed by individual material of distinct identities and properties. The overall material properties resulting from such composites provide improved specific or synergistic characteristics not obtainable by any of the original material components acting alone. Over the ages of time, it seems that the scientific revolution is strongly connected to certain special materials that enabled advancements in technology, and has come to be called progress.

The pursuit of human progress is not only the driving force behind scientists studying new materials today. It is simply driven by motivations, more akin to the curiosity of humans. For example, four-thousand years ago, a human accidentally stumbled across the performance of a new material by transferring carbon to iron using a state-of-the-art, at the time, charcoal-driven, high-temperature, controlled-atmosphere furnace. The human had produced some sort of very imperfect composition of a steel alloy. The appearance and the properties of such a composition were so remarkable, that many followers spent lifetimes advancing available technology to improve and characterize various materials to the point where the fully developed and vastly improved materials were used for many advanced applications in different industries.

Essential to the richness of the field is an understanding of the laws of physics and chemistry that enable detection and realization of new properties of matter. Despite having its roots in basic science, condensed-matter physics is viewed as a form of applied science. This is due in part because the well understood fundamental physical laws are applied to describe the individual atoms in solids. However, the collective properties of many atoms assembled together are too complex to be predicted from the first principles. The complex behavior is characterized by experimental approaches and understanding such behavior allows application of composite materials in many engineering fields.

Reductions in manufacturing costs, improvements in product quality and increased use of computer-aided design are all key issues affecting the future of composite materials in civil, aerospace and automotive applications. A common denominator in all of these issues is the need for characterizing reliable mechanical property data. Current characterization procedures based on static loading of test specimens tend to be slow and expensive. In addition, these materials encounter degradation of material properties in changing operating environments. Composite materials play a big part in many engineering applications, and as such, on-line monitoring of critical structural components has become the key to lengthening the operational life of these materials without interrupting the operation. The goal is to improve structural safety and prevent accidents by taking prompt action once the monitored values exceed any safety threshold. With the on-line monitoring capability, there has been increasing interest in understanding the characteristics of the structure under complex loading conditions.

From the manufacturing standpoint, material property characterization adds to the significant cost of manufacturing. The complexity of test procedures and test equipment often force small and medium-sized composite fabrication shops to rely on outside testing laboratories to perform the characterization. Such a separation of the manufacturing and testing functions precludes an on-line evaluation of the properties, which is needed for optimization and control of the manufacturing process. A material characterization system that is fast, inexpensive and capable of providing feedback instantly to the manufacturing process would allow material properties to be controlled within designed limits.

In consideration of the need for on-line characterization of complex materials to assess any deterioration in product quality and serviceability, it is proposed that a fast and efficient characterization framework that stochastically characterizes the properties of anisotropic materials on-line could be very useful to meet the challenges posed by the aforementioned processes.

1.2 Objective

The objective of this dissertation is to develop a new framework capable of characterizing the nonlinear behavior of anisotropic materials on-line, while reducing the uncertainties that exist in the framework.

1.3 Approach

In order to achieve this objective, it is necessary to first develop a stochastic linear characterization method to characterize the elastic properties of anisotropic materials. The developed method stochastically identifies the elastic constants of anisotropic materials by modeling the measurement noise and removing the effect of noise from the results. Based on the principle of energy conservation, an energy-based characterization methodology, capable of characterizing the behavior of anisotropic materials is formulated by equating the applied external work to the strain energy of the body. The developed method extracts stochastic equations from the formulas of the energy-based characterization methodology and recursively estimates the elastic constants at every acquisition of measurement using a Kalman filter (KF). Since the modeled measurements are expressed nonlinearly, the KF utilizes a Kalman gain that is newly derived in this dissertation through variance minimization to achieve optimal characterization.

The developed stochastic linear characterization method becomes a basis to a multi-linear characterization method that estimates nonlinear constitutive relations of anisotropic materials. The multi-linear characterization method represents constitutive relations by multi-linear partitions, based on the assumptions that the materials are rate-, path- and temperature- independent. Since the characterization is connected by multiple linear characterization processes, the coefficients of each part are then determined by the previously derived KF. The stochastic multi-linear

characterization method scales up the number of estimates and identifies the coefficients of each linear partition when strain values are observed within each partition.

The KF in both stochastic linear and multi-linear characterization methods represents the estimates of material properties by means and covariance, and start with prior estimates every time the sensor takes a measurement. The updates in measurements remove uncertainty through sensor observation. Since the estimates are recursively updated during sensor observations, the KF considers not only the current measurements, but also the prior knowledge and the past estimates. This recursive update mechanism enables the on-line capability of the proposed framework in characterizing the nonlinear behavior of anisotropic materials. In addition to the estimates, the use of differential entropy at every update enables the stochastic multi-linear characterization method to evaluate the certainty associated with all the estimates performed on-line.

The measurement certainties are further improved by a multi-camera data fusion technique. During experimental testing, the material specimen is marked with a uniform set of dots to measure the deformity of the material as load is applied. In the multi-camera system, each camera observes the centroid of each dot and model a Gaussian probability density function (PDF) on each centroid. The technique fuses all the centroids and computes the mean and covariance associated to each fused centroid by the product of all Gaussian PDFs derived from all camera images. The probabilistic model of each fused centroid is modeled as a total Gaussian PDF, which is represented by a fused mean and covariance. The full-field displacements and strains are computed by substituting the fused means into shape functions. The covariance of these full-field measurements are then derived by propagating the fused covariance through the associated mathematical functions. Both means and covariance constructs the Gaussian PDFs of the measurements. These probabilistic models provide the information of measurement covariance to the stochastic linear and multi-linear characterization method, and subsequently derive the optimized Kalman gains.

1.4 Principal Contributions

The principal technical contributions of this dissertation are enumerated as follows:

- A unique stochastic method that determines a multi-linear model for approximating non-linear constitutive relations of anisotropic materials is presented.
- A novel stochastic method that determines the means and covariance of elastic constants of anisotropic materials is developed.
- A recursive measurement update mechanism that enables nonlinear characterization of anisotropic materials performed on-line at every acquisition of measurements is demonstrated.
- A new Kalman gain, which achieves optimal estimation and incorporates prior knowledge and noise information of full-field measurements, is derived through variance minimization.
- An on-line quantification measure, which is formulated based on the covariance of characterization results, is defined.
- A novel multi-camera data fusion technique that improves the certainty of measurements based on the product of Gaussian distributions is demonstrated.
- A new technique, which models the covariance of measurements through the propagation of uncertainties, is presented.

1.5 Publications

To date, components of the dissertation have been presented in the following publications:

Patents:

- [1] Tomonari Furukawa, Jinquan Cheng, **Jan Wei Pan**, John G. Michopoulos and Athanasios Iliopoulos, “An integrated method and system for full-field strain measurement and material constitutive characterization on uniaxial testing machine”, *provisional patent*, 2010
- [2] Tomonari Furukawa, **Jan Wei Pan** and Hou Man, “Material characterization based on the principle of minimum total potential energy”, *provisional patent*, 2009

Journal Articles:

- [1] Tomonari Furukawa and **Jan Wei Pan**, “Stochastic identification of elastic constants for anisotropic materials”, *International Journal for Numerical Methods in Engineering*, 2010, **81**:42-452
- [2] **Jan Wei Pan**, Jinquan Cheng, Tomonari Furukawa and John G. Michopoulos, “Data fusion of probabilistic full-field measurements for material characterization”, *Key Engineering Materials Journal*, 2010, accepted
- [3] Jung-Hoon Sul, B. Gangadhara Prusty and **Jan Wei Pan**, “A fatigue life prediction model for CSM GRP”, *Fatigue & Fracture Engineering Materials & Structures*, 2010, doi: 10.1111/j.1460-2695.2010.01460.x
- [4] **Jan Wei Pan**, Tomonari Furukawa, Hou Man, Athanasios Iliopoulos, John G. Michopoulos and John Hermanson, “An energy-based computational and experimental method for the elastic characterization of materials”, under review
- [5] **Jan Wei Pan**, Jinquan Cheng and Tomonari Furukawa, “Multi-camera data fusion for stochastic energy-based characterization”, *International Journal of Computational Methods*, accepted
- [6] Tomonari Furukawa, John Michopoulos and **Jan Wei Pan**, “Recursive estimation technique for energy-based characterization”, *International Journal for Numerical Methods in Engineering*, submitted
- [7] Hou Man, Tomonari Furukawa, **Jan Wei Pan**, Athanasios Iliopoulos, John Michopoulos, Adrian Orifici and John Hermanson, “Experimentally validated neural network constitutive modeling using energy-based characterization”, under review
- [8] B. Gangadhara Prusty, **Jan Wei Pan** and Jung-Hoon Sul, “Characterization of temperature-dependent behavior of chopped strand mat GRP during low cyclic fatigue, *World Journal of Engineering*, 2009, **6**(Supp): 825-826
- [9] **Jan Wei Pan**, Tomonari Furukawa, Jinquan Cheng and John G. Michopoulos, “Stochastic nonlinear material modeling using energy-based characterization”, in preparation
- [10] **Jan Wei Pan**, Jinquan Cheng and Tomonari Furukawa, “Real-time energy-based characterization of solid materials”, in preparation

Conference Papers:

- [1] Tomonari Furukawa, John G. Michopoulos and **Jan Wei Pan**, “The Deterministic and Stochastic Energy-based Characterization of Composites – A Generalized Theoretical Framework”, *17th International Conference on Composite Materials*, Edinburgh, UK, July 27-31, 2009, 10pp

- [2] **Jan Wei Pan**, Tomonari Furukawa and Hou Man, "Kalman filter technique for the energy-based elastic identification of composite materials", *3rd Asian Pacific Congress on Computational Mechanics (APCOM'07) in conjunction with 11th International Conference on Enhancement and Promotion of Computational Methods in Engineering and Science (EPMESC XI)*, Kyoto, Japan, 2007, 10pp
- [3] **Jan Wei Pan** and Tomonari Furukawa, "Comparison between Kalman filter and singular value decomposition for energy-based anisotropic elasticity characterization", *The 5th International Conference on Numerical Analysis in Engineering*, Padang, Indonesia, 2007, 10pp

Conference Abstracts and Presentations:

- [1] **Jan Wei Pan**, Jinquan Cheng and Tomonari Furukawa, "Energy-based characterization based on multi-sensor data fusion", *8th International Conference on Fracture and Strength of Solids*, Kuala Lumpur, Malaysia, June 7-9, 2010
- [2] **Jan Wei Pan**, Tomonari Furukawa and Hou Man, "Validation of the stochastic elastic energy-based characterization", *10th US National Congress on Computational Mechanics (USNCCM X)*, Columbus, Ohio, July 16-19, 2009
- [3] **Jan Wei Pan** and Tomonari Furukawa, "Nonlinear Stochastic Modeling of Composites using the Energy-based Characterization", *The 2009 Joint ASCE-ASME-SES Conference on Mechanics and Materials*, Blacksburg, Virginia, June 24-27, 2009
- [4] **Jan Wei Pan** and Tomonari Furukawa, "Stochastic Elastic Identification of Anisotropic Materials", *Signals and Systems Seminar*, Blacksburg, Virginia, USA, March 20, 2009
- [5] **Jan Wei Pan** and Tomonari Furukawa, "Identification of Anisotropic Properties from Erroneous Full-field Measurements", *4th International Conference on Composites Testing and Model Identification*, Dayton, Ohio, USA, October 20-22, 2008
- [6] **Jan Wei Pan**, Tomonari Furukawa and Israel Herszberg, "Stochastic Identification of Composite Materials", *Composite CRC Conference & Exhibition*, Melbourne, Australia, March 13-14, 2008
- [7] **Jan Wei Pan**, Tomonari Furukawa, Hou Man and Israel Herszberg, "Unscented Kalman filtering for elastic identification of composite materials using the energy-based method", *14th International Conference on Composite Structures (ICCS/14)*, Victoria, Australia, 2007
- [8] Hou Man, Tomonari Furukawa, **Jan Wei Pan** and Israel Herszberg, "Constitutive Characterization of Composite Materials using the Data Driven Approach", *14th International Conference on Composite Structures*, Victoria, Australia, November 19-21, 2007
- [9] **Jan Wei Pan**, Tomonari Furukawa and David Kellermann, "Application of Kalman Filtering to the Energy-based Material Constitutive Modelling", *Ninth U.S. National Con-*

gress on Computational Mechanics (USNCCM IX), San Francisco, July 22-26, 2007, 2pp

- [10] David Kellermann, Tomonari Furukawa and **Jan Wei Pan**, "A Continuum Mechanics Solution for In-plane Shear Locking in Plate and Shell Elements", *Ninth U.S. National Congress on Computational Mechanics* (USNCCM IX), San Francisco, July 22-26, 2007, 2pp
- [11] **Jan Wei Pan** and Tomonari Furukawa, "Application of Kalman Filtering to the Continuum Materials Characterization", *presented at Department of Mechanical and Materials Engineering*, Universiti Kebangsaan Malaysia, July 20, 2007

1.6 Organization

This dissertation is organized as follows:

- Chapter 2 reviews previous work based on on-line nonlinear characterization of anisotropic materials using vibration analysis, standard mechanical loading tests, field measurements and implicit constitutive modeling. These research efforts further support the claims provided in this introductory chapter, and thus signify the objective of this dissertation.
- Chapter 3 describes an overview of energy-based characterization formulations and derivation of full-field measurements related to this characterization. Following this, a contemporary deterministic approach, which determines elastic constants from the energy-based characterization formulations, is also presented.
- Chapter 4 presents a novel stochastic linear characterization method that identifies elastic constants of anisotropic materials by modeling measurement noise and removing its effect using a Kalman filter. First, stochastic equations are derived from the energy-based characterization formulations, and followed by the derivation of recursive mechanisms that allows the method performed on-line. The derivation of a new optimal Kalman gain is then discussed. This Chapter also presents numerical studies of this method and further compares itself to the deterministic approach.
- Chapter 5 describes a multi-camera data fusion technique that improves the certainty of measurements in the proposed framework. First, Gaussian probabilistic representation of

dots marked on a specimen is described, and followed by the derivation of fused information through product of all Gaussian distributions. Probabilistic measurement models are then derived through propagation of uncertainties method. The robustness of this technique is then highlighted by applying noisy measurements from different cameras to characterizing anisotropic materials.

- Chapter 6 presents a stochastic multi-linear characterization method that approximates nonlinear constitutive relations of anisotropic materials. The definition of multi-linear constitutive model is first presented. This is followed by the derivation of stochastic equations and Kalman filter based on the constitutive models. A quantification measure that describes certainty of on-line results is presented afterwards. Following this, a series of numerical studies of this method is presented.
- Chapter 7 describes the experimental studies of the stochastic linear and multi-linear characterization methods presented in Chapters 4 and 6, and these results are compared with known experimental values. The studies include parametric studies of the proposed framework and also its robustness to existing camera technology. Both features and limitations of the proposed framework are also discussed.
- Chapter 8 summarizes the contributions of the research presented by this dissertation and discusses areas for potential future work.

Chapter 2

Literature Review

This Chapter reviews the past contributions concerned with characterizing the nonlinear behavior of anisotropic materials on-line. The research methods in the field of vibration test procedures focused on characterizing anisotropic materials are discussed in Section 2.1. Despite the on-line capability of vibration mechanics, the metrics are not well suited for handling nonlinear behavior. Section 2.2 covers mechanical loading tests that are used for characterizing the nonlinear behavior of materials. While these tests require multiple specific specimens and configurations, characterization methods that use full-field measurements provide more flexibility in experimental configuration. These methods are presented in Section 2.3. Despite the advantage of having more measurements, most of these methods are off-line and require batch processing of measurements collected from the past. Section 2.4 covers an implicit modeling methodology, which is modeled with non-parametric test methods, and further demonstrates the capability of this method in determining the nonlinear behavior of materials on-line. This chapter is concluded with a summary of the state-of-the-art and how this dissertation stands to leverage the state-of-the-art to make advances in the field of on-line material characterization.

2.1 On-line Evaluation based on Vibration Testing

On-line evaluation of anisotropic materials has been well established in the field of vibration mechanics. Composites, as one of the prime examples of anisotropic materials, have recently attracted more attentions due to their high customizability in stiffness, strength, density and con-

ductivity [1]. One of the vibration test methods performed in composite analysis is modal vibration testing. This testing is based on the measurement of modal frequencies, modal damping factors and mode shapes of a specimen or structure [3-5]. The test procedures provide foundations for rapid, inexpensive characterization of both elastic and viscoelastic properties for design and manufacturing [6]. This has contributed to the inspection of damaged and repaired composite structures, where rapid and inexpensive test methods are required.

Most common vibration analyses have shown that modal testing in either single-mode or multiple-modes of vibration can be used to characterize the effective modulus and damping values of composites and their constituents under various environmental conditions [7]. In the single mode testing, a single measured modal frequency is substituted into an equation derived from the equation of motion for the specimen and its boundary conditions. The natural frequency measurements from specimens vibrating in a single mode have been used for many years, but the test procedures are typically slow and cumbersome, and are only suitable for small laboratory specimens [8]. In the multiple-mode testing, several natural frequencies are measured to develop simultaneous solutions of frequency equations that identify the independent elastic property of composite plates and shells. By comparison, multiple-mode testing eliminates the need for different static tests, and is widely documented in several standards [9, 10, 11-14].

One of the most popular non-destructive testing techniques documented in these standards is the impulsive excitation technique. Modal testing by the use of impulsive excitation methods has been shown to have the potential to be a fast and reliable approach for characterizing intrinsic material properties of composites [15]. This is further supported by recent developments in laboratory facilities, such as microprocessor-based Fast Fourier transform (FFT) analyzers, and PC-based virtual instruments, which has made it more attractive to use impulsive excitation in conjunction with either frequency-domain analysis or time-domain analysis to extract modal parameters from the response measurements in real-time [16].

Research has been performed on applying modal testing methods to the on-line evaluation of operational full-scale composite structures. For example, Yang *et al.* [17] presented an impulse/frequency response test to evaluate engine intake and exhaust valves of different materials. In their work, frequency data were monitored. However, the conversion from the frequency data

to material properties was not studied in their scope of work. The major difficulty in testing full-scale parts appears to be in the development of an analytical model for the solution of inverse problems, in the case where in-situ properties are desired. Alternatively, Cheng and Hwu [18] presented a neural network (NN) model to characterize the material properties of composite wings from frequency data. They performed an on-line characterization of composite wings by measuring the impulse applied on a wing specimen that is clamped on one end and free on the other end. By taking the average of natural frequencies of the first three modes, an artificial neural network is then provided to output the elastic properties in an on-line sense.

Vibration tests allow the specimens to be geometrically free from standardized designs and reduce the required limitations on their boundary conditions. Although a considerable amount of literature exists for the classical solutions to inverse problems dealing with simple structures like beams [19], it is certain that approximate numerical approaches such as finite element (FE) methods will have to be used for parts having complex shapes. A suitable optimization routine is often needed to tune up the set of material properties that minimizes the difference between the measured and predicted frequencies, subject to the provided geometric and boundary constraints on the test specimen [20]. In practice, certain experimental configurations, such as the ideal simply-supported boundary condition along all four edges, have proven to be efficient for modal testing, but are also very difficult to execute [21].

Even though some experimental configurations of mode testing, such as the *free-free* boundary condition [22 and 23], are possible, the characterization results are considered to be unreliable since the simple closed form frequency equations are not straightforward and are solved approximately [24]. Ip *et al.* [25] proposed an information updating technique to determine the elastic constants of orthotropic cylindrical composite shells based on the natural frequencies obtained from free-free configuration modal testing. The technique utilized a Bayesian type estimator to tune the material parameters of an analytic function repeatedly until the measured and analytical frequencies are comparable to each other. A quantitative measure of the confidence in the adjusted material parameters is then obtained and thus leads to its wide application in various configurations, such as beams and columns [26], membranes [27], 3D solid elements [28], plates [29] and shells [30]. Similarly, Kuttenkeuler [31] coupled the same modal analysis technique

with the use of a finite element based method to determine the plate stiffness of orthotropic composite laminates, and was able to characterize more complex plate shapes. Despite the robustness of modal analysis techniques, they have been shown to produce erroneous models although the discrepancy between test and analysis modal responses can be bridged [144 and 147].

The above past works have shown the significant advancement in performing on-line evaluation of anisotropic materials characterization through vibration testing. Vibration analyses that use modal parameters have proven to be effective in characterizing the elastic properties of anisotropic materials on-line [149]. Despite its promising on-line capability, metrics based on modal parameters are not well suited to the resolution of inverse, nonlinear problems [145, 146 and 148].

2.2 Nonlinear Characterization based on Mechanical Testing

The state-of-the-art in the area of mechanical testing for nonlinear characterization of composites is subsequently reviewed in this Section. Advanced composites, such as fiber re-inforced composites (FRC) exhibit different types of nonlinear characteristics in their constitutive behavior [32, 33]. In these studies, the nonlinear constitutive relations were derived from mechanical tests based on various, well-established physical laws [150].

Schapery [34] developed a general viscoelastic and viscoplastic constitutive model based on thermodynamics principles. The model takes the form of convolution integrals of linear viscoelasticity. The nonlinearities of this model appear in the measures of stress and strain and in the reduced time. Although good correlations were found with experimental results in the presented examples, the stress and strain were linearly dependent inside the formulations based on an assumption that the strains were small enough for linear theory to be applicable. Papanicolaou *et al.* [35] subsequently proposed a method to predict the nonlinear viscoelastic behavior of unidirectional fiber-epoxy composites with the analysis of ultimate tensile strength. Creep-recovery tests on 90° unidirectional carbon-fibre/epoxy-matrix composites were performed and resulted with good agreements between the prediction and experimental results. Jiang *et al.* [36] showed an equivalent method that promisingly modeled the rate-dependent nonlinear behavior of selected carbon-fibre/epoxy-matrix composites. Melo and Radford [37] developed a nonlinear viscoelas-

tic model for transverse isotropic composite lamina, based on a linear theory with a smaller number of required model coefficients. The three-dimensional viscoelastic behavior was claimed to be practically characterized with the described experimental procedures. Their work was validated through an experimental investigation using a Dynamic Mechanical Analyzer. The research conducted by these scientists leads the way in modeling nonlinear viscoelastic and viscoplastic materials by utilizing mechanical tests. The work in this dissertation will seek to understand the physics behind the material behavior by leveraging the mechanical tests developed by these scientists.

Tawab and Weitsman [38] presented a strain-based thermodynamics framework for modeling the continuum damage behavior of viscoelastic materials. The effect of damage is introduced through direct coupling between the damage variable and the viscoelastic internal state variables [39]. Lonetti *et al.* [40] showed a comparable approach to express damage in each individual lamina of fiber-reinforced composites by coupling continuous damage mechanics with classical plasticity theory in a consistent thermodynamic framework using internal state variables. The in-plane and interlaminar damage of composite laminates was subsequently investigated under torsional loading. Kumar and Talreja [41] formulated a constitutive model for linear viscoelastic composites in the continuum damage mechanics framework. Their model was derived from a pseudo energy function with internal variables. This differs from the previous works in that it used a pseudo energy function based on the Laplace transform of the original linear constitutive equations and the developed model was able to predict the viscoelastic behavior of cross-ply laminates that contains transverse matrix cracks. The works of these researchers have demonstrated that the assessment of damage behavior is primarily built upon the nonlinear characterization of materials.

Most composite laminates contain significant nonlinear lamina stress-strain behavior occurring in the transverse direction as shear deformation. Uniaxial compression tests are typically performed with longitudinal and transverse strains measured by strain sensors mounted at the center of specimen. In an early work of Petit and Waddoups [42], a piecewise linear method for determining the ultimate strength of laminated composites, and nonlinear lamina stress-strain behavior was presented. To completely characterize the nonlinear behavior, a uniaxial test in two

principal directions and a shear test were required to characterize elastic properties from uniaxial tension and compression curves, both parallel and transverse to the filament, and a shear curve. When determining the fiber/matrix interfacial bond strength of composites, Blaiszik *et al.* [43] showed that each curve is often specified to one unique specimen instead of the material type in general. They demonstrated that at least five specimens were necessary in each test to determine representative mechanical behavior for a material with good agreement between experiments. The existence of multiple standards, documenting the test programs, evaluation strategies and design procedures, has further allowed experimentalists to perform a wide range of testing for studying the material behavior of composites.

The behavior of various composite types in tensile tests is characterized by the following standards. The ASTM D3039 [9] standard is used for balanced symmetric composites; the BS2782 [44] standard is used for prepgs specimens; the CRAG 300 & 302 [45] standard is used for unidirectional fiber-reinforced plastics and woven fiber-reinforced materials; and the ISO 527 [11] stanadard is used for fiber reinforced polymers. The shear material behavior of composite materials is characterized by various standards, which use different specimen configurations, as designated in ASTM D3518 [12] for $\pm 45^\circ$ shear test; ASTM D4255 [10] for rail shear test; ASTM D5379 [13] for V-notched beam or Iosipescu test; and ASTM D3044 [14] for plate-twist test. Although it is advantageous to have these standards for enabling repeatability of experiments, they reflect a range of opinions on how a specimen and an experiment should be tailored for a specific type of composites. This dissertation seeks to challenge some of these standards by developing a new test method that is not constrained by the specimen geometry.

Additionally, improper mounting and usage of contact sensors such as extensometer and surface-bonded resistive strain gages, easily create measurement uncertainties. To maximize the sensing information at contact points, Tairova and Tsvetkov [46] suggested that sensor bases must be one order of magnitude larger than the characteristic size of the specimen surface roughness. While determining the damage behavior of composites, such sensors are easily damaged by the vibration shock, thus creating inconsistent measurements in subsequent experiments. In addition, these sensors contain high transverse sensitivity and the measurements can be affected by any undesired motion that is not along the loading axis by reflecting this motion incorrectly in

the sensor measurement [47 and 48]. The transverse sensitivity errors are further masked by the correction of gage factors, thus creating bias in strain measurements [49].

Hahn and Tsai [50] discovered in their experiment that the stress-strain response of unidirectional lamina under off-axis loading is nonlinear in shear stress-strain relation. A higher order constant was introduced in their complementary elastic energy density function for predicting such nonlinear behavior of lamina, and later on, their work was extended to describe the nonlinear behavior of laminated composites [51]. Nuismer and Whitney [52] adopted this method, and in their work, experimental studies were performed to determine failure criteria for predicting the uniaxial tensile strength of a laminated composite that contains discontinuities through-the-thickness of the material. A similar approach was developed to create a failure criterion that reflects the damage resistance by low-velocity point impact [53] and tensile (or compression)/shear failure [54] respectively. Similarly, laminated composite damage was modeled by Ladeveze and Le Dantec [55] at the elementary-ply, where damage mechanics was used to describe the matrix microcracking and fibre/matrix debonding. In their experimental study, the rupture properties were described by a cross-ply laminate loaded in uniaxial tension. Sun and Chen [56, 57] developed a micromechanical model of elastic-plastic behavior of fibrous composites. The micromechanical model is used to calculate the stress-strain relations for off-axis boron/aluminum composites. The relations are subsequently used to model a macromechanical orthotropic plasticity response [58].

Most experimental characterization approaches determine the mechanical behavior by assuming uniform deformation on specimens and this assumption is, nevertheless, not easily held. One of the main reasons for the failure of this assumption is due to the improper boundary conditions of the test specimen that create undesired kinematic fields along the specimen [59, 60]. Another source of error is the misalignment of specimens to the loading axis of the machine, which also create inevitable non-uniform deformation fields [61 and 62]. Some manufacturing issues such as fiber misalignment [63, 64] and geometrical defects [65] were also found to create non-uniform deformation fields at the stress concentration areas of the specimen. These issues are further summarized in a study performed by Lomov *et al.* [66].

The past works reported above evidently contributed to the foundation of nonlinear constitutive modeling by providing insights into the physics of different material behavior. The nonlinear behavior discussed here was derived from the thermodynamic framework and other related energy principles. Most of these mechanical test methods are concerned with a point-measurement approach using contact sensors to obtain the strain information at a “hot spot”. Without any further analysis, this measurement technique is unable to provide information about the entire structure. Multiple experiments with large number of specimens are thus necessitated to improve the reliability of these test methods. Consequently, this dissertation seeks to find robust characterization approaches, which describe the nonlinear behavior of anisotropic materials on a continuum basis, while being robust to any specimen shape and test configurations.

2.3 Characterization based on Full-field Measurements

Recent advances have seen the development of full-field measurement techniques [67-77] to include the spatial information over the specimen area in material characterization problems [78-80]. This has contributed to a number of investigations in developing techniques capable of characterizing material behavior using the local effects experienced globally throughout the continuum.

With the use of non-contact full-field measurement tools, such as digital image correlation [73], grid method [81] and Moiré interferometry [82], Grediac *et al.* [24, 83] proposed a so-called virtual fields method (VFM) that determines the properties of anisotropic materials through a set of governing equations that are based on the virtual work principle. Grediac *et al.* performed extensive studies on choosing the virtual fields of the governing equations that fulfill the admissibility conditions of specimens. Such virtual fields are often iteratively derived by assuming the static and kinematic boundary conditions of specimens. The introduction of the closed-form solutions, in the form of VFM, has further inspired numerous research works in identifying parameters of visco-plastic [84], elasto-plastic [85] and damage models [86] for anisotropic materials.

For example, Giraudeau *et al.* [87] presented an experimental method that uses VFM to identify not only the elastic properties, but also the damping material properties of isotropic vibrating

plates excited at resonance and out of resonance frequencies. Promma *et al.* [88] applied VFM to identify the constitutive parameters of a hyperelastic model based on the full-field measurements obtained from digital image correlation that is suitable for large strain deformation. Another application of VFM is the characterization of the damage behavior of composites, performed by Chalal *et al.* [89]. Chalal *et al.* applied VFM to determine the in-plane shear response incurred by damage and then derive the nonlinear constitutive model for the composite. Although this method has seen its advances over the past decade, a sensitivity study, performed by Avril and Pierron [90], discovered that the accuracy of VFM is highly dependent on the derivation of virtual fields. In the experiments, tailored experimental configurations are thus required to satisfy the boundary conditions assumptions of the chosen virtual fields.

Most of these field characterization methods are built upon the implicit formulations that link the measured quantities and the material constitutive parameters [91, 92, 93]. The input residuals between the numerical and experimental models are often minimized through various optimization procedures, such as the sensitivity-based element-by-element updating procedure [94], so that the computed and measured full-field deformations are matched with each other. For instance, Pagnacco *et al.* [95] demonstrated an inverse strategy that substitutes the known quantities to yield a set of basis equations for recovering the unknown constitutive parameters. This input residual method is applied based on the experimental availability of all the nodal displacements and the prescribed forces.

On the contrary, the output residuals are minimized through procedures such as the modal assurance criterion [96] and the reciprocity gap method [97]. Unlike the input residual method, the output residual method is more robust and can be applied even when the displacement fields are partially known. Pagnacco and Lemosse [98] demonstrated that unconstrained minimizations can still be achieved even when the prescribed forces are completely unknown. It was observed that the identified parameters are less sensitive to imperfectly-known displacements on the boundary by means of an iterative procedure. Similarly, Bruno *et al.* [99, 100] presented an inverse procedure that substitutes prescribed forces and experimental measured nodal displacements into iterative finite element simulations for recovering the unknown elastic properties from certain initial values set by the user. A mixed numerical-experimental characterization technique was presented

by Lecompte *et al.* [24, 101] to update the orthotropic elastic constants in a biaxial test by minimizing the residual between the measured strain fields and the computed strain fields of cruciform composite specimens. Since the accuracy of these updating method types is highly dependent on the optimization routine, Ienny *et al.* [102] performed a review on the existing cost functions that are effective in the common optimization routine. Several cost functions have thus been presented to improve the accuracy of the characterization results [103-106].

Another characterization method based on full-field strain is an energy-based method that characterizes materials by evaluating them on a continuum basis [107, 108, 109]. In this method, there is no need to choose the virtual fields to fit the specimens' boundary conditions and hence allow for more robust boundary condition definitions and specimen designs. The concept of the energy-based method was originally inspired by a series of studies performed by Mast *et al.* [110, 111, 112]. In their studies, they proposed the quantification of damage in composite structures on a continuum basis. An in-plane loader system was utilized to generate a significant amount of experimental data, including the applied displacements and the resultant forces were used to compute the dissipated energy of a structure to quantify its damage. Since full-field strain measurements are not available to define the system, the experimental data is combined with a linear FE model to tune-up material parameters through minimization of residuals between the measured external work and the numerically derived strain energy. The use of a multi-axial testing machine in their studies exhibited the robust characterization of laminated composite plates without requiring multiple specimens. This method expanded the potential usage of multi-axial experiments where the deformation of specimens of various shapes and geometries can be observed under a variety of loads.

Furukawa and Michopoulos [107-109] subsequently proposed a characterization method that designs the loading path of a multi-axial testing machine. This machine measures more information than any other measurement device of strain states for determining constitutive parameters of laminated composite plates. In the energy-based framework, a deterministic technique was implemented to characterize the elastic behavior of the material by equating the strain energy, derived from the full-field strain measurements, with the external work, derived from the boundary displacement and force. The deterministic technique first constructs a set of linear

equations with a non-square matrix at every acquisition of measurement and then successively identifies the elastic parameters by solving for the pseudoinverse of the matrix. The characterization method, based on the conservation of energy principle, additionally applies singular value decomposition (SVD) to derive the distinguishability and uniqueness for the quantification of the loading path. In conjunction with the identified results, the characterization method quantifies various experiments and load paths towards producing the most informative deformation properties of the material characterization with a single specimen in a single test.

Despite the robustness introduced in these closed-form solutions, several studies [113-115] have found that the use of full-field measurements is highly sensitive to the measurement uncertainties. A sensitivity study of Avril *et al.* [116] found that the reliability of VFM is highly sensitive to the measurement noise and choice of virtual fields. Patterson and his group [117 and 118] addressed the importance of characterizing instrumental error introduced by the optical camera systems, indicating that a careful selection of camera image resolution can minimize uncertainties. Other sources of error include the inadequate choice of speckle size, gray level interpolation and subset size, which can also affect the quality of full-field measurements [119].

Although the energy-based formulations allow a deterministic approach to utilize a general framework to characterize materials from any test, the results are often unreliable since the closed form solution is easily ill-conditioned due to the experimental configuration. On the other hand, VFM and model updating methods must to be tailored for any material test that has different boundary conditions. Despite the advantage of using full-field measurements, most of these methods are off-line and require batch processing of data collected in the past.

2.4 Implicit Modeling of Nonlinear Behavior

Implicit modeling methodology has been applied for modeling constitutive relations based on non-parametric modeling techniques. Such methodology has recently shown its capability to characterize nonlinear behavior on-line. Extensive studies of this methodology have been performed in the areas of metallic materials and soil constitutive model [120], the rate dependent material model [121], and the thermal constitutive model [122]. In this methodology, artificial

neural networks (ANN) are well known for the ability to model nonlinear and complex relations between structure parameters and dynamic characteristics [123].

Liu *et al.* [124] presented a modified hybrid numerical method and a neural network that is capable of characterizing the material properties of functionally graded material plates on-line, once an ANN model is trained. The ANN model is, however, trained off-line using a set of training data that contain various assumed material properties and their corresponding displacement responses calculated from the hybrid modified numerical method. Off-line retraining process is required if the calculated displacement responses deviate unacceptably from the actual ones. Bhat *et al.* also presented another application of ANN to perform on-line characterization of failure modes in carbon fiber re-inforced polymer (CFRP) composites [125]. A set of composite specimens with different shapes and configurations was subjected to fatigue spectrum loading in stages, and the other set was subjected to static compression loading. The ANN model developed was made suitable for on-line monitoring of acoustic emissions, which is usable for identification of failure modes. Several efforts have been made to reliably model the complex behavior of anisotropic materials by using extensive training data from experiments.

Al-Haik *et al.* [126] investigated the viscoplastic behavior of composites by comparing an ANN model to an explicit viscoelastic model at different stress-temperature conditions. The explicit model utilizes the tensile and stress relaxation experiments to predict the creep strain, whereas the ANN model captured the composite viscoplastic behavior by applying training data from the experimental results obtained via creep tests performed at various stress-temperature conditions. In their work, multiple samples are tested under different environmental conditions. Ten samples, which were annealed for 4 hours, were tested at 5°C increments over the temperature range of 45 to 75°C. In the load relaxation test, standard tensile specimens were loaded at a constant displacement rate of 2mm/min until constant strain was maintained in the specimen. The ANN model was trained by the normalized temperature, stress level and time values and was able to predict more accurate results than the explicit viscoelastic model at different stress-temperature conditions.

Hashash *et al.* [127] demonstrated the development of a neural network (NN) constitutive model to map the nonlinear stress-strain relations of composites. An autoprogressive training

technique was used to extract the material constitutive relationship from structural systems by using the stress-strain response of a FE model as the training data. Alternatively, Ghaboussi *et al.* [128] demonstrated that an in-plane neural network constitutive model that is trained by comparing measurements of some monitoring points with the FEA results of a structural test. Similarly, Pidaparti and Palakal [129] also derived a NN constitutive model by applying both uniaxial and off-axis tests on angle-ply laminates to obtain training data. Al-Haik *et al.* [130] showed the use of NN to replace parametric viscoplastic models of polymer matrix composite. Haj-Ali and Kim [131] showed a multi-axial NN constitutive model for FRP composites. In their work, both off-axis tension/compression and pure shear tests on the FRP were conducted to train the ANN model. Although the developed model is able to represent the in-plane constitutive relation, inconsistency can potentially be induced since the training data were collected with various specimen configurations and experiments. A thorough study on the past work of nonlinear modeling approaches, such as genetic algorithms to improve the efficiency of ANN training procedure can be found in [132].

The aforementioned works have shown the significant success in applying implicit modeling methodology to characterize the nonlinear behavior of anisotropic materials. The described methodologies have shown the on-line capability, after the NN model has been trained. The training procedure of NN models requires a considerable amount of training data and results may be biased if a different boundary condition is used as the input to NN model. Although there were some cases when training data was supplied from numerical models [133], exact conditions have to be met if the trained model is to be used to characterize a nonlinear behavior on-line.

2.5 Summary

This Chapter has reviewed the state-of-the-art in material characterization, particularly those works concerned with characterizing nonlinear behavior of anisotropic materials. Research developments on these problems have seen great evolution in the nonlinear characterization, and have enabled several approaches that are suitable for performing on-line characterization.

Vibration analysis has been proven for its good on-line capabilities in characterizing the properties of anisotropic materials. Among many vibration tests, modal vibration testing pro-

vides rapid, inexpensive characterization of both elastic and viscoelastic properties for design and manufacturing. The metrics based on modal parameters are not well suited to the resolution of inverse, nonlinear problems. The nonlinear behavior can be characterized from mechanical testing by using specific test configurations. Characterization methods based on field measurements treat specimens as continua and allow for more flexibility in terms of test configurations. Despite such flexibility, most of the characterization methods are off-line and sensitive to the uncertainties in these measurements. While implicit modeling methodology using trained NN is capable of performing on-line nonlinear characterization, this methodology, however, suffers from the requirement for a considerable amount of training data.

The results of this literature review have identified a need for an efficient, nonlinear characterization method with better robustness to the existence of uncertainties in an on-line characterization framework. This dissertation aims to construct the robust and yet efficient characterization process; beginning with the next Chapter which provides an overview of the energy-based characterization method through full-field measurements, and discusses the adaptability of the methods to the on-line framework in a mathematical formulation point of view.

Chapter 3

Energy-based Characterization and Full-field Measurements

This Chapter presents an overview of the energy-based characterization of anisotropic materials and the derivation of full-field measurements related to this characterization. The elastic constants of anisotropic materials are determined based on the principle of energy conservation, and thus require the measurement of boundary force, full-field displacements, and full-field strains. The full-field measurements are derived from camera images of the specimen, which is marked with series of uniformly spaced dots. A common dots tracking approach is applied to derive full-field displacements and strains. The contemporary deterministic energy-based characterization approach, which integrates the pseudo-inverse calculation and singular value decomposition (SVD) to determine the elastic constants, is also presented in this chapter.

This chapter is outlined as follows. In Section 3.1, the standard energy-based characterization formulation is detailed for determining the elastic constants of anisotropic materials. Section 3.2 briefly describes the derivation of full-field measurements using the dot tracking approach. This includes the transformation of full-field measurements to a generalized common coordinate system by implementing a projective transformation approach. This derivation is followed by the deterministic energy-based characterization approach based on the pseudo-inverse calculation and SVD, detailed in Section 3.3.

3.1 Derivation of Energy-based Characterization

This section derives a review of the standard energy-based characterization of anisotropic materials.

3.1.1 Elastic Moduli of Anisotropic Materials

The energy-based characterization represents the stress-strain constitutive relationships in terms of elastic moduli. As one of the most popularly used anisotropic materials, consider symmetric angle-ply laminate, which consists of two types of lamina, each with a fiber orientation of θ or $-\theta$. The unidirectional lamina, under plane stress deformations, defines the material coordinate system as $\{M\}$ and relates stresses and strains in the elastic regime as

$$\begin{bmatrix} \sigma_1 \\ \sigma_2 \\ \sigma_6 \end{bmatrix} = \begin{bmatrix} q_{11} & q_{12} & 0 \\ q_{12} & q_{22} & 0 \\ 0 & 0 & q_{66} \end{bmatrix} \begin{bmatrix} \varepsilon_1 \\ \varepsilon_2 \\ \varepsilon_6 \end{bmatrix}, \quad (3.1)$$

or in matrix-vector form

$$\{M\}\boldsymbol{\sigma} = \{M\}\mathbf{Q}\{M\}\boldsymbol{\varepsilon}, \quad (3.2)$$

where $\{M\}\boldsymbol{\sigma}$, $\{M\}\mathbf{Q}$ and $\{M\}\boldsymbol{\varepsilon}$ contain the stress, constitutive and strain components with respect to the material coordinate system $\{M\}$, appears as the left superscript of the notations. The non-zero components of the matrix $\{M\}\mathbf{Q}$ are defined as

$$\{M\}\mathbf{q} = [q_{11} \quad q_{22} \quad q_{12} \quad q_{66}]^\top = \left[\frac{E_1}{1 - v_{12}^2 \frac{E_2}{E_1}} \quad \frac{E_2}{1 - v_{12}^2 \frac{E_2}{E_1}} \quad \frac{v_{12} E_2}{1 - v_{12}^2 \frac{E_2}{E_1}} \quad G_{12} \right]^\top, \quad (3.3)$$

where E_1 and E_2 are the Young's moduli along the principal material axes 1 and 2, and G_{12} is the shear modulus that characterizes the change of angle between the two principal directions. The elastic constants $\{M\}\mathbf{q}$ and the traditional set of elastic moduli $[E_1, E_2, v_{12}, G_{12}]$ are invertible and provide bidirectional transformability. To characterize the linear elasticity of the anisotropic materials, the remainder of this chapter treats $\{M\}\mathbf{q}$ as the targeted unknown elastic constants.

Given the stress-strain relationship in Equation (3.1), the stress-strain relationship of the symmetric angle-ply laminate with a fiber orientation of $\pm\theta$ can be described with $\{M\}\mathbf{q}$ in the global coordinate system $\{G\}$ aligned to the material principal axes as:

$$\begin{bmatrix} \sigma_x \\ \sigma_y \\ \sigma_s \end{bmatrix} = \begin{bmatrix} Q_{xx}(\theta; {}^M\mathbf{q}) & Q_{xy}(\theta; {}^M\mathbf{q}) & Q_{xs}(\theta; {}^M\mathbf{q}) \\ Q_{xy}(\theta; {}^M\mathbf{q}) & Q_{yy}(\theta; {}^M\mathbf{q}) & Q_{ys}(\theta; {}^M\mathbf{q}) \\ Q_{xs}(\theta; {}^M\mathbf{q}) & Q_{ys}(\theta; {}^M\mathbf{q}) & Q_{ss}(\theta; {}^M\mathbf{q}) \end{bmatrix} \begin{bmatrix} \varepsilon_x \\ \varepsilon_y \\ \varepsilon_s \end{bmatrix}. \quad (3.4)$$

The matrix-vector form of the stress-strain relationship in the global coordinate system is defined as

$${}^G\boldsymbol{\sigma} = {}^G\mathbf{Q}(\theta; {}^M\mathbf{q}) {}^G\boldsymbol{\varepsilon}, \quad (3.5)$$

where the components of the constitutive matrix ${}^G\mathbf{Q}(\cdot)$ given in the Voigt notation,

$${}^G\mathbf{q}(\cdot) \equiv [q_{xx}(\cdot) \ q_{yy}(\cdot) \ q_{ss}(\cdot) \ q_{xy}(\cdot) \ q_{xs}(\cdot) \ q_{ys}(\cdot)]^\top, \quad (3.6)$$

are linearly related to those in the material coordinates system [1] as

$${}^G\mathbf{q}(\theta; {}^M\mathbf{q}) = {}^M\mathbf{H}(\theta) {}^M\mathbf{q}. \quad (3.7)$$

The transformation matrix ${}^M\mathbf{H}$ is given by

$$\begin{aligned} {}^M\mathbf{H}(\theta) &= \begin{bmatrix} \mathbf{h}_1(\theta)^\top \\ \mathbf{h}_2(\theta)^\top \\ \mathbf{h}_3(\theta)^\top \\ \mathbf{h}_4(\theta)^\top \\ \mathbf{h}_5(\theta)^\top \\ \mathbf{h}_6(\theta)^\top \end{bmatrix} = \begin{bmatrix} h_{11}(\theta) & h_{12}(\theta) & h_{13}(\theta) & h_{14}(\theta) \\ h_{21}(\theta) & h_{22}(\theta) & h_{23}(\theta) & h_{24}(\theta) \\ h_{31}(\theta) & h_{32}(\theta) & h_{33}(\theta) & h_{34}(\theta) \\ h_{41}(\theta) & h_{42}(\theta) & h_{43}(\theta) & h_{44}(\theta) \\ h_{51}(\theta) & h_{52}(\theta) & h_{53}(\theta) & h_{54}(\theta) \\ h_{61}(\theta) & h_{62}(\theta) & h_{63}(\theta) & h_{64}(\theta) \end{bmatrix}, \\ &= \begin{bmatrix} m^4 & n^4 & 4n^2m^2 & 2n^2m^2 \\ n^4 & m^4 & 4n^2m^2 & 2n^2m^2 \\ n^2m^2 & n^2m^2 & -2n^2m^2 + n^4 + m^4 & -2n^2m^2 \\ n^2m^2 & n^2m^2 & -4n^2m^2 & n^4 + m^4 \\ m^3n & -mn^3 & -2mn(m^2 - n^2) & -mn(m^2 - n^2) \\ mn^3 & -m^3n & 2mn(m^2 - n^2) & mn(m^2 - n^2) \end{bmatrix}, \end{aligned} \quad (3.8)$$

with $m = \cos \theta$ and $n = \sin \theta$.

The subsequent Sections in this Chapter address variables and parameters in the global coordinate system. The linear stress-strain relationship (3.5) will be adopted in the following form:

$$\boldsymbol{\sigma} = \mathbf{Q}(\theta; \mathbf{q}_M) \boldsymbol{\varepsilon}, \quad (3.9)$$

by dropping the notation of the global coordinate system $\{G\}$ and subscripting the material coordinate system $\{M\}$ as M .

3.1.2 Principle of Energy Conservation

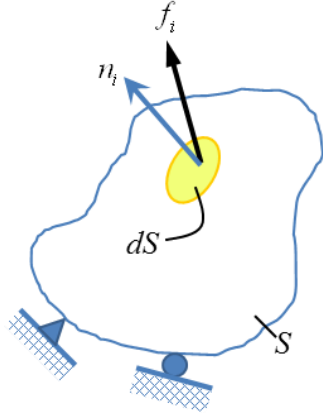


Figure 1 Elastic body subjected to surface force f_i .

This Section presents the concept of the principle of energy conservation. Figure 1 shows the body, S , and the forces f_i acting on the body. The potential energy of the external loads by the force f_i through the displacement u_i on the surface dS is given by

$$W = - \int_S f_i u_i dS, i = \{x, y, z\}. \quad (3.10)$$

Decomposing the deformation into K times deformation results in a set of equations results in

$$W^k = - \int_S f_i^k u_i^k dS, \forall k \in \{1, \dots, K\}. \quad (3.11)$$

The potential energy of the external loads at time step k is formed from the quantity at time step $k-1$, which is denoted as

$$W^{k-1} = - \int_S f_i^{k-1} u_i^{k-1} dS. \quad (3.12)$$

When the deformation continues from time step $k-1$ to k , Equation (3.11) is reformulated as

$$\begin{aligned}
W^k &= - \int_S f_i^k u_i^k dS \\
&= - \int_S (f_i^{k-1} + \Delta f_i^k)(u_i^{k-1} + \Delta u_i^k) dS \\
&= - \int_S (f_i^{k-1} u_i^{k-1} + \Delta f_i^k u_i^{k-1} + \Delta f_i^k \Delta u_i^k + f_i^{k-1} \Delta u_i^k) dS
\end{aligned} \tag{3.13}$$

where the increment Δ indicates the change of quantity (\cdot) from time step $k-1$ to k :

$$\Delta(\cdot)^k = (\cdot)^k - (\cdot)^{k-1}. \tag{3.14}$$

The incremental work potential is defined as the difference between Equations (3.12) and (3.13):

$$\begin{aligned}
\Delta W^k &= W^k - W^{k-1} \\
&= - \int_S (f_i^{k-1} u_i^{k-1} + \Delta f_i^k u_i^{k-1} + \Delta f_i^k \Delta u_i^k + f_i^{k-1} \Delta u_i^k) dS + \int_S f_i^{k-1} u_i^{k-1} dS, \\
&= - \int_S (f_i^{k-1} \Delta u_i^k + \Delta f_i^k u_i^{k-1} + \Delta f_i^k \Delta u_i^k) dS
\end{aligned} \tag{3.15}$$

After deriving the incremental work potential from the force and displacement, the incremental strain energy is derived next. The elastic strain energy of the body volume V is denoted as

$$U = \frac{1}{2} \int_V \sigma_{ij} \varepsilon_{ij} dV, \tag{3.16}$$

Similarly, the incremental strain energy at time step k is derived by the incremental stress and strain, i.e. $\Delta \sigma_{ij}$ and $\Delta \varepsilon_{ij}$, as

$$\Delta U^k = \frac{1}{2} \int_V (\sigma_{ij}^{k-1} \Delta \varepsilon_{ij}^k + \Delta \sigma_{ij}^k \varepsilon_{ij}^{k-1} + \Delta \sigma_{ij}^k \Delta \varepsilon_{ij}^k) dV. \tag{3.17}$$

The relationship, between the strain energy and the work, is formed based on the assumption that the work performed on an elastic structure in equilibrium by statically applied external forces is entirely converted to the work done by internal forces, or the strain energy stored in the structure [137]. The principle of energy conservation implies that the strain energy is equal to the work done by the external loads which increase uniformly from zero. When there are no initial strains and initial stresses, the external work is represented by half of the potential energy of the loads [138]. This principle thus yields the expression of the incremental terms of strain energy and external work as follows:

$$\Delta U^k + \frac{1}{2} \Delta W^k = 0. \tag{3.18}$$

Substitution of Equations (3.17) and (3.15) into Equation (3.18) yields:

$$\frac{1}{2} \int_V (\sigma_{ij}^{k-1} \Delta \varepsilon_{ij}^k + \Delta \sigma_{ij}^k \varepsilon_{ij}^{k-1} + \Delta \sigma_{ij}^k \Delta \varepsilon_{ij}^k) dV = \frac{1}{2} \int_S (f_i^{k-1} \Delta u_i^k + f_i^k u_i^{k-1} + \Delta f_i^k \Delta u_i^k) dS . \quad (3.19)$$

The components of the stress tensor in every point of the body satisfy the equilibrium equations

$$\sigma_{ij,j} = 0, i, j = \{x, y, z\} . \quad (3.20)$$

The Voigt notation represents the stress tensor in terms of the boundary force as

$$f_i = \sigma_{ij} n_j , \quad (3.21)$$

where n_j is a component of the normal vector \mathbf{n} , as shown in Figure 1, perpendicular to the surface dS .

Equations (3.20) and (3.21) derive the terms in Equation (3.19) as follows

$$\int_S f_i^{k-1} \Delta u_i^k dS = \int_S \sigma_{ij}^{k-1} n_j \Delta u_i^k dS = \int_V \sigma_{ij}^{k-1} \Delta u_{i,j}^k dV = \int_V \sigma_{ij}^{k-1} \Delta \varepsilon_{ij}^k dV , \text{ and} \quad (3.22)$$

$$\int_S \Delta f_i^k u_i^{k-1} dS = \int_S \Delta \sigma_{ij}^k n_j u_i^{k-1} dS = \int_V \Delta \sigma_{ij}^k u_{i,j}^{k-1} dV = \int_V \Delta \sigma_{ij}^k \varepsilon_{ij}^{k-1} dV . \quad (3.23)$$

Substitution of Equations (3.22) and (3.23) reduces Equation (3.19) to

$$\frac{1}{2} \int_V (\Delta \sigma_{ij}^k \Delta \varepsilon_{ij}^k) dV = \frac{1}{2} \int_S (\Delta f_i^k \Delta u_i^k) dS . \quad (3.24)$$

or, equivalently,

$$U_\Delta^k = W_\Delta^k . \quad (3.25)$$

where

$$U_\Delta^k = \frac{1}{2} \int_V (\Delta \boldsymbol{\sigma}^{k\top} \Delta \boldsymbol{\varepsilon}^k) dV , \quad (3.26)$$

$$W_\Delta^k = \frac{1}{2} \int_S (\Delta \mathbf{f}^{k\top} \Delta \mathbf{u}^k) dS . \quad (3.27)$$

The relationship between Equations (3.26) and (3.27), as denoted by Equation (3.25), becomes the foundation of the energy-based characterization of anisotropic materials. Substitution of Equation (3.9) into Equation (3.26) yields the strain energy term, which is rewritten as the sum of strain energies each combined with elastic constant:

$$\begin{aligned}
U_{\Delta}^k = & \frac{t}{2} \left\{ Q_{xx}(\theta, \mathbf{q}_M) \int_S (\Delta \varepsilon_x^k)^2 dS + Q_{yy}(\theta, \mathbf{q}_M) \int_S (\Delta \varepsilon_y^k)^2 dS \right. \\
& + Q_{ss}(\theta, \mathbf{q}_M) \int_S (\Delta \varepsilon_s^k)^2 dS + 2Q_{xy}(\theta, \mathbf{q}_M) \int_S \Delta \varepsilon_x^k \cdot \Delta \varepsilon_y^k dS , \\
& \left. + 2Q_{xs}(\theta, \mathbf{q}_M) \int_S \Delta \varepsilon_x^k \cdot \Delta \varepsilon_s^k dS + 2Q_{ys}(\theta, \mathbf{q}_M) \int_S \Delta \varepsilon_y^k \cdot \Delta \varepsilon_s^k dS \right\}
\end{aligned} \quad (3.28)$$

where t is the thickness of the body.

Introduction of the material coordinate system further yields

$$U_{\Delta}^k = \mathbf{g}(\Delta \boldsymbol{\varepsilon}^k; \theta)^\top \mathbf{q}_M, \quad (3.29)$$

where the strain energy coefficient vector $\mathbf{g}(\Delta \boldsymbol{\varepsilon}^k; \theta)$ is described as

$$\begin{aligned}
\mathbf{g}(\Delta \boldsymbol{\varepsilon}^k; \theta) = & \frac{t}{2} \left\{ \left[\int_S (\Delta \varepsilon_x^k)^2 dS \right] \mathbf{h}_1(\theta) + \left[\int_S (\Delta \varepsilon_y^k)^2 dS \right] \mathbf{h}_2(\theta) \right. \\
& + \left[\int_S (\Delta \varepsilon_s^k)^2 dS \right] \mathbf{h}_3(\theta) + 2 \left(\int_S \Delta \varepsilon_x^k \cdot \Delta \varepsilon_y^k dS \right) \mathbf{h}_4(\theta) . \\
& \left. + 2 \left(\int_S \Delta \varepsilon_x^k \Delta \varepsilon_s^k dS \right) \mathbf{h}_5(\theta) + 2 \left(\int_S \Delta \varepsilon_y^k \Delta \varepsilon_s^k dS \right) \mathbf{h}_6(\theta) \right\}
\end{aligned} \quad (3.30)$$

Substitution of Equation (3.29) into Equation (3.25) yields a linear equation:

$$\mathbf{g}(\Delta \boldsymbol{\varepsilon}^k; \theta)^\top \mathbf{q}_M = W_{\Delta}^k. \quad (3.31)$$

Implementation of the set of these equations over the K times deformation for the identification of \mathbf{q}_M is the basis of the energy-based characterization. To solve for the unknown elastic constants in Equation (3.31), a deterministic approach, presented in [107-109], is applied. Its derivation can be found at the end of this Chapter.

3.2 Full-field Measurements

In conjunction with previously described formulation of energy-based characterization, full-field strain and displacement measurements are required to derive the strain energy coefficient $\mathbf{g}(\Delta \boldsymbol{\varepsilon}^k; \theta)$, as presented in Equation (3.30), and the external work term W_{Δ}^k , as presented in Equation (3.27). The full-field measurements in this dissertation are derived by tracking the movement of dots marked on the specimen over discretized time steps. Figure 2 shows a schematic diagram of the deforming process of a specimen, with three dots marked and deformed from the initial step, from time step 1 to time step k . While the specimen is deforming, a camera,

identified here as the $\{c_l\}$ th camera, takes an image of the specimen at each time step and identifies the location of the dots by calculating the centroid of each dot. Assuming that in a total number of n_t dots marked on the specimen, the state of the $\{j \in n_t\}$ th dot at step k is defined by

$$\mathbf{x}_j^k \equiv [x_j^k, y_j^k]^\top. \quad (3.32)$$

The centroids derived from the image at time step k represent the \mathbf{x}_j^k as

$${}^{(I_l)}\mathbf{x}_j^k \equiv [{}^{(c_l)}x_j^k, {}^{(c_l)}y_j^k]^\top. \quad (3.33)$$

where ${}^{(I_l)}(\cdot)$ denotes the quantity (\cdot) that is derived from the image of the $\{c_l\}$ th camera. Since the centroids are directly identified from the pixel coordinate system, homography transformation of the centroids is subsequently applied to identify the centroids in a global coordinate system on a specimen.

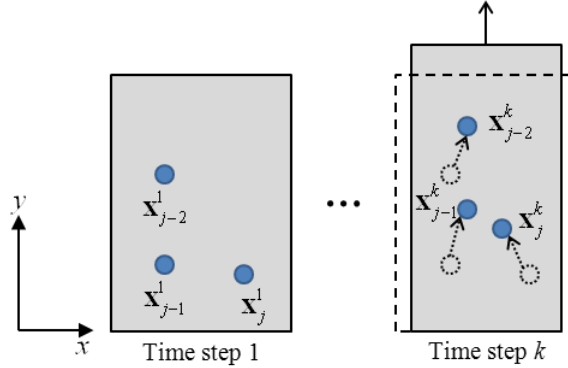


Figure 2 Specimen deformed from time step 1 to time step k .

3.2.1 Homography Transformation

Homography, a transformation used in projective geometry [161], is performed to map the centroid ${}^{(I_l)}\mathbf{x}_j^k$ from the pixel coordinate system to the global coordinate system. The identified centroid in the global coordinate system, identified as ${}^{(c_l)}\mathbf{x}_j^k$, is transformed by multiplying a homography matrix ${}^{(I_l)}\mathbf{H}$ to ${}^{(I_l)}\mathbf{x}_j^k$, i.e.:

$${}^{(c_l)}\mathbf{x}_j^k = {}^{(c_l)}\mathbf{H} {}^{(I_l)}\mathbf{x}_j^k \quad (3.34)$$

where $\{c_l\}(\cdot)$ indicates the transformed quantity (\cdot) derived from the $\{c_l\}$ th camera. The homography matrix $\{c_l\}_{\{I_l\}} \mathbf{H}$ provides a one-to-one mapping of dots, and relates $\{c_l\} \mathbf{x}_j^k$ and $\{I_l\} \mathbf{x}_j^k$ by

$$\begin{bmatrix} \{c_l\} \\ x_j^k \\ y_j^k \\ 1 \end{bmatrix}_{\{I_l\}} = \begin{bmatrix} H_{11} & H_{11} & H_{13} \\ H_{21} & H_{22} & H_{23} \\ H_{31} & H_{32} & H_{33} \end{bmatrix}^{\{I_l\}} \begin{bmatrix} x_j^k \\ y_j^k \\ 1 \end{bmatrix} \quad (3.35)$$

Various approaches have been proposed to construct the homography matrix and to describe how a homography matrix can be decomposed into translation and rotation. This dissertation derives the homography matrix from the image processing toolbox in Matlab via the following steps:

- (1) Measure four dot locations from the corner of the image (or local) coordinate system;
- (2) Choose four corresponding dots at the global coordinate system; and
- (3) Build $\{c_l\}_{\{I_l\}} \tilde{\mathbf{H}}$ based on the rotation and translation between the four local dot locations and their corresponding global dot locations.

3.2.2 Full-field Displacements and Strains

Referring back to Figure 2, the displacement at the j th dot, defined by $\mathbf{u}_j^k \equiv \left[(u_x)_j^k, (u_y)_j^k \right]^\top$, is measured by identifying the difference between the measured \mathbf{x}_j at time step k and time step 1, i.e., $\{c_l\} \mathbf{x}_j^1$ and $\{c_l\} \mathbf{x}_j^k$:

$$\{c_l\} \mathbf{u}_j^k = \{c_l\} \mathbf{x}_j^k - \{c_l\} \mathbf{x}_j^1. \quad (3.36)$$

A total number of n_m points are numerically created to cover the whole specimen, such that the displacement/strain of these created points, derived based on the marked dots, can represent the deformation over the entire specimen area. Thus, the displacement calculated at the $\{m \in n_m\}$ th created point, i.e. $\mathbf{x}_m^k \equiv [x_m^k, y_m^k]^\top$, is describable by the deformation functions [87] as

$$\mathbf{u}_m^k = \sum_{j=1}^{n_l} N_{jm} \{c_l\} \mathbf{u}_j^k, \quad (3.37)$$

and the measured full-field strain is computed by

$$\boldsymbol{\epsilon}_m^k = \left[\sum_{j=1}^{n_t} \frac{\partial N_{jm}^k}{\partial x} (u_x)_j^k, \sum_{j=1}^{n_t} \frac{\partial N_{jm}^k}{\partial y} (u_y)_j^k, \frac{1}{2} \sum_{j=1}^{n_t} \frac{\partial N_{jm}^k}{\partial x} (u_y)_j^k + \frac{1}{2} \sum_{j=1}^{n_t} \frac{\partial N_{jm}^k}{\partial y} (u_x)_j^k \right]^\top, \quad (3.38)$$

where $N_{jm}^k = N_j(\mathbf{x}_m^k)$ is the shape function evaluated at $\mathbf{x} = \mathbf{x}_m^k$ using any available mesh-free or finite element method. Together with the measured boundary force, the full-field displacement and strain measurements, which are derived from Equations (3.37) and (3.38), provide sufficient measurements to the energy-based characterization in Equation (3.31) for determining the elastic constants \mathbf{q}_M .

3.3 Deterministic Energy-based Characterization Approach

3.3.1 Pseudo-inverse Calculation

A deterministic approach [107-109], based on the pseudo-inverse calculation, can be employed to identify \mathbf{q}_M from the previously defined energy-based characterization formulations. Consider that a specimen is loaded with force and K sets of external work and full-field measurements of these sensors have been obtained. From the $(k-1)$ th and $k (\in \{1, \dots, K\})$ th readings of the boundary displacements, \mathbf{u}^{k-1} and \mathbf{u}^k , and those of the boundary forces, \mathbf{f}^{k-1} and \mathbf{f}^k , the incremental external work at every time step k is derived by substituting the measured $\Delta\mathbf{u}^k$ and $\Delta\mathbf{f}^k$ into Equation (3.27) to yield

$$\tilde{W}_\Delta^k = \frac{1}{2} \sum_l \Delta \tilde{\mathbf{f}}_l^{k\top} \Delta \tilde{\mathbf{u}}_l^k, \quad (3.39)$$

where $(\tilde{\cdot})$ represents the measured data of (\cdot) or the data derived from the measurement. Given the strain vector obtained at k th and $(k-1)$ th readings as $\tilde{\boldsymbol{\epsilon}}^{k-1}$ and $\tilde{\boldsymbol{\epsilon}}^k$, respectively, the increment of the incremental strain energy is similarly calculated as

$$\tilde{U}_\Delta^k \equiv \mathbf{g}(\Delta \tilde{\boldsymbol{\epsilon}}^k; \theta)^\top \mathbf{q}_M. \quad (3.40)$$

From Equations (3.39) and (3.40), the energy-based characterization results in a set of linear equations:

$$\mathbf{g}(\Delta \tilde{\boldsymbol{\epsilon}}^k; \theta)^\top \mathbf{q}_M = \tilde{W}_\Delta^k, \forall k \in \{1, \dots, K\}. \quad (3.41)$$

Having the set of linear equations constructed directly from the measurements, the deterministic approach allows for the reformulation of this equation in matrix-vector form:

$$\mathbf{G}(\Delta\tilde{\boldsymbol{\epsilon}}^{1:K}; \theta) \mathbf{q}_M = \tilde{\mathbf{w}}^{1:K}. \quad (3.42)$$

where the full-field strains and external work terms are defined by

$$\mathbf{G}(\Delta\tilde{\boldsymbol{\epsilon}}^{1:K}; \theta) \equiv \left[\mathbf{g}(\Delta\tilde{\boldsymbol{\epsilon}}^1; \theta), \dots, \mathbf{g}(\Delta\tilde{\boldsymbol{\epsilon}}^K; \theta) \right]^\top \quad (3.43)$$

$$\tilde{\mathbf{w}}^{1:K} \equiv \left[\tilde{W}_\Delta^1, \dots, \tilde{W}_\Delta^K \right]^\top. \quad (3.44)$$

As the matrix $\mathbf{G}(\Delta\tilde{\boldsymbol{\epsilon}}^{1:K}; \theta)$ is of dimensions $K \times 4$, the deterministic approach solves the elastic constants \mathbf{q}_M by

$$\mathbf{q}_M = \mathbf{G}(\Delta\tilde{\boldsymbol{\epsilon}}^{1:K}; \theta)^+ \tilde{\mathbf{w}}^{1:K}, \quad (3.45)$$

where

$$\mathbf{G}(\Delta\tilde{\boldsymbol{\epsilon}}^{1:K}; \theta)^+ = \left\{ \mathbf{G}(\Delta\tilde{\boldsymbol{\epsilon}}^{1:K}; \theta)^\top \mathbf{G}(\Delta\tilde{\boldsymbol{\epsilon}}^{1:K}; \theta) \right\}^{-1} \mathbf{G}(\Delta\tilde{\boldsymbol{\epsilon}}^{1:K}; \theta)^\top \quad (3.46)$$

is the pseudo-inverse of $\mathbf{G}(\Delta\tilde{\boldsymbol{\epsilon}}^{1:K}; \theta)$. It is to be noted that the distinguishability of the identified elastic constants depends upon the rank of the matrix $\mathbf{G}(\Delta\tilde{\boldsymbol{\epsilon}}^{1:K}; \theta)$. The study on the distinguishability and other properties of the identification problem can be found in [107-109].

3.3.2 Quantification

The deterministic approach utilizes singular value decomposition (SVD) to analyze the performance of the characterization results, in terms of uniqueness and distinguishability. The uniqueness of the characterization results determines if the matrix $\mathbf{G}(\Delta\tilde{\boldsymbol{\epsilon}}^{1:K}; \theta)$ in Equation (3.45) has an inverse matrix. The singular values of the matrix result from an SVD on the matrix:

$$\mathbf{G}(\Delta\tilde{\boldsymbol{\epsilon}}^{1:K}; \theta) = \tilde{\mathbf{U}} \tilde{\mathbf{S}} \tilde{\mathbf{V}}^\top \quad (3.47)$$

where $\tilde{\mathbf{U}} \in \Re^{K \times K}$ and $\tilde{\mathbf{V}} \in \Re^{4 \times 4}$ are orthogonal and $\tilde{\mathbf{S}} \in \Re^{K \times 4}$ is diagonal with real, non-negative singular values $\tilde{s}_i, \forall i \in \{1, \dots, 4\}$. The singular values are used to quantify the degree of unique-

ness of the characterization results, and thus quantify the uniqueness by a quantitative parameter F^u as follows.

$$F^u = \frac{\tilde{s}_{\min}}{\tilde{s}_{\max}}. \quad (3.48)$$

The less indifferent the singular values are from each other, the more unique the solution is, and thus increases the ability of the deterministic approach to distinguish all elastic constants that are seemingly close to each other.

3.3.3 Process Diagram

Figure 3 shows the process diagram of the numerical implementation of the deterministic energy-based characterization approach. Given $k = 2$, the predetermined boundary displacements $\tilde{\mathbf{u}}^2$ and forces $\tilde{\mathbf{f}}^2$ allow the incremental external work \tilde{W}_Δ^2 and the full-field strains $\Delta\tilde{\boldsymbol{\epsilon}}^2$ to be measured. The term $\mathbf{g}(\Delta\tilde{\boldsymbol{\epsilon}}^2; \theta)$ determined from $\Delta\tilde{\boldsymbol{\epsilon}}^2$ is combined with previous $\mathbf{g}(\Delta\tilde{\boldsymbol{\epsilon}}^k; \theta)$, such as $\mathbf{g}(\Delta\tilde{\boldsymbol{\epsilon}}^1; \theta)$ from $k = 1$, to form $\mathbf{G}(\Delta\tilde{\boldsymbol{\epsilon}}^{1:2}; \theta)$ that is used to derive the pseudo-inverse matrix $\mathbf{G}(\Delta\tilde{\boldsymbol{\epsilon}}^{1:2}; \theta)^+$. The measured \tilde{W}_Δ^1 combined with the previous \tilde{W}_Δ^k , such as \tilde{W}_Δ^1 to form $\tilde{\mathbf{w}}^{1:2}$, which is then multiplied with $\mathbf{G}(\Delta\tilde{\boldsymbol{\epsilon}}^{1:2}; \theta)^+$ to compute the elastic constants \mathbf{q}_M^2 . As a result of SVD, the deterministic approach utilizes the singular values $\tilde{s}_i, \forall i \in \{1, \dots, 4\}$, to compute the uniqueness of the characterization results F^u .

Figure 3 also illustrates the contribution of the deterministic approach based on the energy-based characterization formulation. The deterministic approach utilizes all the data measured in the past to determine the mean value of the elastic constants, and thus, its accuracy is dependent on the uniqueness of collected data.

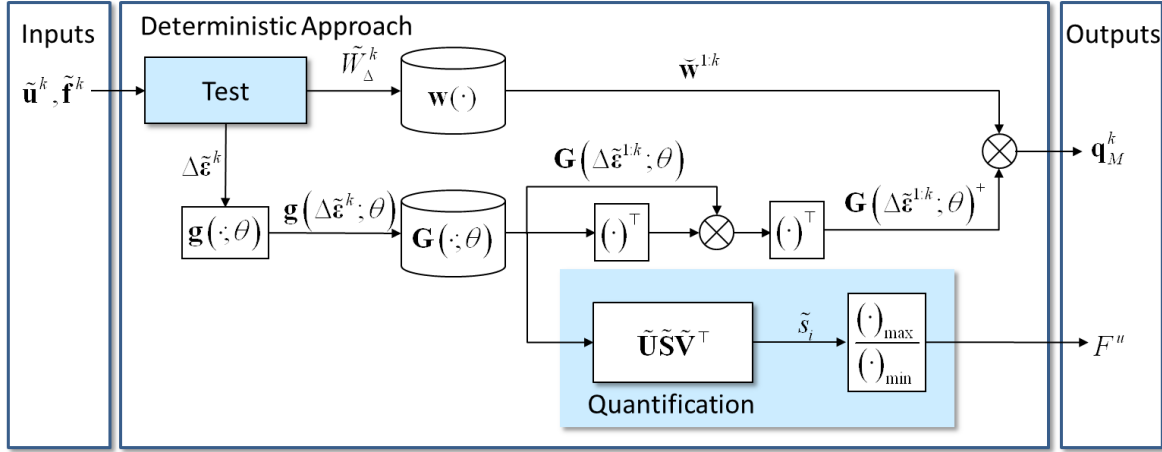


Figure 3 Schematic diagram of the deterministic energy-based characterization process.

3.4 Summary

In the beginning of this chapter, the details of the energy-based characterization formulation and the derivation of full-field measurements were presented. The energy-based characterization formulation, which is built upon the principle of energy conservation, formulates the elastic constants in terms of the boundary force and displacement, and full-field strains. The derivation of full-field measurements is capable of providing sufficient information for use with the energy-based characterization formulation to solve for the elastic constants. By collecting these measurements, a deterministic approach based on a pseudo-inverse calculation, is capable of determining the elastic constants in the energy-based characterization formulation, while quantifying the uniqueness of the measurements.

The characterization framework, proposed by this dissertation, is based on the energy-based characterization fundamentals and formulations. The next chapter uses the notations and fundamentals outlined in this Chapter and applies them to describe a stochastic linear characterization method, and the method is compared with the deterministic energy-based characterization approach in terms of efficiency under the effect of uncertainties.

Chapter 4

Stochastic Linear Characterization of Anisotropic Materials

This Chapter presents a stochastic linear characterization method that stochastically identifies the elastic constants of anisotropic materials by modeling the measurement noise and removing its effect unlike the deterministic energy-based characterization approach presented in the previous Chapter, which deterministically identifies the elastic constants directly from measurements. This method recursively estimates the elastic constants at every acquisition of measurements using a Kalman filter. Owing to the nonlinear expression of the measurement model, a Kalman gain has been newly derived and achieves optimal estimation. Since the variances in addition to the means are computed, the linear characterization method can not only identify the elastic constants, but also describe their certainty as an additional advantage.

This chapter is organized as follows. Section 4.1 describes the state transition and measurement models of the linear characterization method, based on the energy-based characterization formulations. The recursive mechanism of the measurement update that enables the on-line capability of the linear characterization method is covered in Section 4.2. Section 4.3 describes the numerical implementation of the linear characterization method. The results are then compared in Section 4.4 with the deterministic approach under various parametric studies.

4.1 State Transition Model and Measurement Model

Since the Kalman filter (KF) initially requires the determination of matrices in the state transition and the measurement models (see Appendix 1), the stochastic identification of elastic constants using KF starts with the formulations of a state transition model and measurement model. As the elastic constants do not change, the state transition model for the elastic constants is thus expressed with the identity matrix \mathbf{I} as

$$\mathbf{q}_M^k = \mathbf{I}\mathbf{q}_M^{k-1} + \mathbf{w}_q^{k-1} = \mathbf{I}\mathbf{q}_M^{k-1} \quad (4.1)$$

where $\mathbf{w}_q^{k-1} \sim N(\mathbf{0}, \mathbf{P}_q)$ since the covariance is zero, i.e. $\mathbf{P}_q = \mathbf{0}$.

As the noise of the sensed measurements introduces uncertainty to the measurement model, the measurement model must be developed by modeling all the sensors. The stochastic linear characterization method uses boundary displacement/force sensors and a full-field strain sensor, where the measured data of the external work and the full-field strain are expressed as

$$z_W^k = W_\Delta^k + v_W^k \quad (4.2)$$

$$\mathbf{z}_\epsilon^k = \Delta\boldsymbol{\epsilon}^k + \mathbf{v}_\epsilon^k, \quad (4.3)$$

where the uncertainties due to measurement noises are given by normal distributions with a zero mean, $v_W^k \sim N(0, P_W^k)$ and $\mathbf{v}_\epsilon^k \sim N(\mathbf{0}, \mathbf{P}_\epsilon^k)$. The true incremental external work W_Δ^k of Equation (4.2) is expressed in terms of $\mathbf{g}(\Delta\boldsymbol{\epsilon}^k; \theta)$ as shown in Equation (3.32). If we approximately relate the unknown true $\mathbf{g}(\Delta\boldsymbol{\epsilon}^k; \theta)$ to the measured $\mathbf{g}(\mathbf{z}_\epsilon^k; \theta)$ by

$$\mathbf{g}(\mathbf{z}_\epsilon^k; \theta) \approx \mathbf{g}(\Delta\boldsymbol{\epsilon}^k; \theta) + \mathbf{g}(\mathbf{v}_\epsilon^k; \theta), \quad (4.4)$$

where $\mathbf{g}(\mathbf{v}_\epsilon^k; \theta) \sim N(\mathbf{0}, \mathbf{P}_g)$, the substitution of Equation (4.4) into (3.32) and its substitution into Equation (4.2) constructs the measurement model as

$$z_W^k = [\mathbf{g}(\mathbf{z}_\epsilon^k; \theta) - \mathbf{g}(\mathbf{v}_\epsilon^k; \theta)]^\top \mathbf{q}_M^k + v_W^k \quad (4.5)$$

The problem of this measurement model is the inclusion of full-field noise in the coefficient, making the model nonlinear and thus disabling the optimal estimation of the elastic constants by the standard KF developed for linear systems.

4.2 Prediction and Correction

Having the state transition model (4.1) and measurement model (4.5) defined, the formulation of KF for the estimation of elastic constants results in the determination of the prediction and the correction processes as described in Appendix 1. Since the prediction of the constants does not introduce any uncertainty, the substitution of the state transition matrix into Equations (A1.4) and (A1.7), as expected, yields the prediction as an uninfluential process:

$$\mathbf{q}_M^{k|k-1} = \mathbf{I}\mathbf{q}_M^{k-1|k-1} = \mathbf{q}_M^{k-1|k-1} \quad (4.6)$$

$$\mathbf{P}^{k|k-1} = \mathbf{I}\mathbf{P}^{k-1|k-1}\mathbf{I}^\top + \mathbf{P}_{\mathbf{q}}^{k-1} = \mathbf{P}^{k-1|k-1}. \quad (4.7)$$

The correction, on the other hand, updates the estimation of the constants at every measurement. The substitution of Equation (4.5) into (A1.8) when the measurement is z_W^k yields the correction of the mean with the Kalman gain as

$$E\langle \mathbf{q}_M^k \rangle := E\langle \mathbf{q}_M^k \rangle + E\left\langle \mathbf{K}^k \left\{ z_W^k - [\mathbf{g}(\mathbf{z}_e^k; \theta) - \mathbf{g}(\mathbf{v}_e^k; \theta)]^\top \mathbf{q}_M^k - v_W^k \right\} \right\rangle \quad (4.8)$$

Since the expectations of the noises are all zero, the mean correction in KF is resultantly simplified as

$$\mathbf{q}_M^{k|k} = \mathbf{q}_M^{k|k-1} + \mathbf{K}^k \left[z_W^k - \mathbf{g}(\mathbf{z}_e^k; \theta)^\top \mathbf{q}_M^{k|k-1} \right] \quad (4.9)$$

The correction of covariance starts with the derivation of the residual:

$$\begin{aligned} \mathbf{e}^{k|k} &= \mathbf{q}_M - \mathbf{q}_M^{k|k} = \mathbf{q}_M - \mathbf{q}_M^{k|k-1} - \mathbf{K}^k \left\{ [\mathbf{g}(\mathbf{z}_e^k; \theta) - \mathbf{g}(\mathbf{v}_e^k; \theta)]^\top \mathbf{q}_M^k + v_W^k - \mathbf{g}(\mathbf{z}_e^k; \theta)^\top \mathbf{q}_M^{k|k-1} \right\} \\ &= \left[\mathbf{I} - \mathbf{K}^k \mathbf{g}(\mathbf{z}_e^k; \theta)^\top \right] \mathbf{e}^{k|k-1} - \mathbf{K}^k \left[v_W^k - \mathbf{g}(\mathbf{v}_e^k; \theta)^\top \mathbf{q}_M^k \right]. \end{aligned} \quad (4.10)$$

The covariance, expressed in terms of the difference, is simplified through mutual independence of various noises as

$$\begin{aligned}
E \langle \mathbf{e}^{k|k} \mathbf{e}^{k|k\top} \rangle &= E \left\langle \left\{ \left[\mathbf{I} - \mathbf{K}^k \mathbf{g}(\mathbf{z}_\epsilon^k; \theta)^\top \right] \mathbf{e}^{k|k-1} - \mathbf{K}^k \left[v_W^k - \mathbf{g}(\mathbf{v}_\epsilon^k; \theta) \mathbf{q}_M^k \right] \right\} \right. \\
&\quad \left. \left\{ \left[\mathbf{I} - \mathbf{K}^k \mathbf{g}(\mathbf{z}_\epsilon^k; \theta)^\top \right] \mathbf{e}^{k|k-1} - \mathbf{K}^k \left[v_W^k - \mathbf{g}(\mathbf{v}_\epsilon^k; \theta) \mathbf{q}_M^k \right] \right\}^\top \right\rangle \\
&= \left[\mathbf{I} - \mathbf{K}^k \mathbf{g}(\mathbf{z}_\epsilon^k; \theta)^\top \right] E \left\langle \mathbf{e}^{k|k-1} \left(\mathbf{e}^{k|k-1} \right)^\top \right\rangle \left[\mathbf{I} - \mathbf{K}^k \mathbf{g}(\mathbf{z}_\epsilon^k; \theta)^\top \right]^\top \\
&\quad + \mathbf{K}^k E \left\langle \left[v_W^k - \mathbf{g}(\mathbf{v}_\epsilon^k; \theta)^\top \mathbf{q}_M^k \right] \left[v_W^k - \mathbf{g}(\mathbf{v}_\epsilon^k; \theta)^\top \mathbf{q}_M^k \right]^\top \right\rangle \mathbf{K}^{k\top} \\
&= \left[\mathbf{I} - \mathbf{K}^k \mathbf{g}(\mathbf{z}_\epsilon^k; \theta)^\top \right] E \left\langle \mathbf{e}^{k|k-1} \mathbf{e}^{k|k-1\top} \right\rangle \left[\mathbf{I} - \mathbf{K}^k \mathbf{g}(\mathbf{z}_\epsilon^k; \theta)^\top \right]^\top \\
&\quad + \mathbf{K}^k E \left\langle \left(v_W^k \right)^2 \right\rangle \mathbf{K}^{k\top} + \mathbf{K}^k E \left\langle \left[\mathbf{g}(\mathbf{v}_\epsilon^k; \theta)^\top \mathbf{q}_M^k \right]^2 \right\rangle \mathbf{K}^{k\top} \\
&= \left[\mathbf{I} - \mathbf{K}^k \mathbf{g}(\mathbf{z}_\epsilon^k; \theta)^\top \right] E \left\langle \mathbf{e}^{k|k-1} \mathbf{e}^{k|k-1\top} \right\rangle \left[\mathbf{I} - \mathbf{K}^k \mathbf{g}(\mathbf{z}_\epsilon^k; \theta)^\top \right]^\top \\
&\quad + \mathbf{K}^k E \left\langle \left(v_W^k \right)^2 \right\rangle \mathbf{K}^{k\top} + \mathbf{K}^k \left[\sum_{i=1}^4 \left(q_M^{k|k-1} \right)_i^2 E \left\langle g_i \left(\mathbf{v}_\epsilon^k; \theta \right)^2 \right\rangle \right] \mathbf{K}^{k\top}.
\end{aligned} \tag{4.11}$$

As a result, the correction of the covariance is given by

$$\begin{aligned}
\mathbf{P}^{k|k} &= \left[\mathbf{I} - \mathbf{K}^k \mathbf{g}(\mathbf{z}_\epsilon^k; \theta)^\top \right] \mathbf{P}^{k|k-1} \left[\mathbf{I} - \mathbf{K}^k \mathbf{g}(\mathbf{z}_\epsilon^k; \theta)^\top \right]^\top \\
&\quad + \mathbf{K}^k P_W^k \mathbf{K}^{k\top} + \mathbf{K}^k \left[\sum_{i=1}^4 \left(q_M^{k|k-1} \right)_i^2 \left(P_g^k \right)_i \right] \mathbf{K}^{k\top} \\
&= \mathbf{P}^{k|k-1} - \mathbf{P}^{k|k-1} \mathbf{g}(\mathbf{z}_\epsilon^k; \theta) \mathbf{K}^{k\top} - \mathbf{K}^k \mathbf{g}(\mathbf{z}_\epsilon^k; \theta)^\top \mathbf{P}^{k|k-1} \\
&\quad + \mathbf{K}^k \left\{ \mathbf{g}(\mathbf{z}_\epsilon^k; \theta)^\top \mathbf{P}^{k|k-1} \mathbf{g}(\mathbf{z}_\epsilon^k; \theta) + P_W^k + \left[\sum_{i=1}^4 \left(q_M^{k|k-1} \right)_i^2 \left(P_g^k \right)_i \right] \right\} \mathbf{K}^{k\top}.
\end{aligned} \tag{4.12}$$

Having the covariance correction derived, the Kalman gain that minimizes the covariance must make its trace differentiated partially with respect to the Kalman gain zero:

$$\begin{aligned}
\frac{\partial \text{Tr}(\mathbf{P}^{k|k})}{\partial \mathbf{K}^k} &= -2 \left[\mathbf{g}(\mathbf{z}_\epsilon^k; \theta)^\top \mathbf{P}^{k|k-1} \right]^\top \\
&\quad + 2 \mathbf{K}^k \left\{ \mathbf{g}(\mathbf{z}_\epsilon^k; \theta)^\top \mathbf{P}^{k|k-1} \mathbf{g}(\mathbf{z}_\epsilon^k; \theta) + P_W^k + \left[\sum_{i=1}^4 \left(q_M^{k|k-1} \right)_i^2 \left(P_g^k \right)_i \right] \right\} = 0.
\end{aligned} \tag{4.13}$$

The Kalman gain is consequently given by

$$\mathbf{K}^k = \mathbf{P}^{k|k-1\top} \mathbf{g}(\mathbf{z}_\epsilon^k; \theta) \left\{ \mathbf{g}(\mathbf{z}_\epsilon^k; \theta)^\top \mathbf{P}^{k|k-1} \mathbf{g}(\mathbf{z}_\epsilon^k; \theta) + P_W^k + \left[\sum_{i=1}^4 \left(q_M^{k|k-1} \right)_i^2 \left(P_g^k \right)_i \right] \right\}^{-1}. \tag{4.14}$$

Substitution of Equation (4.14) into (4.12) simplifies the covariance correction as

$$\mathbf{P}^{k|k} = \mathbf{P}^{k|k-1} - \mathbf{K}^k \mathbf{g}(\mathbf{z}_\epsilon^k; \theta)^\top \mathbf{P}^{k|k-1}. \quad (4.15)$$

The characterization method provides the proposed framework the recursive estimation mechanism to utilize the measurements obtained at every time step to create a new estimation, with the new estimate and its computed covariance recursively informing the prediction step of the following time step. The recursive estimation algorithms deliver the benefits of estimating the constants on-line with the test by the feed-forward architecture, inherited from the original Kalman filter, as shown in Appendix 1. The characterization method becomes computationally inexpensive since it requires only the last “best guess”, not the entire history of the probabilistic states of the estimated constants, strengthening its on-line capability for characterization.

4.3 Numerical Implementation

Figure 4 shows the schematic diagram of the numerical implementation of the stochastic linear characterization method. To be determined *a priori* in addition to the parameters appearing in the state transition model (4.1) and the measurement model (4.5) and the loading conditions of the material testing machine are the initial conditions of the mean $\mathbf{q}_M^{0|0}$ and the covariance $\mathbf{P}^{0|0}$, or the so-called *prior knowledge*.

Given $\mathbf{q}_M^{0|0}$, $\mathbf{P}^{0|0}$ and $k = 1$, the prediction updates them to $\mathbf{q}_M^{1|0}$ and $\mathbf{P}^{1|0}$ without any change. The predetermined loading then allows the increments of external work z_W^1 and the full-field strain \mathbf{z}_ϵ^1 to be measured. The term $\mathbf{g}(\mathbf{z}_\epsilon^1; \theta)$ determined from \mathbf{z}_ϵ^1 , together with $\mathbf{P}^{1|0}$, computes the Kalman gain \mathbf{K}^1 . The mean is updated to $\mathbf{q}_M^{1|1}$ from $\mathbf{q}_M^{1|0}$ by subtracting $\mathbf{g}(\mathbf{z}_\epsilon^1; \theta)^\top \mathbf{q}_M^{1|0}$ from z_W^1 and multiplying it by \mathbf{K}^1 , whereas the covariance is updated to $\mathbf{P}^{1|1}$ from $\mathbf{P}^{1|0}$ by subtracting $\mathbf{g}(\mathbf{z}_\epsilon^1; \theta)^\top \mathbf{P}^{1|0}$ multiplied by \mathbf{K}^1 from $\mathbf{P}^{1|0}$. The following prediction, $\mathbf{q}_M^{k|k-1}$ and $\mathbf{P}^{k|k-1}$, and update, $\mathbf{q}_M^{k|k}$ and $\mathbf{P}^{k|k}$, $k = \{2, 3, \dots\}$, can be carried out iteratively by setting $k := k + 1$ when the update is complete and providing new loading conditions.

The figure also illustrates the original contribution of the characterization method. While the conventional approach dealt with only the mean value deterministically, the characterization method also estimates the covariance on-line, removing the effect of measurement noise and allowing the estimation with certainty.

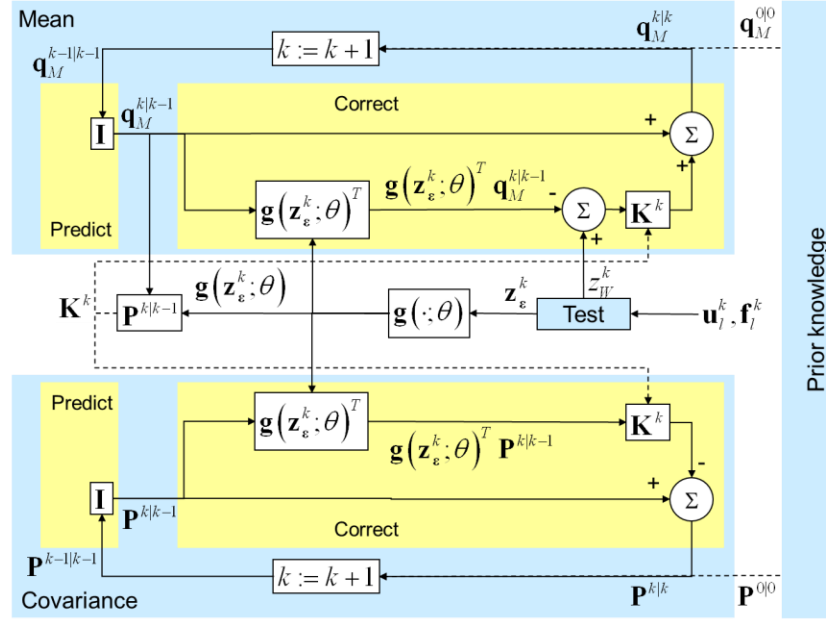


Figure 4 Numerical implementation of the stochastic linear characterization method.

4.4 Numerical Examples

This section investigates the effectiveness of the characterization method in two steps. The first step is aimed at the concept-proving of the characterization method where three parametric studies are carried out by solving an algebraic problem resembling the elastic constants identification problem. In the second and final step, the applicability of the characterization method to the elastic constants identification of an anisotropic material is examined.

4.4.1 Concept Proving by Algebraic Problem

The problem made in this section consists of the following two sets of equations:

$$\begin{aligned} \mathbf{z}_g^k &= \mathbf{g}^k + \mathbf{v}_g^k \\ z_w^k &= (\mathbf{g}^k)^T \mathbf{q} + v_w^k = (\mathbf{z}_g^k - \mathbf{v}_g^k)^T \mathbf{q} + v_w^k, \forall k \in \{1, \dots, K\}, \end{aligned} \quad (4.16)$$

where $\mathbf{q} = [q_1, q_2]^\top$ are the constants to estimate, and $\mathbf{g}^k = [g_1^k, g_2^k]^\top$ are the true multipliers, which are to resemble $\mathbf{g}(\Delta\boldsymbol{\varepsilon}^k; \theta)$ and take a variety of values according to

$$g_i^k = \mu_i^k (g_i^{\max} - g_i^{\min}) + g_i^{\min}, \forall i \in \{1, 2\}, \quad (4.17)$$

where $\mu_i^k \in [0, 1]$ is a uniformly distributed random value. \mathbf{z}_g^k and z_w^k are the measurements, and $\mathbf{v}_g^k \sim N(\mathbf{0}, \mathbf{P}_g)$ and $v_w^k \sim N(0, P_w)$ are the noises. Although the space of constants has been reduced to two dimensions to facilitate parametric studies, the equations are identical to Equations (4.1) and (4.3) and thus allow the examination of efficacy of the characterization method for the identification of elastic constants.

Table 1 lists the parameters used commonly to create measurements in the following three parametric studies. The measurements were created by firstly specifying \mathbf{q}^* and generating \mathbf{g}^k via Equation (4.17), and then adding noises with specified \mathbf{P}_g^* (specified variances $(P_g^*)_1$ and $(P_g^*)_2$ as \mathbf{P}_g^* is a diagonal matrix) and P_w^* . The measurements were created with constants $\mathbf{q}^* = [1000, 5000]^\top$. It is therefore expected that the characterization method finds constants around \mathbf{q}^* . The characterization method estimates constants by specifying the initial guess \mathbf{q}^{00} and \mathbf{P}^{00} and the covariance matrices for measurement noises \mathbf{P}_g and P_w .

Table 1 Parameters commonly used in the parametric studies of characterization method.

Parameter	Value
$[q_1^*, q_2^*]$	$[1000, 5000]$
$[g_1^{\min}, g_2^{\min}]$	$[0, 0]$
$[g_1^{\max}, g_2^{\max}]$	$[150, 150]$

4.4.1.1 Transitional Performance

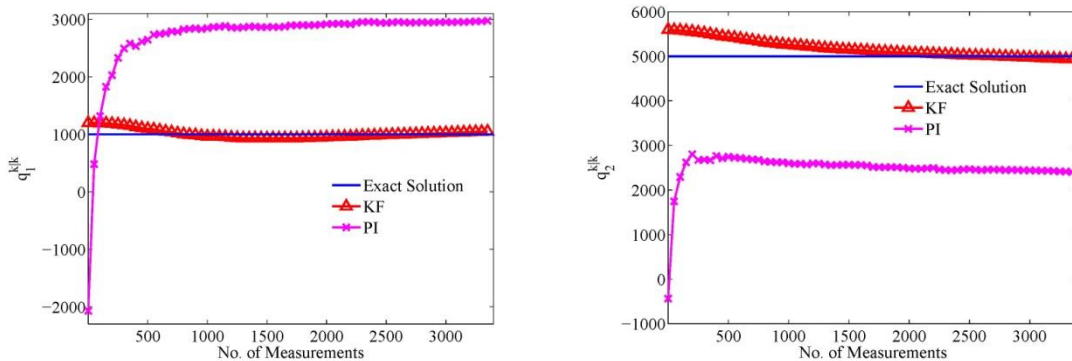
In order to investigate its transitional performance and the mechanism of estimation, the proposed framework was first applied to estimating the unknown constants when a particular set of parameters were chosen for the operation of the proposed framework and the creation of meas-

urements. Table 2 shows the variances and the prior estimates used in the proposed framework. In addition to the parameters specified in Table 1, the variances shown in the table were used to create the measurements. It is to be noted that the variances were chosen to create measurement noises exceeding 10% such that the identification of even only two parameters becomes erroneous. To compare its performance to those of conventional deterministic approaches, the deterministic approach presented in Section 3.4 was also used to estimate the constants from the same set of measurements.

Table 2 Parameters for test investigating transitional performance.

Parameter for Measurement	Value	Parameter for Proposed Framework	Value
$\left[\left(P_g^* \right)_1, \left(P_g^* \right)_2 \right]$	[20, 20]	$\left[\left(P_g \right)_1, \left(P_g \right)_2 \right]$	[20, 20]
P_w^*	20000	P_w^*	20000
		$\left[q_1^{0 0}, q_2^{0 0} \right]$	[1200, 5600]
		$\left[P_{11}^{0 0}, P_{22}^{0 0} \right]$	[1000, 1100]

Figures 5(a) and (b) show the transition of the two constants identified by the linear characterization method and the conventional deterministic approach. Note that \mathbf{q}^* is shown as Exact Solution. The results first show that both the characterization method and the deterministic approach converge as the number of measurements acquired increases. However, while the proposed framework settles to the exact solution within 5% error, the deterministic approach converges to values different from the exact solution by over 1500.



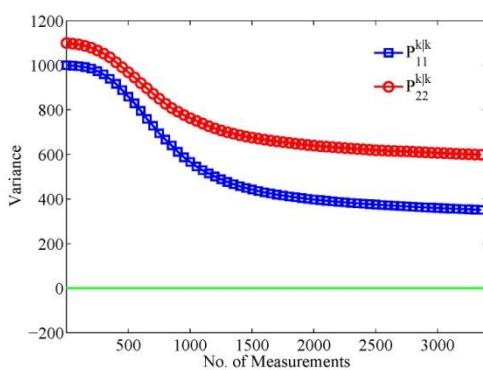
(a) q_1 (b) q_2

Figure 5 Transition of constants identified by the characterization method and the deterministic approach.

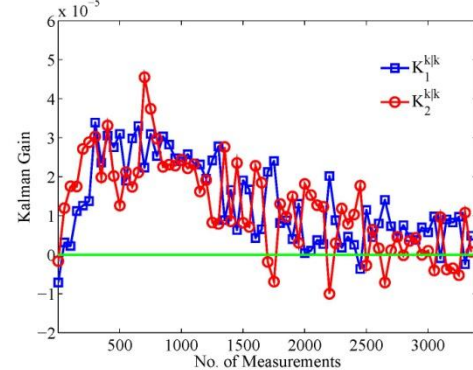
The effectiveness of the proposed framework can also be found by seeing the variances of the estimated constants in Figure 6(a). The stochastic linear characterization method estimates not only the constants, but also how certain the estimated constants are, unlike the deterministic approach. Moreover, it is shown that the characterization method reduces variances or increases certainty of estimation as the number of measurements acquired increases. To configure the mechanism of the characterization method to yield good converging estimates, the transition of Kalman gains, which converges to zero at the increase of the number of measurements, is shown in Figure 6(b). The KF determines the Kalman gain such that the trace of the covariance is minimized as indicated in Equation (4.13). This reduces the variances towards zero as shown in Figure 6(a), and Equation (4.14) gives the limit of the Kalman gain when the covariance approaches zero as

$$\lim_{P^{k|k-1} \rightarrow 0} \mathbf{K}^k = \mathbf{0} \quad (4.18)$$

as Figure 6(b) demonstrates. The substitution of the decreasing Kalman gain into Equation (4.9) results in the estimation of a converging mean.



(a) Covariance



(b) Kalman gain

Figure 6 Covariance updated by the Kalman gain.

4.4.1.2 Estimation at Different Noise Amplitudes

Having understood its effective converging performance and superiority to the conventional approach, the performance of the stochastic linear characterization method was next investigated by solving estimation problems each with a different set of measurement noises. Table 3 lists the parameters used to create measurements as well as those used to estimate the constants by the characterization method. Measurement noises for each estimation were created using a variance ranging from 0 to 40 for $(P_g^*)_i, \forall i \in \{1, 2\}$ and a variance ranging from 0 to 40000 for P_w^* , and the same variances were used in the characterization method. Using the correct information on the measurement noises and varying the amplitude of noise, it is possible to investigate whether the stochastic linear characterization method can estimate well regardless of the noise amplitude.

Table 3 Parameters for tests investigating noise effect ($x \in [0, 40]$, $y \in [0, 40000]$).

Parameter for Measurement	Value	Parameter for Proposed Framework	Value
$\left[(P_g^*)_1, (P_g^*)_2\right]$	$[x, x]$	$\left[(P_g)_1, (P_g)_2\right]$	$[x, x]$
P_w^*	y	P_w^*	y
		$\left[q_1^{0 0}, q_2^{0 0}\right]$	$[1200, 5600]$
		$\left[P_{11}^{0 0}, P_{22}^{0 0}\right]$	$[1000, 1100]$

Figures 7(a) and (b) show the distribution of the Root Mean Square (RMS) error in logarithm scales for each constant, which were generated from the estimations by the stochastic linear characterization method after the acquisition of 3400 measurements. The RMS error is by definition written as:

$$e_{\text{RMS}}(q_i^{k|k}) = \sqrt{\frac{\sum_{j=1}^k (q_i^{k|k} - q_i^*)^2}{k}}, \forall i = \{1, 2\}. \quad (4.19)$$

It is first shown that the RMS error is within 700 even when the variances of measurement noises are at the maximum. The superiority of this result can be verified when Figure 8 is shown, which is the result of the same test using the conventional deterministic approach. The maximum RMS

error of the conventional approach amounts over 43000, which is 60 times more than that of the proposed framework. The RMS error by the proposed framework ranges within 630 whereas the range of the RMS error the conventional approach exceeded 43000. The ability of the proposed framework in removing the effect of noise can also be verified by the results.

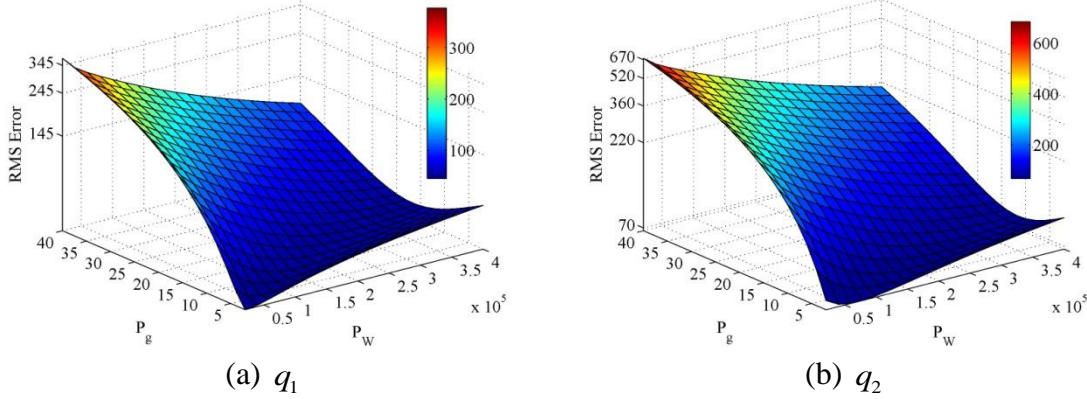


Figure 7 RMS distribution at different noise amplitudes by the characterization method.

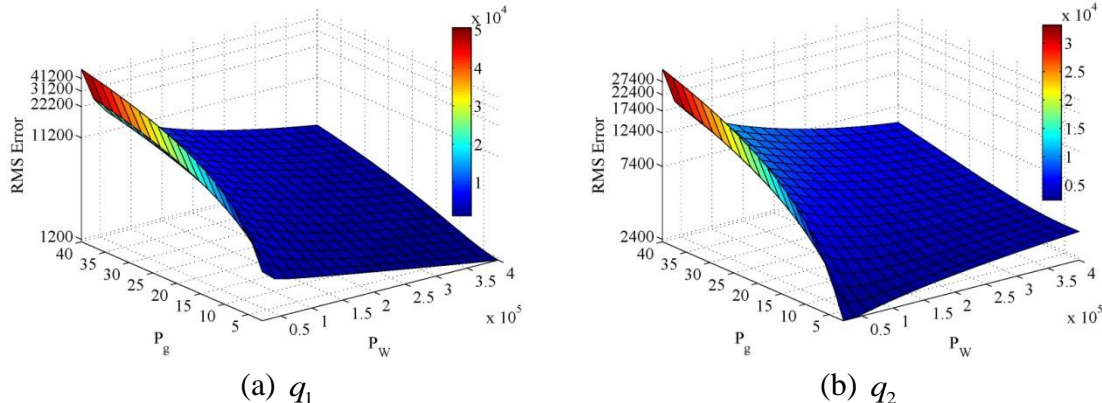


Figure 8 RMS distribution with different noise amplitudes by the conventional deterministic approach.

4.4.1.2 Estimation at Different Prior Knowledge

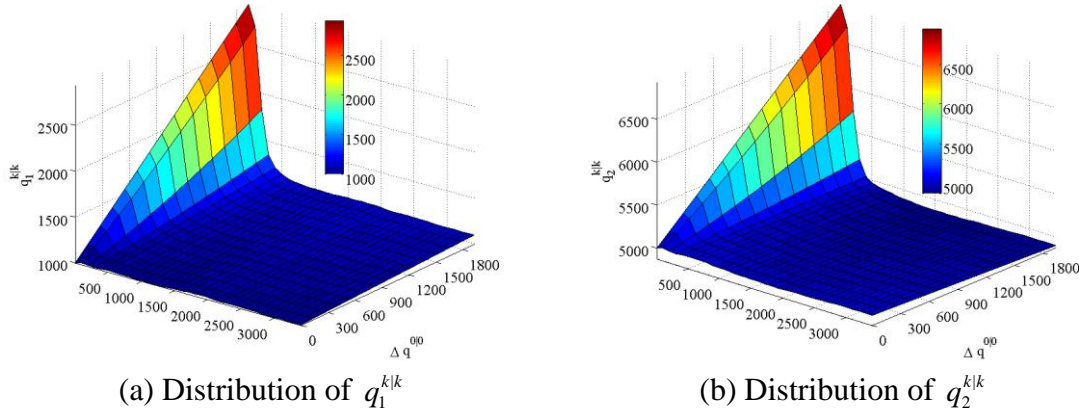
The ability of the proposed framework for estimation at different prior knowledge was investigated with two parametric studies. Table 4 lists the parameters of the first study where the prior knowledge on the mean $\mathbf{q}^{0|0}$ was varied while the prior knowledge on the covariance $\mathbf{P}^{0|0}$ was fixed. The prior means were proportionally varied by the same amount. Note that the increment,

or the gap between the prior mean and the true value, rather than the prior mean itself has been selected as one axis because the performance of the characterization method varies only with respect to the gap.

Table 4 Parameters for tests investigating prior means ($\Delta q^{0|0} \in [0, 2000]$).

Parameter for Measurement	Value	Parameter for Proposed Framework	Value
$\left[\left(P_g^* \right)_1, \left(P_g^* \right)_2 \right]$	$[20, 20]$	$\left[\left(P_g \right)_1, \left(P_g \right)_2 \right]$	$[20, 20]$
P_w^*	20000	P_w^*	20000
		$\left[q_1^{0 0}, q_2^{0 0} \right]$	$\left[q_1^* + \Delta q^{0 0}, q_2^* + \Delta q^{0 0} \right]$
		$\left[P_{11}^{0 0}, P_{22}^{0 0} \right]$	$[1000, 1100]$

Figures 9(a) and (b) show the distribution of each estimated constant $q_i^{k|k}$, $\forall i \in \{1, 2\}$, with different gaps and at different numbers of measurements. The figures first depict that the estimated constants converge to the exact solution no matter what the gap is. The figures also show that estimated constants quickly approach to the exact solution even if the gap is large. These observations indicate that the performance of the characterization method is not largely affected by the prior knowledge on the mean value. Figures 9(c) and (d) show the distribution of each variance $P_{ii}^{k|k}$. It is shown in the figures that the variances quickly reduce towards zero or that the estimated values quickly become certain irrespective of the gap. Figure 9 on the whole indicates that the performance of estimation by the proposed framework still depends on the number of measurements acquired but is consistent regardless of the prior knowledge on the mean value.



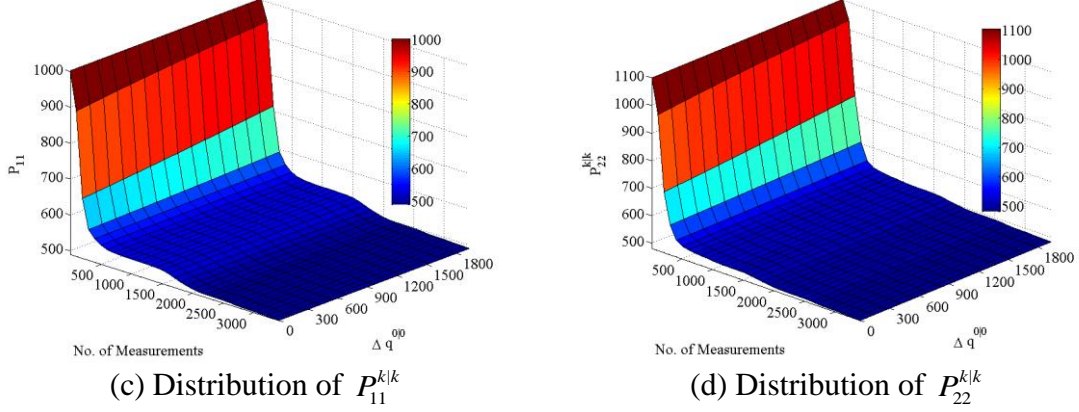


Figure 9 Distribution of mean and variance computed with different prior means.

Table 5 lists the parameters of the second study where the prior knowledge on the covariance $\mathbf{P}^{0|0}$ was varied with the prior knowledge on the mean $\mathbf{q}^{0|0}$ fixed. The prior variances were again varied proportionally by the same amount. Figures 10(a) and (b) show the distribution of each estimated constant with different prior variances and at different numbers of measurements, whilst Figures 10(c) and (d) show the distribution of each variance. There are more fluctuations when the prior variances are large, but the estimated constants exhibit convergence to the exact solution no matter what the prior variances are. The variances reduce fast particularly with a large prior variance and become nearly zero after 2000 measurements regardless of the prior variance. The results, together with the parametric study on the prior mean, indicate that the characterization method consistently makes a good estimate with high certainty regardless of the prior knowledge on both the mean and covariance.

Table 5 Parameters for tests investigating prior variances ($\Delta P^{0|0} \in [0, 2000]$).

Parameter for Measurement	Value	Parameter for Proposed Framework	Value
$\left[\left(P_g^* \right)_1, \left(P_g^* \right)_2 \right]$	[20,20]	$\left[\left(P_g \right)_1, \left(P_g \right)_2 \right]$	[20,20]
P_w^*	20000	P_w^*	20000
		$\left[q_1^{0 0}, q_2^{0 0} \right]$	[1200,5600]
		$\left[P_{11}^{0 0}, P_{22}^{0 0} \right]$	$\left[1000 + \Delta P^{0 0}, 1100 + \Delta P^{0 0} \right]$

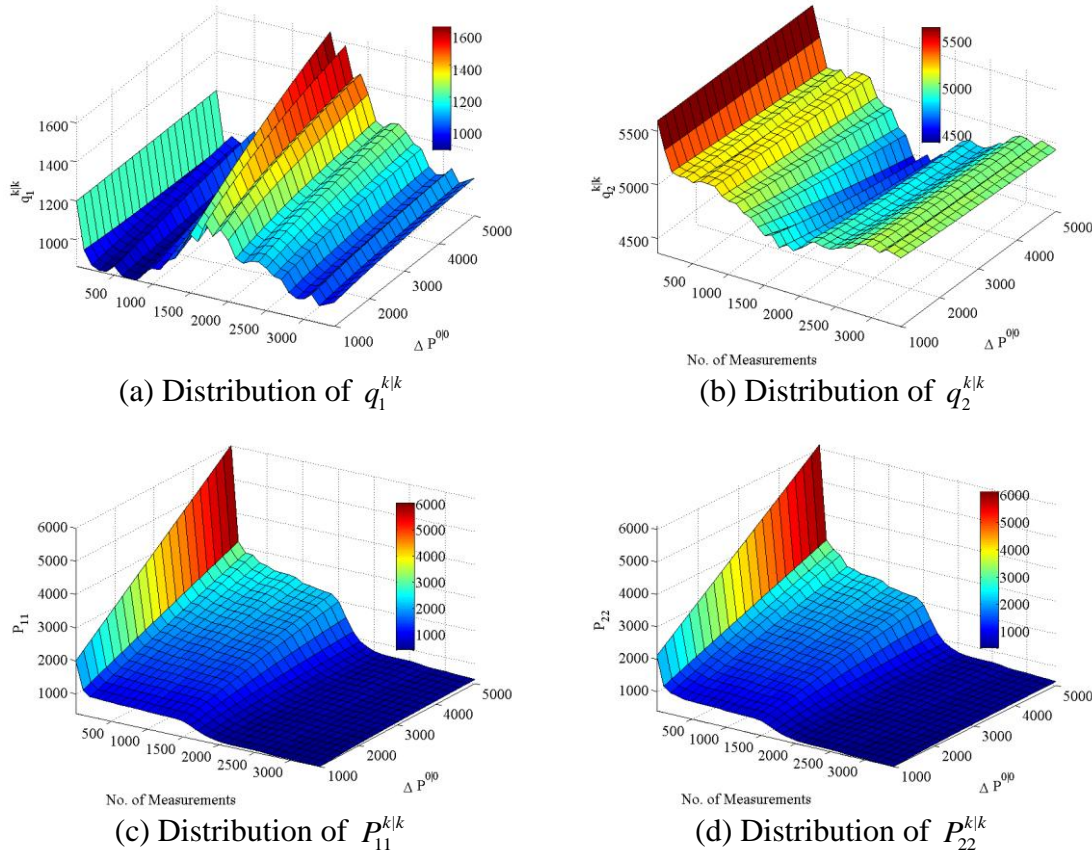


Figure 10 Distribution of mean and variance computed with different prior variances.

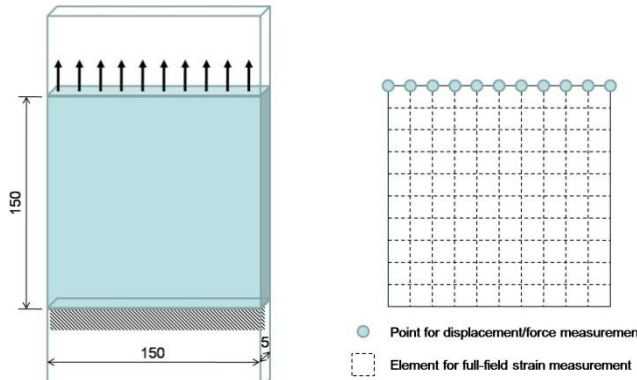
4.4.2 Identification of Elastic Constants

In the identification of elastic constants, the specimen used consisted of a typical laminate composed of AS4/3506-1 lamina with a balanced $\pm 30^\circ$ stacking sequence. The anisotropic material has been reported to have the elastic constants listed in Table 6. Figure 11(a) shows the geometry of the specimen as well as the loading conditions. The ungripped part of the specimen, used for identification, was of square shape with dimensions of 150mm \times 150mm \times 5mm. A tensile test was performed where the upper surface was pulled vertically while the bottom surface was fixed both vertically and horizontally. Material tests were performed in a simulated environment. Figure 11(b) shows the points of boundary displacement/force measurements as well as elements of strain measurement. The boundary displacement/force measurements were created by specifying the loading conditions and adding artificial noises whereas the strain measurements were created

by performing the two-dimensional finite element analysis with the loading conditions and adding artificial noises. As shown in the figure, 11 boundary points and 100 strain elements were measured. The rest of parameters used to create measurements and the parameters used by the characterization method are listed in Table 7.

Table 6 Material properties of AS4/3506-1 specimen.

Property	Value
q_{11}^*	1.36×10^5 MPa
q_{22}^*	1.11×10^4 MPa
q_{66}^*	5.80×10^3 MPa
q_{12}^*	3.34×10^3 MPa
θ	30°



(a) Specimen and loading (b) Measurements

Figure 11 Experimental setup.

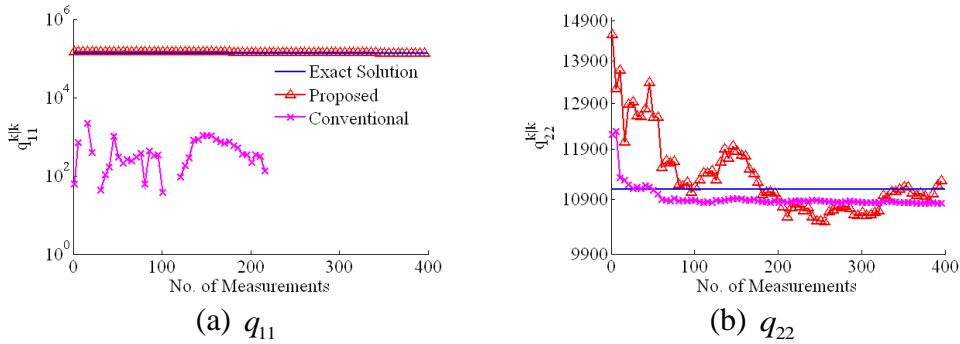
Table 7 Parameters for the identification of elastic constants ($\forall i \in \{1, \dots, 4\}$).

Parameter for Measurement	Value	Parameter for Proposed Framework	Value
$(P_g^*)_i$	1.00×10^{-4}	$(P_g)_i$	1.00×10^{-4}
P_w^*	2.00×10^2	P_w^*	2.00×10^2
		$\mathbf{q}^{0 0}$	$[1.50 \times 10^5, 1.50 \times 10^4, 5.00 \times 10^3, 1.00 \times 10^4]^\top$ MPa
		$P_{11}^{0 0}$	5.10×10^6
		$P_{22}^{0 0}$	1.05×10^7
		$P_{33}^{0 0}$	1.50×10^7

$$P_{44}^{00}$$

$$3.01 \times 10^8$$

Figures 12 and 13 show the transitions of the elastic constants identified and the variances computed by the characterization method, respectively. Figure 12 also shows the result of the conventional approach for comparison. Although the identification of elastic constants scaled up the problem to four-dimensional space, the characterization method identified adequate elastic constants after taking 200 measurements. The estimation by the characterization method at every acquisition of measurements is very fast, and the recursive estimation does not increase the computation time with respect to the number of measurements. The identification after 200 measurements thus indicates the practical feasibility of the characterization method. It is also shown that the constants identified by the conventional approach are considerably deviated from the exact solution and do not even improve by the acquisition of more measurements. The fluctuation of means was attributed to the random error introduced in the measurement uncertainties. Figure 13 additionally shows the ability of the characterization method in exhibiting the certainty of estimation in terms of variances and the increase of certainty with the acquisition of measurements. The decrease and convergence of the variances toward zero also indicate that the identification of elastic constants is being converging. Table 8 quantitatively compares the characterization method and the conventional approach in terms of the identified constants after 400 measurements. The results indicate the maximum error of the characterization method is within 4% and it is improved from the conventional approach by two orders.



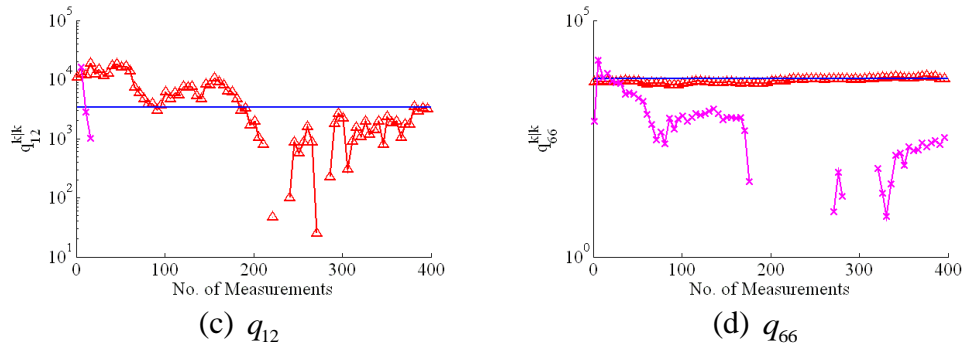


Figure 12 Elastic constants identified.

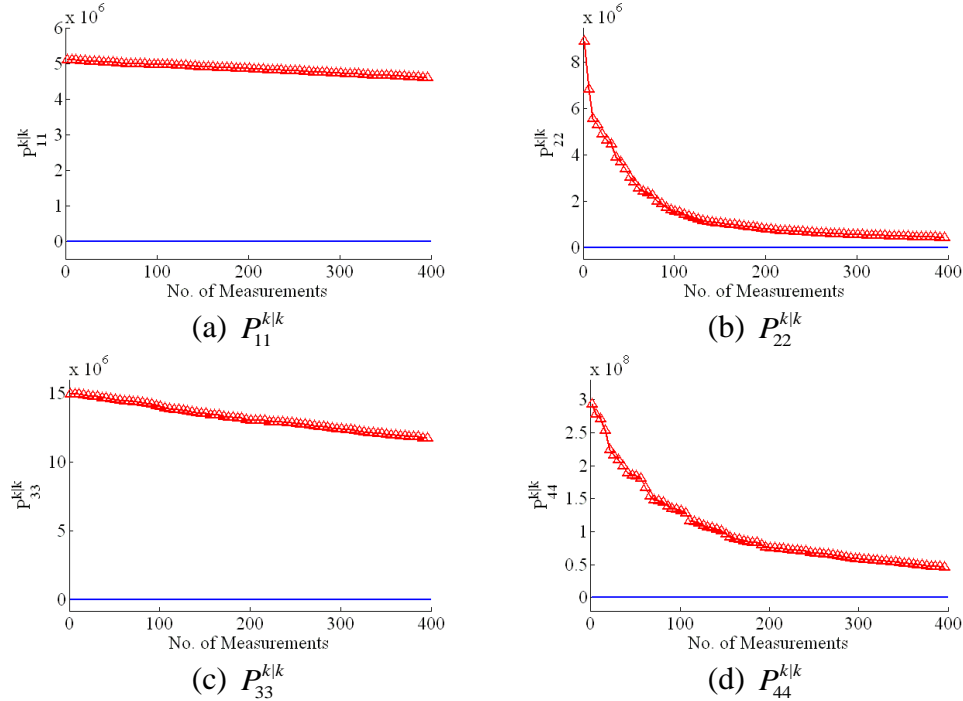


Figure 13 Variances computed.

Table 8 Elastic constants identified after 400 measurements.

Elastic Constant	Identified Value		Error	
	Proposed (MPa)	Deterministic (MPa)	Proposed (%)	Deterministic (%)
q_{11}	1.35×10^5	1.34×10^2	0.47	90.16
q_{22}	1.12×10^4	1.08×10^4	1.51	2.34
q_{66}	5.93×10^3	3.40×10^2	2.32	94.15
q_{12}	3.23×10^3	1.02×10^3	3.11	69.37

4.5 Summary

A method which stochastically identifies the elastic constants of anisotropic materials to remove the effect of noise significant in the energy-based characterization has been proposed. The stochastic linear characterization method recursively estimates the constants at the acquisition of every set of measurements using KF. Due to the nonlinear expression of the measurement model, a Kalman gain that achieves optimal estimation has been further derived. Since the variances in addition to the means are computed, the characterization method can not only identify the elastic constants, but also quantify their certainty through the computed covariance as an additional advantage.

The validity of the characterization method was first investigated via three parametric studies with low-dimensional algebraic problems resembling the elastic identification problem. The first study, showing the transition of identification by the characterization method and its comparison to the conventional deterministic approach, demonstrates the efficacy and the superiority of the characterization method in terms of the accuracy of identification and the provision of certainty. In the second study of the noise effect, the characterization method was found to identify appropriately regardless of the noise amplitude and exceed the deterministic approach by 60 times in terms of accuracy. The third study of the prior knowledge influence indicates that the characterization method also makes a good estimate consistently irrespective of the prior knowledge. The characterization method was finally applied to the identification of elastic constants of a composite specimen consisting of AS4/3506-1 laminae with a balanced $\pm 30^\circ$ stacking sequence.

The results in this Chapter show successful identification of four elastic constants and have demonstrated the applicability of the method to the linear characterization of anisotropic materials. The characterization method is the basis of the proposed framework to perform linear characterization of anisotropic materials. The accuracy and performance of the characterization method are improved in the following chapter, where a multi-camera data fusion technique is presented to improve the measurements certainty.

Chapter 5

Multi-camera Data Fusion for Probabilistic Full-field Measurements

This Chapter presents a multi-camera data fusion technique that contributes robust probabilistic full-field measurements for the stochastic linear characterization method. When a specimen is deformed at a loading step, the data fusion technique formulates Gaussian probability density functions (PDF) of the centroids that are derived from the dots marked on the specimen. This is followed by the product of these Gaussian PDFs from multiple cameras, to compute the fused mean and covariance of centroids. The physical uncertainties, underlying in the full-field measurements, are then probabilistically modeled by propagating the computed covariance through the measurement models that are formulated in the previous Chapter. The data fusion technique further minimizes the covariance of full-field measurements, and subsequently improves the certainty of characterization results effectively.

This Chapter is organized as follows. In Section 5.1, probabilistic representations of the centroids are first presented. This section also includes the probabilistic formulations of fusing the centroids from multiple images. Section 5.2 covers the Gaussian probabilistic modeling of full-field measurements, which are derived by propagating the fused covariance through the measurement models. Following this, Section 5.3 presents the numerical implementation of the data fusion technique to the stochastic linear characterization method. Section 5.4 details the numerical examples that are carried out to demonstrate the potential of the data fusion technique. This

section is concluded with its application to determining the elastic constants of an anisotropic material.

5.1 Product of Gaussian Distributions

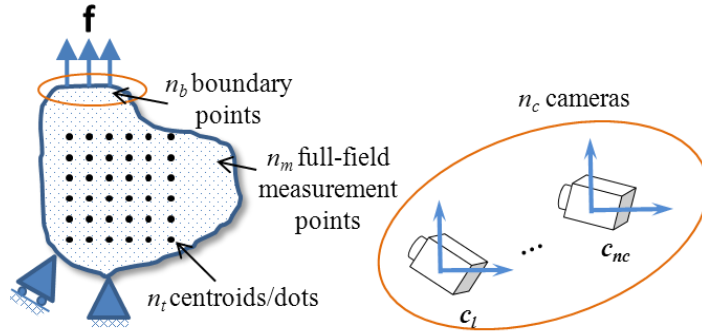


Figure 14 Schematic diagram of the multi-camera data fusion setup.

Figure 14 shows a schematic diagram of the multi-camera data fusion setup. The multi-camera data fusion technique uses a group of n_c cameras, labeled as $\{c_1, \dots, c_{n_c}\}$, to estimate the fused dot locations before deriving the probabilistic full-field measurements. Centroids of these dots are identified in different pixel coordinate systems from these cameras images. Homography transformation, previously presented in Section 3.2.1, is utilized to transform these centroids to a global coordinate system. This is demonstrated by first formulating the j^{th} centroid of the I_l^{th} camera image as

$${}^{I_l}(\mathbf{z}_x)_j^k \equiv [{}^{I_l}(z_x)_j^k, {}^{I_l}(z_y)_j^k]^\top = {}^{I_l}\mathbf{x}_j^k + {}^{I_l}(\mathbf{v}_x)_j^k, \quad (5.1)$$

where ${}^{I_l}(\cdot)$ represents the quantity (\cdot) that is derived from the I_l^{th} image from the c_l^{th} camera, $(\cdot)_j$ is the quantity (\cdot) corresponding to the j^{th} centroid, ${}^{I_l}(\mathbf{v}_x)_j^k \sim \mathbf{N}(\mathbf{0}, {}^{I_l}(\mathbf{P}_x)_j^k)$ follows a zero-mean normal distribution that has a covariance ${}^{I_l}(\mathbf{P}_x)_j^k$ given by the camera manufacturer's calibration data. The homography transforms ${}^{I_l}(\mathbf{z}_x)_j^k$ to a global coordinate system $\{c_l\}$ by a transformation matrix $\{{}_{I_l}^{c_l}\mathbf{H}$, i.e.,

$$\begin{aligned} {}^{c_l}(\mathbf{z}_x)_j^k &\equiv [{}^{c_l}(z_x)_j^k, {}^{c_l}(z_y)_j^k]^\top = \{{}_{I_l}^{c_l}\mathbf{H}\} {}^{I_l}(\mathbf{z}_x)_j^k \\ &= \{{}_{I_l}^{c_l}\mathbf{H}\} {}^{I_l}\mathbf{x}_j^k + \{{}_{I_l}^{c_l}\mathbf{H}\} {}^{I_l}(\mathbf{v}_x)_j^k \\ &\approx \mathbf{x}_j^k + {}^{c_l}(\mathbf{v}_x)_j^k \end{aligned} \quad (5.2)$$

For simplicity, it is assumed that $\{c_l\}_{\{I_l\}} \mathbf{H}$ yields the exact transformation from $I_l \mathbf{x}_j^k$ to \mathbf{x}_j^k and the measurement noise through the transformation $c_l (\mathbf{v}_x)_j^k$ still remains as white Gaussian:

$$c_l (\mathbf{v}_x)_j^k \sim \mathbf{N}(\mathbf{0}, c_l (\mathbf{P}_x)_j^k) \quad (5.3)$$

with the covariance $c_l (\mathbf{P}_x)_j^k$ that is attributed to the location of the c_l^{th} camera $\mathbf{x}_{c_l}^k$ in the global coordinate system. The observation probability density function (PDF) of the j^{th} dot is defined by a Gaussian distribution as

$$c_l p(\mathbf{x}_j^k | \mathbf{x}_{c_l}^k) \sim N(c_l (\mathbf{z}_x)_j^k, c_l (\mathbf{P}_x)_j^k). \quad (5.4)$$

Since the correlation of the Gaussian PDFs constructed in all n_c cameras is the true \mathbf{x}_j^k , the product of all PDFs becomes a total Gaussian PDF on \mathbf{x}_j^k based on all camera states \mathbf{x}_c^k :

$$\begin{aligned} {}^d p(\mathbf{x}_j^k | \mathbf{x}_c^k) &= \kappa \prod_{l=1}^{n_c} {}^{c_l} p(\mathbf{x}_j^k | \mathbf{x}_{c_l}) \\ &= \kappa \prod_{l=1}^{n_c} \left| 2\pi c_l (\mathbf{P}_x)_j^k \right|^{-\frac{1}{2}} \exp \left\{ -\frac{1}{2} \left[\mathbf{x}_j^k - {}^{c_l} (\mathbf{z}_x)_j^k \right]^T \left[{}^{c_l} (\mathbf{P}_x)_j^k \right]^{-1} \left[\mathbf{x}_j^k - {}^{c_l} (\mathbf{z}_x)_j^k \right] \right\}, \end{aligned} \quad (5.5)$$

where κ is the normalizing constant, and ${}^d(\cdot)$ denotes the data fusion results of (\cdot) . Based on Equation (5.4) of all n_c cameras, the data fusion technique derives the total Gaussian PDF of the j^{th} centroid as

$$\begin{aligned} {}^d p(\mathbf{x}_j^k | \mathbf{x}_c^k) &\propto \exp \left\{ -\frac{1}{2} \sum_{l=1}^{n_c} \left[\mathbf{x}_j^k - {}^{c_l} (\mathbf{z}_x)_j^k \right]^T \left[{}^{c_l} (\mathbf{P}_x)_j^k \right]^{-1} \left[\mathbf{x}_j^k - {}^{c_l} (\mathbf{z}_x)_j^k \right] \right\} \\ &\sim N \left\langle \left\{ \sum_{l=1}^{n_c} \left[{}^{c_l} (\mathbf{P}_x)_j^k \right]^{-1} \right\}^{-1} \left\{ \sum_{l=1}^{n_c} \left[{}^{c_l} (\mathbf{P}_x)_j^k \right]^{-1} {}^{c_l} (\mathbf{z}_x)_j^k \right\}^{-1}, \left\{ \sum_{l=1}^{n_c} \left[{}^{c_l} (\mathbf{P}_x)_j^k \right]^{-1} \right\}^{-1} \right\rangle. \end{aligned} \quad (5.6)$$

As a result of unequal uncertainties in each camera, the data fusion technique computes the fused mean ${}^d (\mathbf{z}_x)_j^k$ of Equation (5.6), weighted by the covariance of each camera $c_l (\mathbf{P}_x)_j^k$, as

$${}^d (\mathbf{z}_x)_j^k \equiv \left[{}^d (z_x)_j^k, {}^d (z_y)_j^k \right]^T = \left\{ \sum_{l=1}^{n_c} \left[{}^{c_l} (\mathbf{P}_x)_j^k \right]^{-1} \right\}^{-1} \left\{ \sum_{l=1}^{n_c} \left[{}^{c_l} (\mathbf{P}_x)_j^k \right]^{-1} {}^{c_l} (\mathbf{z}_x)_j^k \right\}, \quad (5.7)$$

and the fused covariance ${}^d (\mathbf{P}_x)_j^k$ that describes the certainty of the centroid is computed by

$${}^d(\mathbf{P}_x)_j^k \equiv \text{diag} \left[{}^d(P_x)_j^k, {}^d(P_y)_j^k \right] = \left\{ \sum_{l=1}^{n_c} \left[{}^{c_l}(\mathbf{P}_x)_j^k \right]^{-1} \right\}^{-1}. \quad (5.8)$$

Substitution of Equation (5.8) into (5.7) simplifies the fused mean of the j^{th} centroid to

$${}^d(\mathbf{z}_x)_j^k = {}^d(\mathbf{P}_x)_j^k \left\{ \sum_{l=1}^{n_c} \left[{}^{c_l}(\mathbf{P}_x)_j^k \right]^{-1} {}^{c_l}(\mathbf{z}_x)_j^k \right\} \quad (5.9)$$

5.2 Propagation of Uncertainties

The probabilistic representation of the fused full-field displacement of the n_m created points is derived by propagating the computed fused mean and covariance, from Equations (5.9) and (5.8), through the measurement models presented in the stochastic linear characterization method. Substitution of the fused mean of centroids to Equations (3.37) and (3.38) yields the full-field displacements of all n_m created points as

$$\mathbf{z}_{u_i}^k \equiv \left[\left(z_{u_i} \right)_1^k, \dots, \left(z_{u_i} \right)_{n_m}^k \right]^{\top} = \mathbf{N}_x^{k\top} \left\{ {}^d \mathbf{z}_i^k - {}^d \mathbf{z}_i^1 \right\} = \mathbf{N}_x^{k\top d} \mathbf{z}_{u_i}^k, \forall i \in \{x, y\}, \quad (5.10)$$

where $(\cdot)_{u_i}$ indicates whether the measured (\cdot) is corresponding to u_x or u_y , and the shape function \mathbf{N}_x^k , the fused location \mathbf{z}_i^k , and the fused displacement $\mathbf{z}_{u_i}^k$ are arranged by the n_t number of centroids and the n_m number of created full-field measurement points as:

$$\mathbf{N}_x^k \equiv \begin{bmatrix} N_{11}^k & \dots & N_{1n_m}^k \\ \vdots & \ddots & \vdots \\ N_{n_t 1}^k & \dots & N_{n_t n_m}^k \end{bmatrix}, \quad {}^d \mathbf{z}_i^k \equiv [{}^d(z_i)_1^k, \dots, {}^d(z_i)_{n_t}^k]^{\top} \text{ and } {}^d \mathbf{z}_{u_i}^k \equiv [{}^d(z_{u_i})_1^k, \dots, {}^d(z_{u_i})_{n_t}^k]^{\top}.$$

The computed fused covariance of the j^{th} dot ${}^d(\mathbf{P}_x)_j^k$ introduces the uncertainties of full-field displacement calculated at all n_m points. This is because each fused centroid ${}^d(\mathbf{z}_x)_j^k$ contains uncertainties which propagate through the combination of its fused data in Equation (5.10). The covariance of full-field displacement of all n_m points is thus adapted from the propagation of uncertainties as

$$\mathbf{P}_{u_i}^k \equiv \text{diag}[(P_{u_i})_1^k, \dots, (P_{u_i})_{n_m}^k] = \mathbf{N}_x^{k\top d} \mathbf{P}_i^k \mathbf{N}_x^k, \forall i \in \{x, y\}, \quad (5.11)$$

where the displacement covariance of all n_t centroids are defined by

$${}^d \mathbf{P}_i^k \equiv \text{diag} \left[{}^d (P_i)_1^k, \dots, {}^d (P_i)_{n_t}^k \right]^\top.$$

Similarly, the means of the full-field strain, $\mathbf{Z}_\varepsilon^k \equiv [\mathbf{z}_{\varepsilon_x}^k, \mathbf{z}_{\varepsilon_y}^k, \mathbf{z}_{\varepsilon_s}^k]^\top$, are derived by the shape functions, $\mathbf{N}_{\varepsilon_i}^k \equiv \frac{\partial \mathbf{N}_x^k}{\partial i}, \forall i \in \{x, y\}$, $\mathbf{N}_{\varepsilon_s}^k \equiv \frac{1}{2} [\mathbf{N}_{\varepsilon_x}^{k\top}, \mathbf{N}_{\varepsilon_y}^{k\top}]^\top$, and the fused means of the full-field displacement, ${}^d \mathbf{z}_u^k \equiv \left[\left({}^d \mathbf{z}_{u_x}^k \right)^\top, \left({}^d \mathbf{z}_{u_y}^k \right)^\top \right]^\top$, as

$$\begin{cases} \mathbf{z}_{\varepsilon_i}^k \equiv [(z_{\varepsilon_i})_1^k, \dots, (z_{\varepsilon_i})_{n_m}^k]^\top = \mathbf{N}_{\varepsilon_i}^{k\top} {}^d \mathbf{z}_{u_i}^k, \forall i \in \{x, y\} \\ \mathbf{z}_{\varepsilon_s}^k \equiv [(z_{\varepsilon_s})_1^k, \dots, (z_{\varepsilon_s})_{n_m}^k]^\top = \mathbf{N}_{\varepsilon_s}^{k\top} {}^d \mathbf{z}_u^k \end{cases}. \quad (5.12)$$

The covariance of full-field strain measurements, $\mathbf{P}_\varepsilon^k \equiv [\mathbf{P}_{\varepsilon_x}^k, \mathbf{P}_{\varepsilon_y}^k, \mathbf{P}_{\varepsilon_s}^k]$, is derived by the propagation of uncertainties as

$$\begin{cases} \mathbf{P}_{\varepsilon_i}^k \equiv \text{diag}[(P_{\varepsilon_i})_1^k, \dots, (P_{\varepsilon_i})_{n_m}^k] = \mathbf{N}_{\varepsilon_i}^{k\top} {}^d \mathbf{P}_u^k \mathbf{N}_{\varepsilon_i}^k, \forall i \in \{x, y\} \\ \mathbf{P}_{\varepsilon_s}^k \equiv \text{diag}[(P_{\varepsilon_s})_1^k, \dots, (P_{\varepsilon_s})_{n_m}^k]^\top = \mathbf{N}_{\varepsilon_s}^{k\top} {}^d \mathbf{P}_u^k \mathbf{N}_{\varepsilon_s}^k \end{cases}, \quad (5.13)$$

where the covariance of the fused dot locations of all n_t centroids is defined by ${}^d \mathbf{P}_u^k \equiv \text{diag}[{}^d (P_{u_x})_1^k, \dots, {}^d (P_{u_x})_{n_t}^k, {}^d (P_{u_y})_1^k, \dots, {}^d (P_{u_y})_{n_t}^k]$.

Substitution of Equation (5.12) over $\boldsymbol{\varepsilon}^k$ in Equation (3.31) yields the term $\mathbf{z}_g^k \equiv [z_{g_1}^k, \dots, z_{g_4}^k]^\top$ as

$$\mathbf{z}_g^k = \mathbf{g}(\Delta \mathbf{z}_\varepsilon^k; \theta). \quad (5.14)$$

It is also shown that the uncertainties in \mathbf{z}_ε^k propagate through a nonlinear function \mathbf{g} in Equation (3.31). As a result of the propagation, the nonlinear function is linearized by approximating it to a first-order Taylor series expansion, such that the propagation of \mathbf{P}_ε^k to the covariance of the term \mathbf{z}_g^k , $\mathbf{P}_g^k \equiv \text{diag}[P_{g_1}^k, \dots, P_{g_4}^k]^\top$, approximately follows the linear cases presented in Equations (5.11) and (5.13). The covariance is computed by

$$P_{g_f}^k = \left[(\mathbf{g}')_f^k \right]^\top \mathbf{p}_\varepsilon^k, \forall f \in \{1, \dots, 4\}, \quad (5.15)$$

where the term $(\mathbf{g}')_f^k$ is derived as

$$\begin{aligned}
(\mathbf{g}')_s^k = & \left\{ \left[\frac{\partial g_f(\Delta(\mathbf{z}_\varepsilon)_1^k; \theta)}{\partial \epsilon_x} \right]^2, \dots, \left[\frac{\partial g_f(\Delta(\mathbf{z}_\varepsilon)_{n_m}^k; \theta)}{\partial \epsilon_x} \right]^2, \right. \\
& \left[\frac{\partial g_f(\Delta(\mathbf{z}_\varepsilon)_1^k; \theta)}{\partial \epsilon_y} \right]^2, \dots, \left[\frac{\partial g_f(\Delta(\mathbf{z}_\varepsilon)_{n_m}^k; \theta)}{\partial \epsilon_y} \right]^2, \\
& \left. \left[\frac{\partial g_f(\Delta(\mathbf{z}_\varepsilon)_1^k; \theta)}{\partial \epsilon_s} \right]^2, \dots, \left[\frac{\partial g_f(\Delta(\mathbf{z}_\varepsilon)_{n_m}^k; \theta)}{\partial \epsilon_s} \right]^2 \right\}^\top,
\end{aligned} \tag{5.16}$$

and the vector \mathbf{p}_ε^k is defined by the covariance terms of the probabilistic full-field strain measurements as follows:

$$\mathbf{p}_\varepsilon^k \equiv \left[(\mathbf{P}_{\varepsilon_x})_1^k, \dots, (\mathbf{P}_{\varepsilon_x})_{n_m}^k, (\mathbf{P}_{\varepsilon_y})_1^k, \dots, (\mathbf{P}_{\varepsilon_y})_{n_m}^k, (\mathbf{P}_{\varepsilon_s})_1^k, \dots, (\mathbf{P}_{\varepsilon_s})_{n_m}^k \right]^\top. \tag{5.17}$$

In order to obtain the external work, the boundary displacement $(\mathbf{z}_u)_b^k$ is derived from Equation (5.10) as

$$(\mathbf{z}_{u_i})_b^k \equiv \left[(z_{u_i})_{b_1}^k, \dots, (z_{u_i})_{b_{n_b}}^k \right]^\top = \mathbf{N}_b^{k \top d} \mathbf{z}_{u_i}^k, \forall i \in \{x, y\}, \tag{5.18}$$

where the shape function \mathbf{N}_b^k , created over the n_t number of centroids ${}^d \mathbf{z}_x^k$ and n_b number of boundary points \mathbf{x}_b^k , is defined as

$$\mathbf{N}_b^k = \begin{bmatrix} N_{1b_1}^k & \dots & N_{n_t b_{n_b}}^k \\ \vdots & \ddots & \vdots \\ N_{1b_1}^k & \dots & N_{n_t b_{n_b}}^k \end{bmatrix} \tag{5.19}$$

Similarly, the fused covariance of the boundary displacement $(\mathbf{P}_{u_i})_b^k$ is thus derived by

$$(\mathbf{P}_{u_i})_b^k = \mathbf{N}_b^{k \top d} \mathbf{P}_{u_i}^k \mathbf{N}_b^k, \forall i \in \{x, y\}. \tag{5.20}$$

5.3 Numerical Implementation

Figure 15 shows the schematic diagram of the data fusion technique implemented to improve the certainty of measurements, where the solid line represents the flow of mean and dashed line is the flow of covariance. Given time step k , n_c number of cameras are used to measure centroids of the specimen from material testing. Each camera takes an image and identifies the j th centroid ${}^{c_j}(\mathbf{z}_x)^k_j$ and then fused the states to compute the fused mean ${}^d(\mathbf{z}_x)^k_j$ and covariance ${}^d(\mathbf{P}_x)^k_j$, using Equations (5.9) and (5.8). After collecting ${}^d(\mathbf{z}_x)^k_j$ and ${}^d(\mathbf{P}_x)^k_j$ of each j centroid into ${}^d\mathbf{z}_x^k$ and ${}^d\mathbf{P}_x^k$, the fused mean of the full-field displacement ${}^d\mathbf{z}_u^k$ and its covariance ${}^d\mathbf{P}_u^k$ are derived with the shape function \mathbf{N}_x^k . Both ${}^d\mathbf{z}_u^k$ and ${}^d\mathbf{P}_u^k$ are used for calculating the mean and covariance of the full-field strain, i.e., \mathbf{z}_e^k and \mathbf{P}_e^k . In addition, the boundary displacement mean $(\mathbf{z}_u)_b^k$ and covariance $(\mathbf{P}_u)_b^k$ are derived by ${}^d\mathbf{z}_u^k$ and ${}^d\mathbf{P}_u^k$ through the shape function \mathbf{N}_b^k .

This figure also illustrates the original contribution of the data fusion technique. The mean and covariance are fused based on the covariance in each camera sensor. The propagation of uncertainties yields the probabilistic full-field measurements in terms of mean and covariance, which contribute to the empirical knowledge of the stochastic linear characterization method.

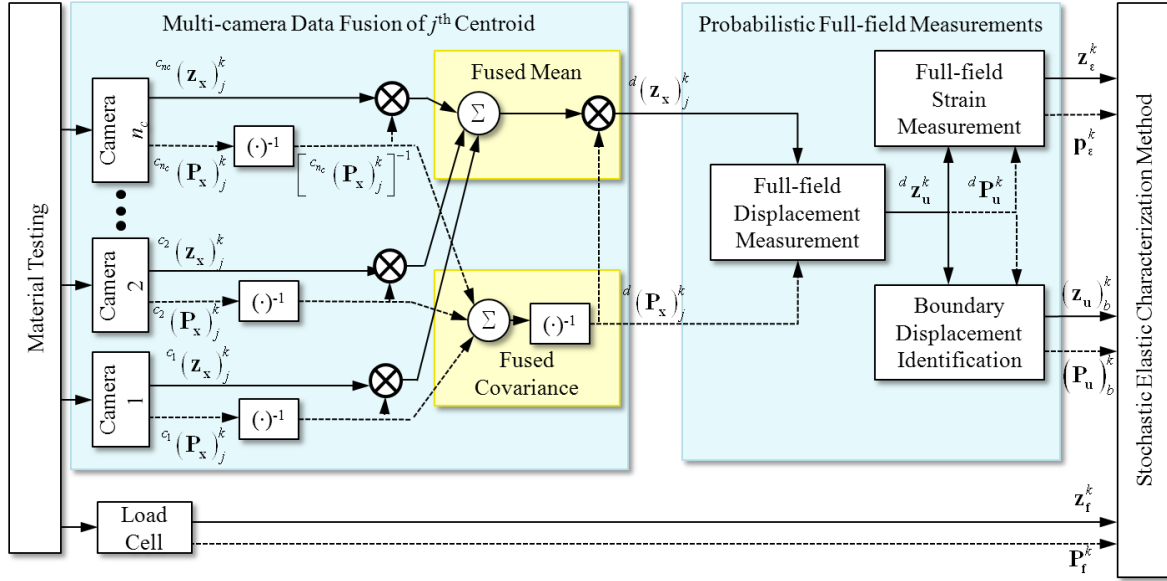


Figure 15 Numerical implementation of the data fusion technique.

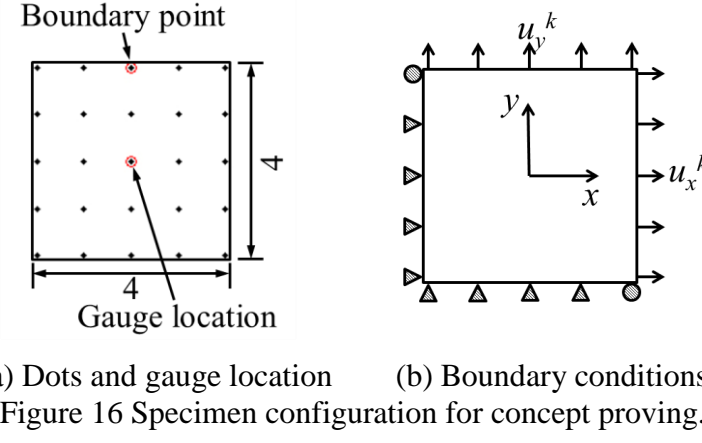
5.4 Numerical Studies

This section investigates the effectiveness of the multi-camera data fusion technique in two steps. The first step is aimed at the concept proving of the data fusion technique where three parametric studies are carried out by solving a simple analysis on an isotropic material, resembling the multi-camera full-field measurement problem. In the second and final step, the applicability of the data fusion technique to the stochastic linear characterization of an anisotropic material is examined.

5.4.1 Concept Proving of Full-field Measurements

The data fusion problem defined for Test 1-3 attempts to estimate the probabilistic full-field measurements by using cameras that contain different uncertainties. The problem made in this section is a simple analysis on an isotropic material with Young's modulus $E = 70\text{GPa}$ and Poisson's ratio $\nu_{12} = 0.3$ based on the results generated by a finite element analysis. Figure 16 shows the specimen configuration for proving the proposed technique. The specimen is of a square shape that is dimensioned at a 4-unit length on each side, as shown in Figure 16(a). The mesh configuration in the finite element analysis allows us to measure the deformation of 25 dots on

the specimen. Two dots are chosen to represent the boundary point and the gauge location for comparing the results. Figure 16(b) shows the boundary conditions of the specimen where displacement u_x^k and u_y^k are applied on two sides of the specimen to simulate equal displacement on both sides. The rest of the parameters used in the analysis are listed in Table 1.



(a) Dots and gauge location (b) Boundary conditions
Figure 16 Specimen configuration for concept proving.

Table 9 Parameters commonly used to create measurements in Tests 1-3.

Parameter	Value
Total no. of measurements	30
Displacement in x , u_x^k	$u_x^{k-1} + \Delta u$
Displacement in y , u_y^k	$u_y^{k-1} + \Delta u$
Incremental displacement, Δu	0.03

5.4.1.1 Estimation of Full-field Measurements (Test 1)

The uncertainties of cameras at each time step k were attributed by the covariance listed in Table 10. Each camera has a different covariance in the sensor properties, where camera 1, 2 and 3 had the most, moderate and least accurate information on the centroids, respectively.

Table 10 Covariance of every j^{th} centroid observed by camera $c_l, \forall l \in \{1, 2, 3\}$, in Test 1.

Parameter	Value
$c_1 (\mathbf{P}_x)_j^k$	$\text{diag}[4.00, 4.00] \times 10^{-4}$
$c_2 (\mathbf{P}_x)_j^k$	$\text{diag}[6.00, 6.00] \times 10^{-4}$
$c_3 (\mathbf{P}_x)_j^k$	$\text{diag}[8.00, 8.00] \times 10^{-4}$

Figures 17(a) and (b) compare the full-field displacements derived by each camera and the data fusion results in terms of error percentage. Despite that each camera observed an error at the magnitude of over 5% throughout the whole deformation, the data fusion technique converges within 1% of the exact solution after 4 measurements are collected. The derivation of full-field strain by each camera and the data fusion technique are compared in Figures 18(a)-(c). The unfused full-field strains by each camera are shown more uncertain than the measurement derived by the proposed technique. Both the strains in the transverse and longitudinal directions in Figures 18(a) and (b) show error of over 10% whereas the proposed technique oversees a 2% accuracy within the exact solution that was achieved only after 4 measurements. The comparison of shear strains in Figure 18(c) shows that each camera achieved error of over 20%. The data fusion technique, however, improved the shear strain by estimating within 10% of the exact solution after 6 measurements. Table 11 compares the mean error of the full-field measurements derived by each camera and the data fusion technique. As expected, the mean error increased from camera 1 to 3 due to the difference of accuracy in each camera. The proposed technique estimated the measurements more accurately with a mean error percentage of 1% despite the covariance in each camera.

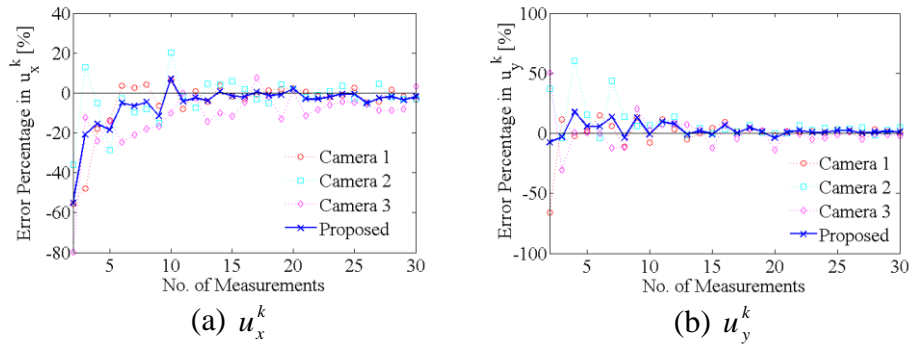
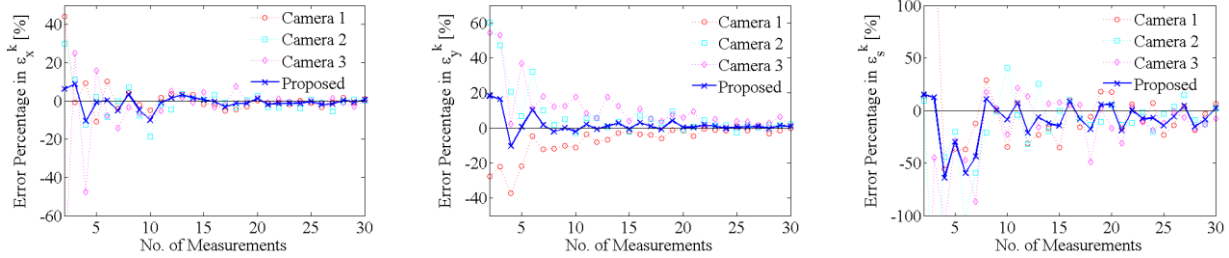


Figure 17 Comparison of full-field displacement measurements at the gauge location.



(a) ε_x^k (b) ε_y^k (c) ε_s^k

Figure 18 Comparison of full-field strain measurements at the gauge location (Test 1).

Table 11 Mean error percentage of the fused measurements (Test 1).

Measurement	Mean Absolute Error Percentage [%]			
	Camera 1	Camera 2	Camera 3	Proposed
u_x	7.26	7.13	12.30	6.49
u_y	6.68	9.22	7.58	4.19
ε_x	4.53	4.84	9.44	2.63
ε_y	7.35	8.62	11.57	2.98
ε_s	31.24	24.85	35.39	15.06

5.4.1.2 Parametric Study of Camera Uncertainties and Number of Cameras (Test 2)

After showing the capability of the data fusion technique over the results derived directly from each camera, the number of cameras with different uncertainties was investigated by applying the parameters listed in Table 12. The number of cameras tested varied from 1 unit to 50 units. The uncertainties in each number of cameras are attributed by a covariance, which was increased equally over the number of study. Figures 19(a) and (b) compare the error of the estimated centroid at the gauge location when the data derived from different number of cameras were fused by the data fusion technique. It is overall shown that the error decreases when the measurement covariance is lesser in each camera, and the error converges to 1% when more than 10 cameras that have measurement covariance of 0.05 are utilized. This concludes that the proposed technique can not only estimate the achievable accuracy by a number of cameras, but also determine the adequate number of cameras that can achieve any desired accuracy without introducing excessive number of cameras.

Table 12 Parameters for estimation using multiple cameras with different covariance,

$$\forall l \in \{1, \dots, 50\} \text{ (Test 2).}$$

Parameter	Value
n_c	l
${}^c \mathbf{P}_x$	$\text{diag}[l, l] \times 10^{-5}$

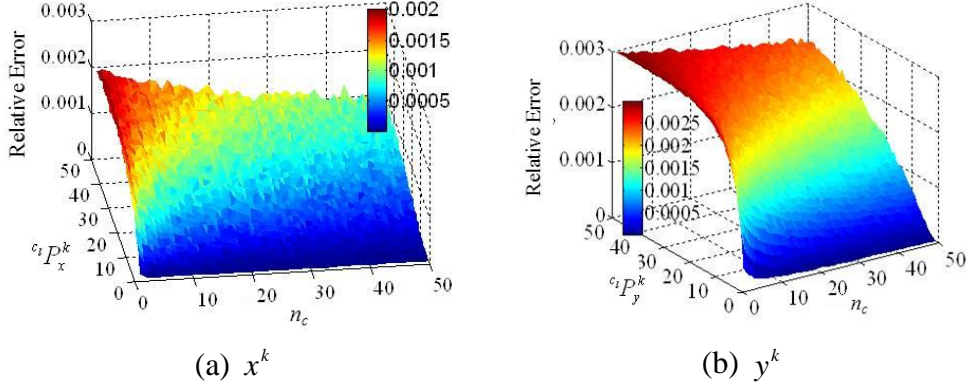


Figure 19 Error of gauge location from multiple cameras with different covariance,
 $\forall l \in \{1, \dots, 50\}$ (Test 2).

5.4.1.3 Error Propagation from Different Noise Parameters (Test 3)

In order to investigate the efficiency of error propagation of the data fusion technique, different covariance type of camera was used in 30 time steps. Table 13 lists the parameters for the case studies of the error propagation. Four cameras were used in all 3 cases where the uncertainty in measurements was increased from the first to the fourth camera. Case 1 resembles the problem where the covariance in each camera is constant throughout the time steps. The cameras in case 2 employ covariance that was linearly increased at each measurement, whereas case 3 simulates the problem where nonlinear covariance, in the form of sinusoidal wave, is observed in each camera. Figures 20(a) and (b) show the error of the estimated full-field displacement, whereas Figures 21(a)-(c) show the error of the full-field strain at the gauge location in all 3 cases. The data fusion technique estimated full-field displacements that were within 5% of the exact solution after 4 measurements. The estimated fused full-field strains achieved within 10% accuracy of the exact solution after 20 measurements. The full-field strains are shown to be noisy in case 3 before 10 measurements were achieved and the measurements in case 2 become noisier afterwards when the linearly increasing covariance surpassed the noise of case 3. As expected, the measurement in case 1 has the overall least noise since constant covariance was used. Overall, the data fusion technique estimated the fused full-field measurements adequately, despite the difference of the covariance type in each case.

Table 13 Parameters for the data fusion technique, $\forall l \in \{1, \dots, 4\}$, and $n_c = 4$ (Test 3).

Case	Parameter	Value
1	$c_l \tilde{\mathbf{P}}_x^k$	$\text{diag}[l, l] \times 10^{-4}$
2	$c_l \tilde{\mathbf{P}}_x^k$	$c_l \tilde{\mathbf{P}}_x^{k-1} + \text{diag}[l, l] \times 10^{-4}$
3	$c_l \tilde{\mathbf{P}}_x^k$	$l \text{diag}[\sin(k) + 1, \sin(k) + 1] \times 10^{-5}$

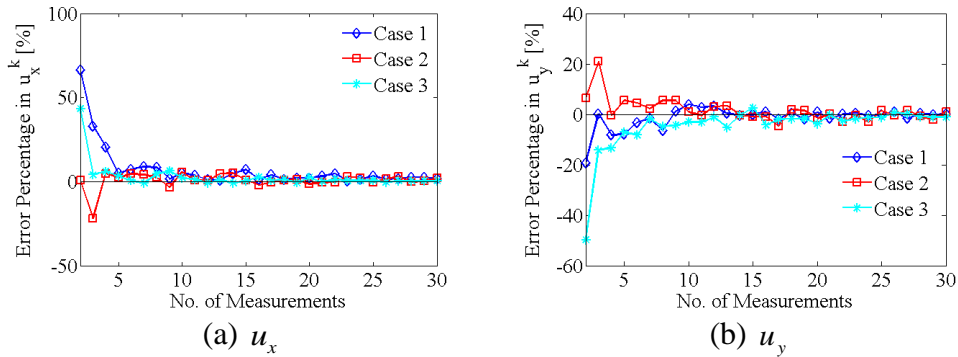


Figure 20 Case studies of the estimated means of fused full-field displacement measurements at the gauge location (Test 3).

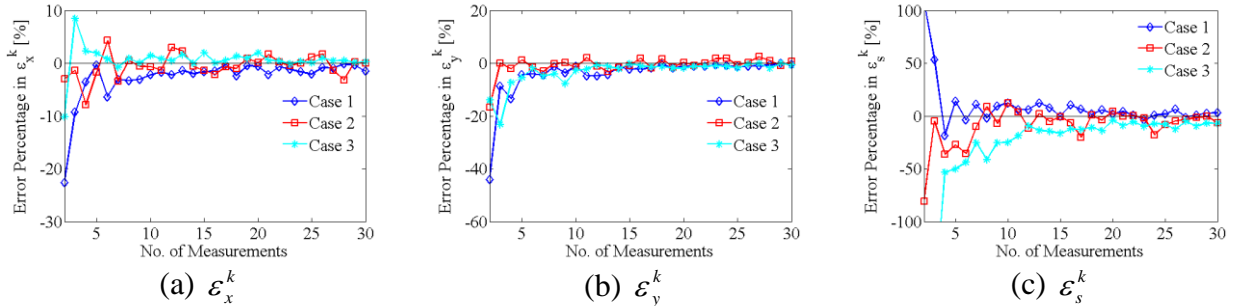


Figure 21 Case studies of the estimated means of fused full-field strain measurements at the gauge location (Test 3).

Figures 22, 23 and 24 show the propagated variances of the full-field measurements estimated by the proposed technique. Figure 22(a) shows the estimated variances of the fused full-field displacement propagated from the covariance of each camera. Figure 22(b) shows the variance of the boundary displacement at the boundary point propagated from the fused covariance of the centroids, whereas the variances propagated from the full-field displacement are shown in Figures 23(a) and (b). It is noted that the constant, linearly increasing and nonlinear trends of covariance from Table 13 remain the same despite the difference in magnitude. Figures 24(a)-(d)

show the covariance \mathbf{P}_g^k , propagated from the uncertainties in full-field strain measurements. It is, however, shown that \mathbf{P}_g^k increased exponentially due to its quadratic equations over the time steps, indicating new trends of covariance from the ones listed in Table 13. The transition of the propagated variance is estimated to construct a more appropriate Kalman gain, Equation (4.14), in the stochastic linear characterization method.

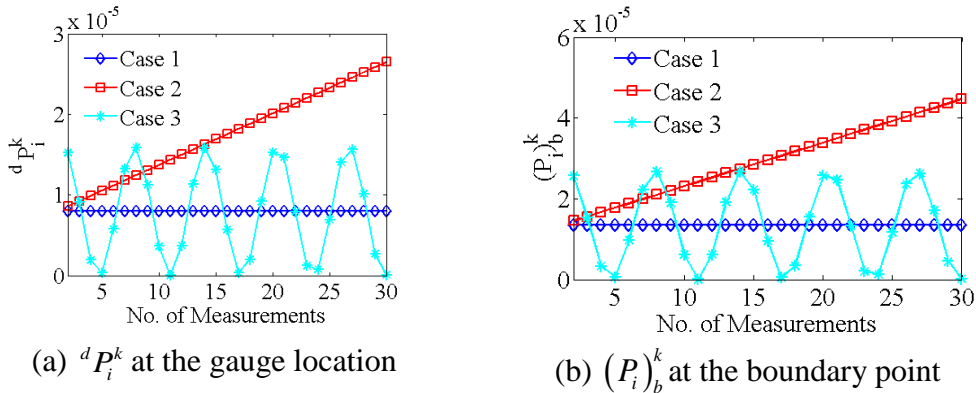


Figure 22 Propagated variance of displacement in all three cases, $\forall i \in \{x, y\}$ (Test 3).

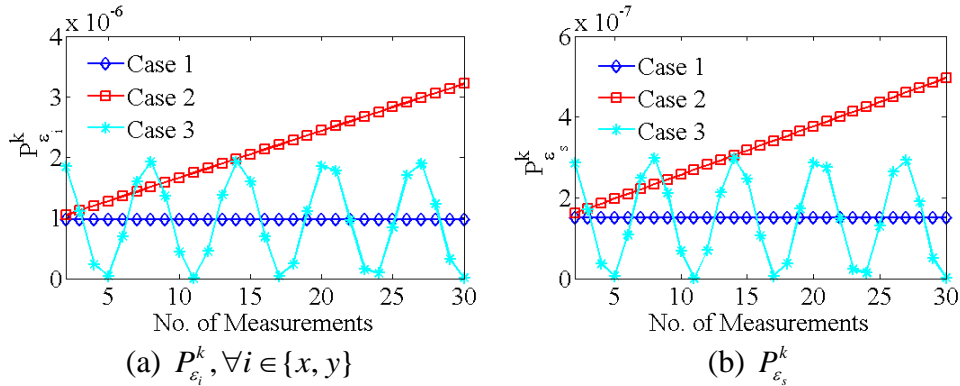
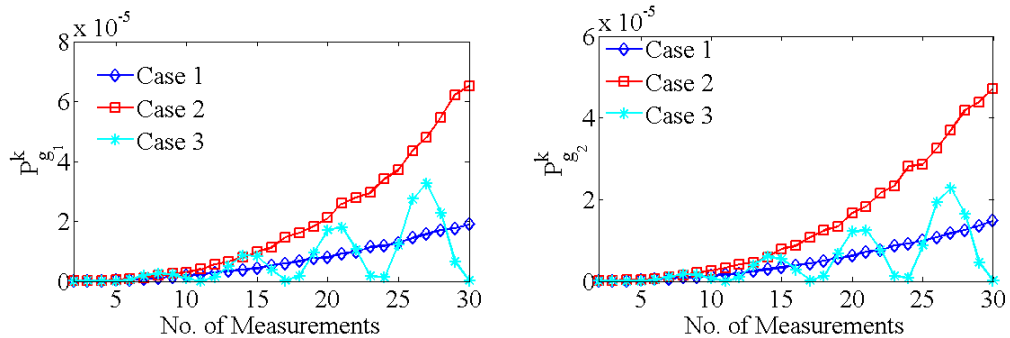


Figure 23 Propagated variance of full-field strain in all three cases (Test 3).



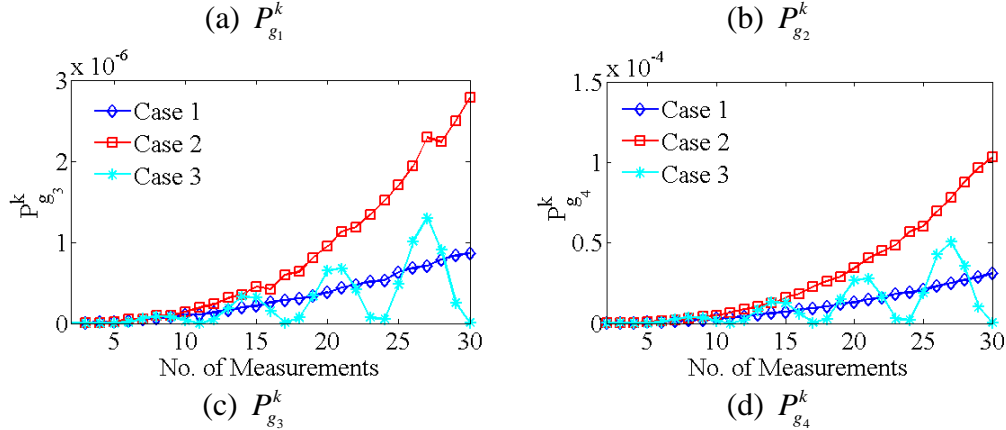


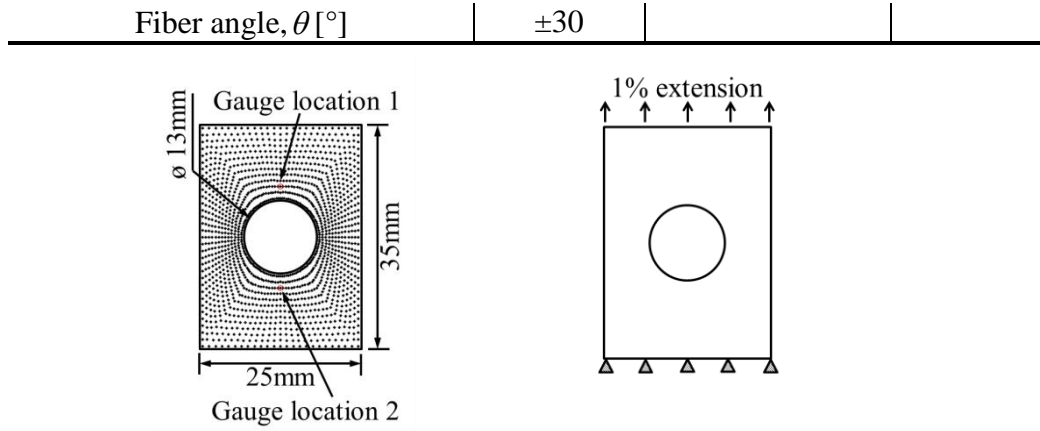
Figure 24 Propagated variance, $P_{g_i}^k, \forall i \in \{1, \dots, 4\}$, in all three cases (Test 3).

5.4.2 Application to the Characterization of Anisotropic Materials

Based on the efficacy investigated in the previous section, the data fusion technique is finally applied to the stochastic characterization of an anisotropic material. The chosen anisotropic material is the AS4D/9310 graphite/epoxy cross-ply laminate $[\pm 30]_T$ that has a thickness of 1.25mm in each lamina. The material parameters of the lamina are listed in Table 14. Figures 25(a) and (b) show the specimen configuration for the characterization of anisotropic material. Figure 25(a) shows not only the dots and the dimension of the specimen, but also the two gauge locations that were used to compare the fused measurements. As shown in the figure, 1456 dots were measured. The open-hole specimen was loaded with the boundary conditions that resembled a tensile test, as shown in Figure 25(b). The parameters for the estimation of elastic constants are listed in Table 15. The covariance of four cameras was used by the data fusion technique, whereas the prior knowledge on the mean $q_M^{0|0}$ and variances $\mathbf{P}^{0|0}$ were utilized by the stochastic characterization method.

Table 14 Material parameters of AS4D/9310 graphite/epoxy lamina.

Parameter	Value	Elastic Constant	Value
Longitudinal modulus, E_1 [MPa]	1.34×10^5	q_{11} [MPa]	1.35×10^5
Longitudinal modulus, E_2 [MPa]	7.71×10^3	q_{22} [MPa]	7.75×10^3
Shear modulus, G_6 [MPa]	4.31×10^3	q_{12} [MPa]	2.33×10^3
Poisson's ratio, ν_{12}	0.30	q_{66} [MPa]	4.31×10^3

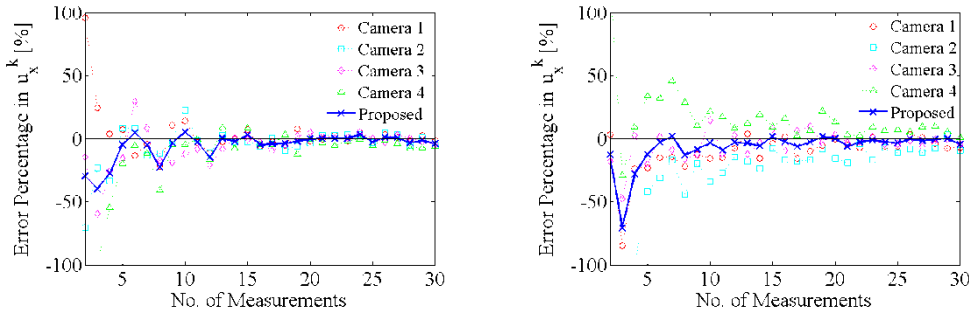


(a) Dots and gauge locations (b) Boundary conditions
Figure 25 Specimen configuration for the estimation of elastic constants.

Figures 26(a)-(d) show the transitions of the error of full-field displacements derived by each camera and the data fusion technique. As shown in the figures, the variations in the full-field displacements at both gauge locations are observed. The fused full-field displacements, however, converged to the exact solution after 4 measurements. The mean error 10% of the fused measurements is lower than the observed measurements, which has a 25% mean error percentage.

Table 15 Parameters for the estimation of elastic constants using $n_c = 4$ cameras.

Parameter For measurement	Value	Parameter for stochastic characterization	Value
$c_1 \mathbf{P}_x^k$	$\text{diag}[1.00, 1.00] \times 10^{-9}$	$\mathbf{q}_M^{00} [\text{MPa}]$	$[1.50, 0.05, 0.05, 0.05]^T \times 10^5$
$c_2 \mathbf{P}_x^k$	$\text{diag}[2.00, 2.00] \times 10^{-9}$	P_{11}^{00}	5.10×10^{13}
$c_3 \mathbf{P}_x^k$	$\text{diag}[3.00, 3.00] \times 10^{-9}$	P_{22}^{00}	5.00×10^{14}
$c_4 \mathbf{P}_x^k$	$\text{diag}[4.00, 4.00] \times 10^{-9}$	P_{33}^{00}	5.00×10^{14}
		P_{44}^{00}	4.00×10^{12}



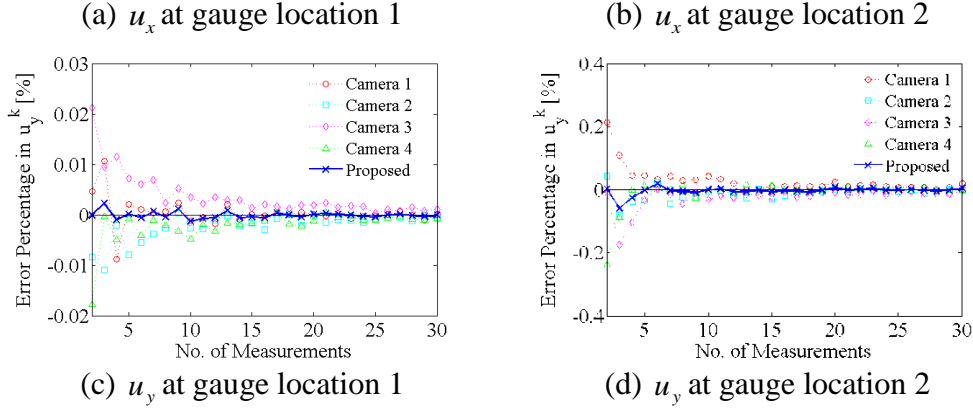
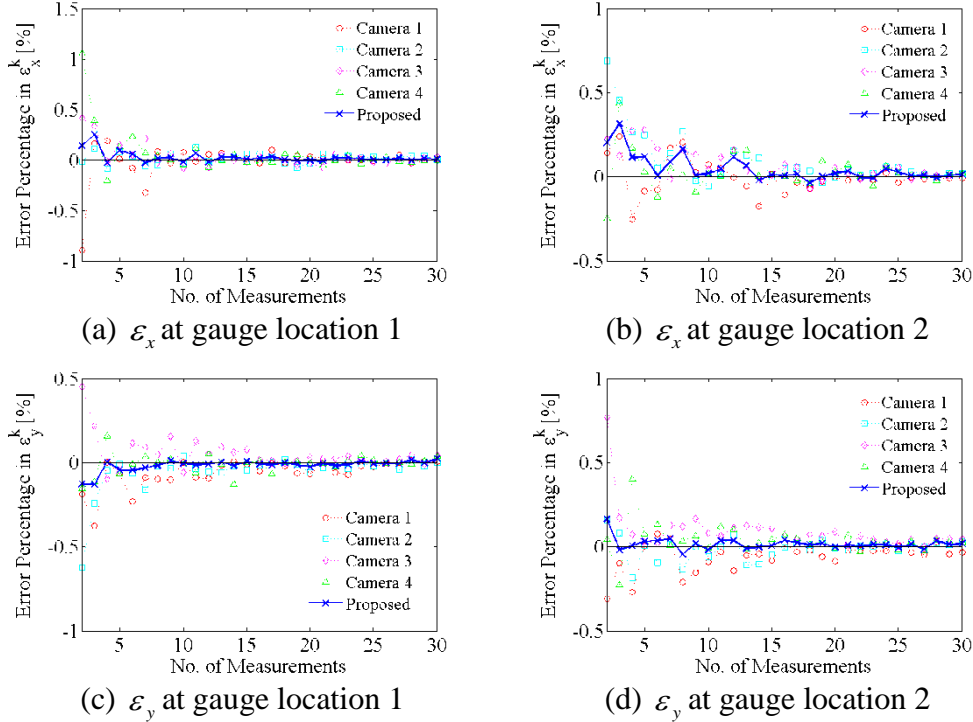


Figure 26 Comparison of measured full-field displacements at gauge locations.

Figures 27(a)-(f) show the transition of the strains at the gauge locations, estimated by the data fusion technique. The figures also show the strain results of each camera for comparison. As the specimen is deformed, the proposed technique weighted the covariance in each camera and estimated the full-field strains within 5% accuracy of the exact solution.



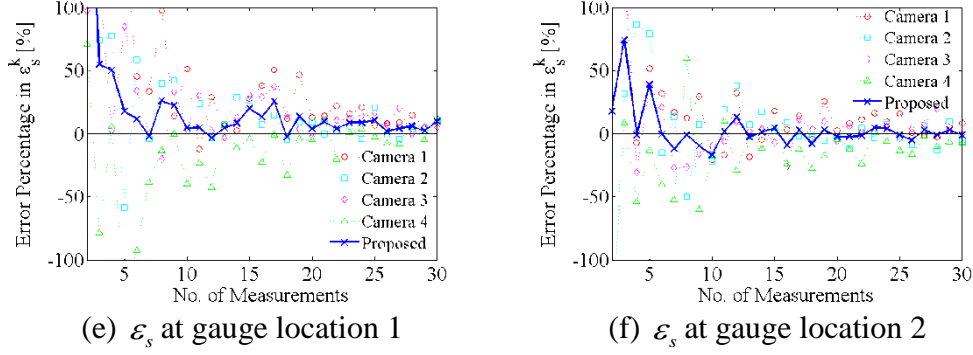
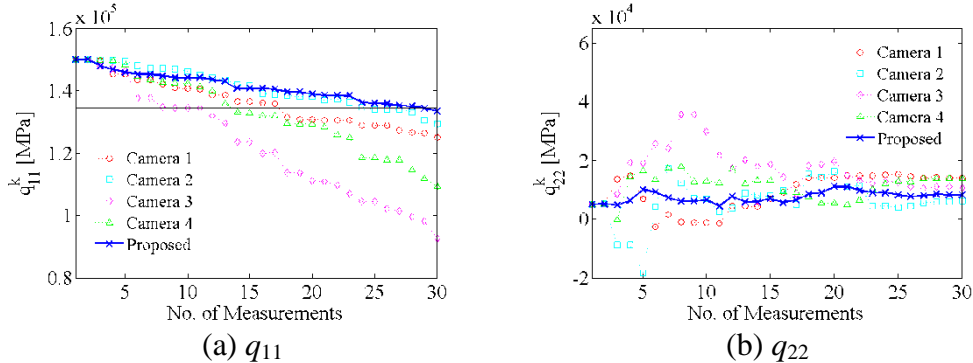


Figure 27 Comparison of measured full-field strains at gauge locations.

Figures 28 and 29 show the transition of the elastic constants identified and the variances computed by the stochastic linear characterization method using the measurements estimated by the proposed technique, respectively. Figure 28 also shows the derived elastic constants from each camera for comparison. The data fusion technique improves the measurements and resulted adequate identification of elastic constants after taking 30 measurements, whereas the constants identified by directly using the measurements from each camera did not converge to the exact solution. Figure 29 additionally exhibits the certainty of estimation in terms of variances of elastic constants. The decrease and convergence of the variances toward zero also indicate that the identification of elastic constants is being converging. Table 16 further compares the error of the elastic constants when using the measurements from the data fusion technique and each camera after 30 time steps. The comparison indicates the practical feasibility of the data fusion technique that improved the accuracy of the stochastic linear characterization method by at least two orders.



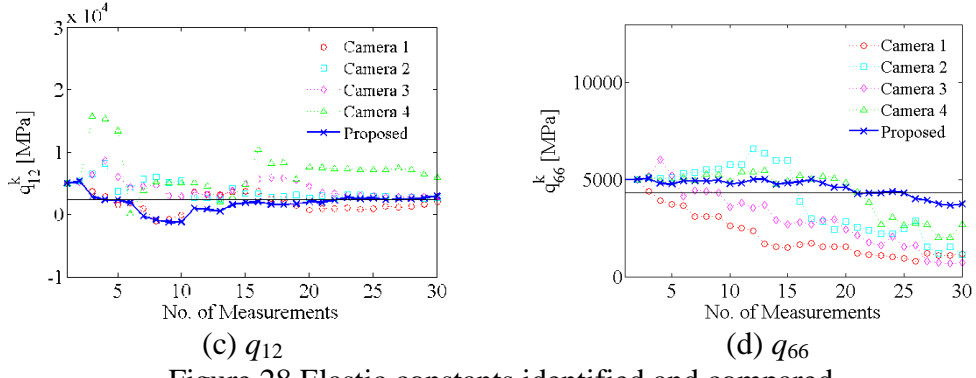


Figure 28 Elastic constants identified and compared.

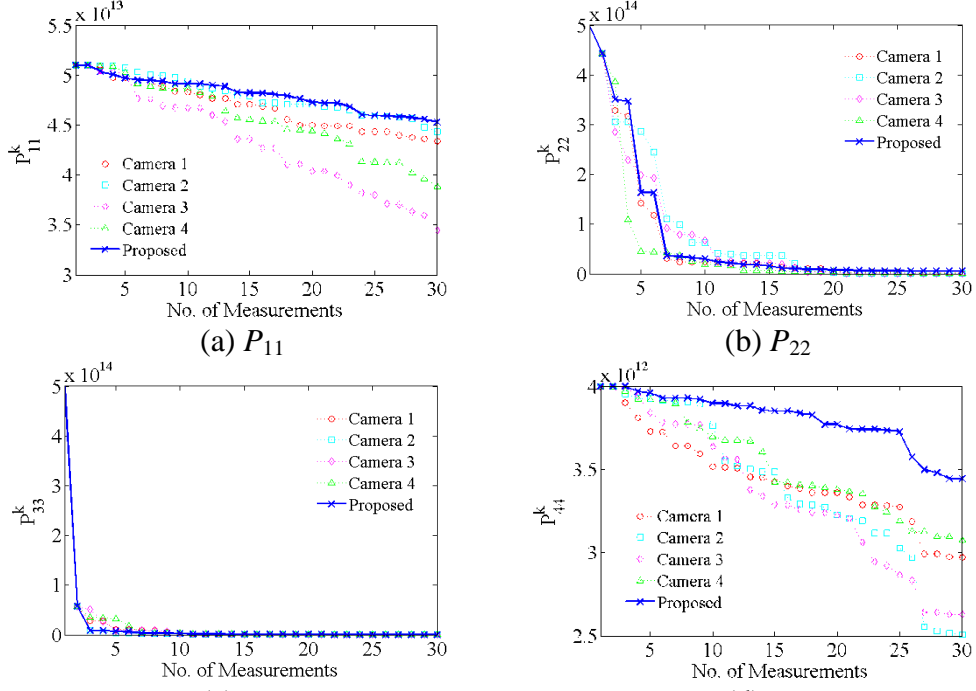


Figure 29 Variance computed and compared.

Table 16 Parameters for the estimation of elastic constants using $n_c = 4$ cameras.

Elastic Constant	Error Percentage [%]				
	Camera 1	Camera 2	Camera 3	Camera 4	Proposed
q_{11}	7.06	3.94	31.28	18.95	0.97
q_{22}	79.48	20.57	36.77	78.84	4.92
q_{12}	16.82	11.91	25.38	155.10	24.65
q_{66}	72.62	74.04	83.58	37.42	13.34

5.5 Summary

A data fusion technique, which fuses the information of dots marked on a test coupon from images taken by multiple cameras, has been presented to derive more reliable probabilistic full-field measurements for the proposed framework. For each camera at a specific loading step, the data fusion technique constructs a Gaussian PDF for each centroid of dots from a image. The product of these Gaussian PDFs over different cameras yields the fused mean and covariance of centroids. The fused covariance is further used to construct probabilistic measurement models through a propagation of uncertainties method.

Three numerical studies were performed on a specimen that was loaded equally on two free edges. The first study, showing the transition of the fused results and the comparisons with the unfused measurement of each camera, demonstrated 5 times accuracy improvement of the data fusion technique in measuring full-field strains. The second study demonstrated that the number of cameras converges to a certain value when a certain accuracy level is required, hence aiding the data fusion technique to improve the accuracy of measurements without excessive number of cameras. The third study indicated that the data fusion technique adequately propagate uncertainties from different model of measurement covariance, thus determining more reliable empirical knowledge for the stochastic characterization method to compute the Kalman gain. The data fusion technique was finally applied to the linear characterization of a graphite/epoxy laminate. The results show improvement of the stochastic characterization method by two orders and have demonstrated the potential of the data fusion technique in improving the measurements for more accurate characterization results.

The numerical studies in this Chapter demonstrate that the data fusion technique minimizes the effect of uncertainties in measurements, and provides probabilistic measurements to estimate more reliable characterization results. With the capability of the multi-camera data fusion technique demonstrated, the following Chapter commences with the development of stochastic multi-linear characterization method, which is derived based on the previously presented stochastic linear characterization method.

Chapter 6

Stochastic Multi-linear Characterization of Anisotropic Materials

This Chapter presents a stochastic multi-linear characterization method to approximate the nonlinear behavior of anisotropic materials. The nonlinear behavior of anisotropic materials is represented with a multi-linear model under the assumption that the material is path-, rate- and temperature independent. The modified Kalman filter presented in the stochastic linear characterization method is further generalized to include the characterization of coefficients of multi-linear partitions. Since the coefficients are estimated with their associated variance, differential entropy is also presented here as a single quantity that measures the certainty of all estimated coefficients. The validity of the characterization method in estimating the multi-linear coefficients is first demonstrated via a multi-linear finite element analysis. Parametric studies of the proposed framework under a range of measurement uncertainties are subsequently investigated.

This Chapter is organized as follows. Section 6.1 first shows a multi-linear framework that approximates the nonlinear behavior of anisotropic materials. Section 6.2 presents generalized stochastic equations of the modified Kalman filter to incorporate the characterization of multi-linear coefficients. The formulation of differential entropy is also presented in this section. Section 6.3 describes the numerical implementation of the modified Kalman filter for solving the multi-linear characterization problem. Following this, Section 6.4 demonstrates the validity of the characterization method through a series of numerical studies.

6.1 Nonlinear Energy-based Characterization Framework

6.1.1 Multi-linear Constitutive Model

The partitions in a multi-linear constitutive model are created to approximate the nonlinear behavior of anisotropic materials. To simplify the nonlinear behavior with the multi-linear representation, it is assumed that the materials are path-, rate- and temperature-independent. When a symmetric angle-ply laminate is deformed in a finite element analysis, each element experiences the behavior of a multi-linear partition.

Figure 30 shows the multi-linear partitions that are created based on the planar strains of an element e . n_A , n_B and n_C are defined as the total number of partition in the strain axis ε_1 , ε_2 and ε_6 , respectively. Each linear partition is described by a set of multi-linear coefficients. The elemental strain, exhibited along each material axis $\varepsilon_i, i \in \{1, 2, 6\}$, is partitioned by a strain incremental value $\Delta\varepsilon_i$, where $\Delta(\cdot)_i$ represents the incremental value of (\cdot) on the i^{th} material axis. A list of these parameters, which are used to define each multi-linear partition, is summarized in Table 17.

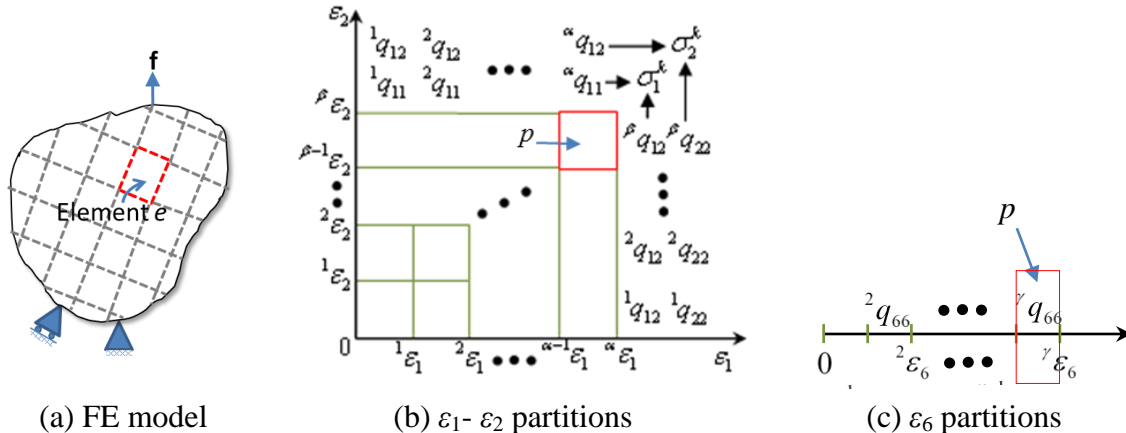


Figure 30 Schematic diagram of the multi-linear partitions on each material axis of an element e in a deforming elastic body.

Table 17 Use of parameters in defining a specific partition.

Strain Partition	Partition Range	Multi-linear Coefficients	Critical Strains
α	${}^\alpha\varepsilon_1 > \varepsilon_1 \geq {}^{\alpha-1}\varepsilon_1$	${}^\alpha q_{11}, {}^\alpha q_{12}$	${}^\alpha\varepsilon_1, {}^{\alpha-1}\varepsilon_1$
β	${}^\beta\varepsilon_2 > \varepsilon_2 \geq {}^{\beta-1}\varepsilon_2$	${}^\beta q_{12}, {}^\beta q_{22}$	${}^\beta\varepsilon_2, {}^{\beta-1}\varepsilon_2$
γ	${}^\gamma\varepsilon_6 > \varepsilon_6 \geq {}^{\gamma-1}\varepsilon_6$	${}^\gamma q_{66}$	${}^\gamma\varepsilon_6, {}^{\gamma-1}\varepsilon_6$

For a specific partition range on the strains $\varepsilon_1 - \varepsilon_2$, defined by ${}^\alpha\varepsilon_1 > \varepsilon_1 \geq {}^{\alpha-1}\varepsilon_1$, $\forall \alpha \in \{1, \dots, n_A\}$, and ${}^\beta\varepsilon_2 > \varepsilon_2 \geq {}^{\beta-1}\varepsilon_2$, $\forall \beta \in \{1, \dots, n_B\}$, the stress-strain relations of the σ_1 and σ_2 models are represented by

$$\begin{bmatrix} \sigma_1^k \\ \sigma_2^k \end{bmatrix} = \begin{bmatrix} {}^\alpha q_{11} & {}^\beta q_{12} \\ {}^\alpha q_{12} & {}^\beta q_{22} \end{bmatrix} \begin{bmatrix} \varepsilon_1^k \\ \varepsilon_2^k \end{bmatrix} + \mathbf{D}_{1-2}, \quad (6.1)$$

where the matrix \mathbf{D}_{1-2} is constant in the specified strain partition range of $\varepsilon_1 - \varepsilon_2$ defined by any previous multi-linear coefficients, i.e.:

$$\mathbf{D}_{1-2} = - \begin{bmatrix} {}^\alpha q_{11} & {}^\beta q_{12} \\ {}^\alpha q_{12} & {}^\beta q_{22} \end{bmatrix} \begin{bmatrix} {}^{\alpha-1}\varepsilon_1 \\ {}^{\beta-1}\varepsilon_2 \end{bmatrix} + \sum_{i_1=0}^{\alpha} \sum_{i_2=0}^{\beta} \begin{bmatrix} {}^{(\alpha-1)-i_1} q_{11} & {}^{(\beta-1)-i_2} q_{12} \\ {}^{(\alpha-1)-i_1} q_{12} & {}^{(\beta-1)-i_2} q_{22} \end{bmatrix} \begin{bmatrix} {}^{(\alpha-1)-i_1}\varepsilon_1 - {}^{(\alpha-2)-i_1}\varepsilon_1 \\ {}^{(\beta-1)-i_2}\varepsilon_2 - {}^{(\beta-2)-i_2}\varepsilon_2 \end{bmatrix} \quad (6.2)$$

with the condition such that ${}^h(\cdot) = 0$ if the term h is given by $h \leq 0$.

For a specific partition range on the strain ε_6 , defined by ${}^\gamma\varepsilon_6 > \varepsilon_6 \geq {}^{\gamma-1}\varepsilon_6$, $\forall \gamma \in \{1, \dots, n_C\}$, the stress-strain relation of the σ_6 model are derivable by

$$\sigma_6^k = {}^\gamma q_{66} \varepsilon_6^k + D_6, \quad (6.3)$$

where D_6 is a constant in the strain partition range of ε_6 denoted by

$$D_6 = -{}^\gamma q_{66} {}^{\gamma-1}\varepsilon_6 + \sum_{i_3=1}^{\gamma} {}^{\gamma-1}q_{66} {}^{(\gamma-1)-i_3} \varepsilon_6, \quad (6.4)$$

with the similar condition such that ${}^h(\cdot) = 0$ if the term h is given by $h \leq 0$.

In the same strain partition range, Equations (6.1) and (6.3) yield the stress-strain relations in their incremental forms as

$$\begin{bmatrix} \Delta\sigma_1^k \\ \Delta\sigma_2^k \\ \Delta\sigma_6^k \end{bmatrix} = \begin{bmatrix} \sigma_1^k - \sigma_1^{k-1} \\ \sigma_2^k - \sigma_2^{k-1} \\ \sigma_6^k - \sigma_6^{k-1} \end{bmatrix} = \begin{bmatrix} {}^\alpha q_{11} & {}^\beta q_{12} & 0 \\ {}^\alpha q_{12} & {}^\beta q_{22} & 0 \\ 0 & 0 & {}^\gamma q_{66} \end{bmatrix} \begin{bmatrix} \Delta\varepsilon_1^k \\ \Delta\varepsilon_2^k \\ \Delta\varepsilon_6^k \end{bmatrix}, \quad (6.5)$$

where the non-zero terms of the multi-linear coefficients that describe the behavior of the element e are denoted as

$${}_e^p \mathbf{q}_M \equiv \left[{}_e^\alpha q_{11}, {}_e^\beta q_{22}, {}_e^\alpha q_{12}, {}_e^\beta q_{12}, {}_e^\gamma q_{66} \right]^\top, \quad (6.6)$$

and ${}^p(\cdot)$ denotes the quantity (\cdot) that exhibits the multi-linear behavior in the corresponding linear partitions of p , ${}_e(\cdot)$ denotes the quantity (\cdot) of element e . Thus, ${}^p{}_e(\cdot)$ denotes the quantity (\cdot) of the partition p measured on an element e .

Given the incremental stress-strain relation of lamina in the material coordinate system, the relations between the stresses and strains of the symmetric angle-ply laminate with a fiber orientation of $\pm\theta$ can be approximated in the global coordinate system as

$$\mathbf{Q}(\theta; {}^p{}_e \mathbf{q}_M) = \begin{bmatrix} {}^{\alpha}{}_e q_{xx}(\theta; {}^p{}_e \mathbf{q}_M) & {}^{\beta}{}_e q_{xy}(\theta; {}^p{}_e \mathbf{q}_M) & {}^{\gamma}{}_e q_{xs}(\theta; {}^p{}_e \mathbf{q}_M) \\ {}^{\alpha}{}_e q_{xy}(\theta; {}^p{}_e \mathbf{q}_M) & {}^{\beta}{}_e q_{yy}(\theta; {}^p{}_e \mathbf{q}_M) & {}^{\gamma}{}_e q_{ys}(\theta; {}^p{}_e \mathbf{q}_M) \\ {}^{\alpha}{}_e q_{xs}(\theta; {}^p{}_e \mathbf{q}_M) & {}^{\beta}{}_e q_{ys}(\theta; {}^p{}_e \mathbf{q}_M) & {}^{\gamma}{}_e q_{ss}(\theta; {}^p{}_e \mathbf{q}_M) \end{bmatrix} = \mathbf{Q}({}^p{}_e \mathbf{q}) \quad (6.7)$$

with ${}^p{}_e \mathbf{q} \equiv \left[{}^{\alpha}{}_e q_{xx}, {}^{\beta}{}_e q_{yy}, {}^{\gamma}{}_e q_{ss}, {}^{\alpha}{}_e q_{xy}, {}^{\alpha}{}_e q_{yx}, {}^{\alpha}{}_e q_{xs}, {}^{\gamma}{}_e q_{ys}, {}^{\beta}{}_e q_{ys}, {}^{\gamma}{}_e q_{xy} \right]^T$.

Transformation of the constitutive model with respect to the fiber angle θ yields the constitutive model in the local coordinates as

$${}^p{}_e \mathbf{q} = \mathbf{H}(\theta) {}^p{}_e \mathbf{q}_M, \quad (6.8)$$

where the transformation matrix $\mathbf{H}(\theta)$ is derived as

$$\mathbf{H}(\theta) = \begin{bmatrix} \mathbf{h}_1(\theta)^T \\ \mathbf{h}_2(\theta)^T \\ \mathbf{h}_3(\theta)^T \\ \mathbf{h}_4(\theta)^T \\ \mathbf{h}_5(\theta)^T \\ \mathbf{h}_6(\theta)^T \\ \mathbf{h}_7(\theta)^T \\ \mathbf{h}_8(\theta)^T \\ \mathbf{h}_9(\theta)^T \end{bmatrix} = \begin{bmatrix} m^4 & m^2 n^2 & m^2 n^2 & m^2 n^2 & 4m^2 n^2 \\ n^4 & m^4 & m^2 n^2 & m^2 n^2 & 4m^2 n^2 \\ 2m^2 n^2 & 2m^2 n^2 & -2m^2 n^2 & -2m^2 n^2 & 2(m^2 - n^2)^2 \\ m^2 n^2 & m^2 n^2 & n^4 & m^4 & -4m^2 n^2 \\ m^2 n^2 & m^2 n^2 & m^4 & n^4 & -4m^2 n^2 \\ m^3 n & -mn^3 & mn^3 & -m^3 n & 2mn(n^2 - m^2) \\ 2m^3 n & -2mn^3 & -2m^3 n & 2mn^3 & 4mn(n^2 - m^2) \\ mn^3 & -m^3 n & m^3 n & -mn^3 & 2mn(m^2 - n^2) \\ 2mn^3 & -2m^3 n & -2mn^3 & 2m^3 n & 4mn(m^2 - n^2) \end{bmatrix}, \quad (6.9)$$

with $m = \cos \theta$ and $n = \sin \theta$. Similar to Equation (3.26), the incremental strain energy of the element e , ${}_e U_{\Delta}^k$, is described as

$${}_e U_{\Delta}^k = \frac{1}{2} \int_V \Delta_e \boldsymbol{\sigma}^{k\top} \Delta_e \boldsymbol{\varepsilon}^k dV = {}_e \mathbf{g}(\Delta_e \boldsymbol{\varepsilon}^k; \theta)^{\top} {}_e \mathbf{q}_M, \quad (6.10)$$

where

$$\begin{aligned} {}_e \mathbf{g}(\Delta_e \boldsymbol{\varepsilon}^k; \theta) &\equiv [{}_e g_1^k, {}_e g_2^k, {}_e g_3^k, {}_e g_4^k, {}_e g_5^k]^{\top} \\ &= \frac{t}{2} \left\{ \int_A (\Delta_e \varepsilon_x^k)^2 dA \mathbf{h}_1(\theta) + \int_A (\Delta_e \varepsilon_y^k)^2 dA \mathbf{h}_2(\theta) + \int_A (\Delta_e \varepsilon_s^k)^2 dA \mathbf{h}_3(\theta) \right. \\ &\quad + \int_A \Delta_e \varepsilon_x^k \Delta_e \varepsilon_y^k dA \mathbf{h}_4(\theta) + \int_A \Delta_e \varepsilon_x^k \Delta_e \varepsilon_s^k dA \mathbf{h}_5(\theta) + \int_A \Delta_e \varepsilon_y^k \Delta_e \varepsilon_s^k dA \mathbf{h}_6(\theta) \\ &\quad \left. + \int_A \Delta_e \varepsilon_x^k \Delta_e \varepsilon_s^k dA \mathbf{h}_7(\theta) + \int_A \Delta_e \varepsilon_y^k \Delta_e \varepsilon_s^k dA \mathbf{h}_8(\theta) + \int_A \Delta_e \varepsilon_s^k \Delta_e \varepsilon_y^k dA \mathbf{h}_9(\theta) \right\}, \end{aligned} \quad (6.11)$$

and $\Delta(\cdot)^k = (\cdot)^k - (\cdot)^{k-1}$ is computed only if both $(\cdot)^{k-1}$ and $(\cdot)^k$ are in any of the same strain partition.

6.1.2 Principle of Energy Conservation

After deriving the strain energy of element ${}_e U_{\Delta}^k$, based on its corresponding multi-linear coefficients \mathbf{q}_M , the overall strain energy is examined by considering all of the elements and the corresponding multi-linear coefficients. In a loading step, it is assumed that there exist a number of multi-linear coefficients that governs the behavior of all elements. The multi-linear coefficients that describe the overall deformation are given by

$$\mathbf{q}_M^k \equiv [\mathbf{q}_{11}^{k\top}, \mathbf{q}_{22}^{k\top}, \mathbf{q}_{12}^{k\top}, \mathbf{q}_{66}^{k\top}]^{\top}, \quad (6.12)$$

where ${}^p(\cdot)$ denotes the quantity (\cdot) that exhibits the multi-linear behavior in the corresponding linear partitions of p , which every element of a deforming body is experiencing. Based on the definition given in

Figure 30, each of the multi-linear coefficient term in Equation (6.12) is given by

$$\left\{ \begin{array}{l} \mathbf{q}_{11}^k \equiv [{}^1 q_{11}^k, \dots, {}^{n_A} q_{11}^k]^{\top} \\ \mathbf{q}_{22}^k \equiv [{}^1 q_{22}^k, \dots, {}^{n_B} q_{22}^k]^{\top} \\ \mathbf{q}_{12}^k \equiv [{}^1 q_{12}^k, \dots, {}^{\max(n_A, n_B)} q_{12}^k]^{\top} \\ \mathbf{q}_{66}^k \equiv [{}^1 q_{66}^k, \dots, {}^{n_C} q_{66}^k]^{\top} \end{array} \right. \quad (6.13)$$

Based on Equations (6.11), the term $\mathbf{g}(\Delta\boldsymbol{\varepsilon}^k; \theta) \in \Re^{[n_A+n_B+\max(n_A, n_B)+n_C] \times 1}$ is derived by rearranging and summing up the term ${}_e \mathbf{g}(\Delta {}_e \boldsymbol{\varepsilon}^k; \theta)$ of the elements that correspond to the multi-linear coefficients \mathbf{q}_M^k in Equation (6.12), i.e.,

$$\begin{aligned} \mathbf{g}(\Delta\boldsymbol{\varepsilon}^k; \theta) &\equiv \left[\check{g}_1^k, \dots, \check{g}_{n_\alpha+n_\beta+\max(n_\alpha, n_\beta)+n_\gamma}^k \right]^\top \\ &= \left[\sum_{e_i=1}^{1 E_A^k} \left({}_{e_i} g_1^k \right), \dots, \sum_{e_i=1}^{n_A E_A^k} \left({}_{e_i} g_1^k \right), \sum_{j=1}^{1 E_B^k} \left({}_{e_j} g_2^k \right), \dots, \sum_{j=1}^{n_B E_B^k} \left({}_{e_j} g_2^k \right), \dots \right. \\ &\quad \left. , \sum_{e_i=1}^{1 E_A^k} \sum_{e_j=1}^{1 E_B^k} \left({}_{e_i} g_3^k + {}_{e_j} g_4^k \right), \dots, \sum_{e_i=1}^{n_A E_A^k} \sum_{e_j=1}^{n_B E_B^k} \left({}_{e_i} g_3^k + {}_{e_j} g_4^k \right), \dots \right. \\ &\quad \left. , \sum_{e_l=1}^{1 E_C^k} \left({}_{e_l} g_5^k \right), \dots, \sum_{e_l=1}^{n_C E_C^k} \left({}_{e_l} g_5^k \right) \right]^\top, \end{aligned} \quad (6.14)$$

where the left subscript of the term g denotes the element number that corresponds to the specific multi-linear coefficient, $E_{(\cdot)}$ is the number of element that is associated to the partition (\cdot) . Here, the term g becomes zero if the strain is not observed in the associated partition. The overall incremental strain energy of the total number of elements, U_Δ^k , is thus calculated by multiplying Equation (6.14) to Equation (6.12), i.e.:

$$U_\Delta^k = \mathbf{g}(\Delta\boldsymbol{\varepsilon}^k; \theta)^\top \mathbf{q}_M^k. \quad (6.15)$$

Based on the assumption of principle of energy conservation, substitution of Equation (6.15) into Equation (3.25) yields the framework of the nonlinear characterization as

$$\mathbf{g}(\Delta\boldsymbol{\varepsilon}^k; \theta)^\top \mathbf{q}_M^k = W_\Delta^k, \quad (6.16)$$

where the incremental external work, created by the loading at the l th contact point, is given by

$$W_\Delta^k = \frac{1}{2} \sum_l (\Delta \mathbf{u}_l^k)^\top \Delta \mathbf{f}_l^k.$$

6.2 Stochastic Estimation using Kalman Filter

6.2.1 State Transition and Measurement Models

The state transition model at time step k is thus multiplied with an identity matrix $\mathbf{I} \in \Re^{4n_p \times 4n_p}$, denoted as:

$$\mathbf{q}_M^k = \mathbf{I}\mathbf{q}_M^{k-1}, \quad (6.17)$$

Similar to Equation (4.5), the measurement model is derived as

$$z_W^k = [\mathbf{g}(\mathbf{z}_\varepsilon^k; \theta) - \mathbf{g}(\mathbf{v}_\varepsilon^k; \theta)]^\top \mathbf{q}_M^k + v_W^k, \quad (6.18)$$

where the measured data of the external work and the full-field strain are expressed as

$$z_W^k = W_\Delta^k + v_W^k, \quad (6.19)$$

$$\mathbf{z}_\varepsilon^k = \Delta\varepsilon^k + \mathbf{v}_\varepsilon^k, \quad (6.20)$$

and the uncertainties due to measurement noises are given by the same normal distributions described in Equations (4.2) and (4.3). The unknown true $\mathbf{g}(\Delta\varepsilon^k; \theta)$ is also related to the measured $\mathbf{g}(\mathbf{z}_\varepsilon^k; \theta)$ by

$$\mathbf{g}(\mathbf{v}_\varepsilon^k; \theta) \sim N(\mathbf{0}, \mathbf{P}_g^k), \quad (6.21)$$

where \mathbf{v}_g^k is the same quantity defined in Equation (4.4).

6.2.2 Prediction and Correction

Since the state transition model does not change over time in the p^{th} partition, the prediction of the multi-linear coefficients does not introduce any uncertainty. Subsequently, the prediction is yielded as an uninfluential process as

$$\mathbf{q}_M^{k|k-1} = \mathbf{I}\mathbf{q}_M^{k-1|k-1}, \quad (6.22)$$

$$\mathbf{P}^{k|k-1} = \mathbf{I}\mathbf{P}^{k-1|k-1}\mathbf{I}^\top. \quad (6.23)$$

At time step k , the coefficients that are not within the p^{th} partition become zero. Based on the prediction, the mean correction of the multi-linear coefficients at the partition p is derived by the following function

$$\mathbf{q}_M^{k|k} = \mathbf{q}_M^{k|k-1} + \mathbf{K}^k \left[z_W^k - \mathbf{g}(\mathbf{z}_e^k; \theta)^\top \mathbf{q}_M^{k|k-1} \right]. \quad (6.24)$$

Substitution of Equation (6.24) into the residual that is previously developed in Equation (4.11) yields the correction of covariance for the multi-linear coefficients of the p^{th} partition as

$$\mathbf{P}^{k|k} = \mathbf{P}^{k|k-1} - \mathbf{K}^k \mathbf{g}(\mathbf{z}_e^k; \theta)^\top \mathbf{P}^{k|k-1}. \quad (6.25)$$

Substitution of the predictions and the measured $\mathbf{g}(\mathbf{z}_e^k; \theta)$ into previous Equation (4.13) yields the Kalman gain for the coefficients at the p^{th} partition as

$$\mathbf{K}^k = \mathbf{P}^{k|k-1\top} \mathbf{g}(\mathbf{z}_e^k; \theta) \left\{ \mathbf{g}(\mathbf{z}_e^k; \theta)^\top \mathbf{P}^{k|k-1} \mathbf{g}(\mathbf{z}_e^k; \theta) + P_W^k + \sum_{i=1}^{n_p} \left[(q_M)_{i|k-1}^2 \right] \left(P_g^k \right)_i^k \right\}^{-1}. \quad (6.26)$$

6.2.3 Quantification

After generalizing the prediction and correction to include the characterization of multi-linear coefficients, quantification is sought to determine the performance of the characterization method. Based on the modified Kalman filter, the estimated variance from Equation (6.25) describes the uncertainty of the estimated multi-linear coefficients. The increasing number of multi-linear coefficients, however, introduces more variances, which represent the uncertainty of the characterization results. Within the framework of information theory, measures of the uncertainty associated with a continuous random variable are well studied [173]. The reliability of the estimated multi-linear coefficients is thus quantified by differential entropy as a single quantity to evaluate the uncertainties associated with all the coefficients. The differential entropy proposed to describe the uncertainty of all the multi-linear coefficients is denoted as

$$H(\mathbf{P}^{k|k}) = \frac{1}{2} \ln \left[(2\pi e)^{n_p} \det \mathbf{P}^{k|k} \right]. \quad (6.27)$$

Although the information gain is generally more popular for quantifying uncertainty due to its non-negative nature, the information gain requires a reference distribution and does not derive an absolute value inherent in the distribution. Governed by the computed covariance of all coefficients, the differential entropy has been chosen to measure the uncertainty of the characterization results.

6.3 Numerical Studies

This section investigates the on-line capability and robustness of the stochastic multi-linear characterization method by applying a finite element analysis of an anisotropic material in three numerical studies. The anisotropic material chosen for the studies is AS4D/9310 graphite/epoxy laminate. The reported properties of the material are listed in Table 18. A finite element analysis has been developed to prove the concept of the characterization method. Three multi-linear partitions were defined for the numerical examples. Based on the known elastic properties in their linear region, the multi-linear coefficients used for the numerical examples are listed in Table 18. Each set of the multi-linear coefficients contains three values. The incremental partition values that define the partition ranges of each strain quantity are listed in Table 19.

Table 18 Material parameters of the AS4D/9310 graphite/epoxy laminated specimen for numerical examples.

Material Constants	Value	Multi-linear Coefficients	Value
Elastic Modulus E_1 [MPa]	1.34×10^5	\mathbf{q}_{11}^* [MPa]	$[1.34, 0.94, 0.75] \times 10^5$
Elastic Modulus E_2 [MPa]	7.71×10^3	\mathbf{q}_{22}^* [MPa]	$[7.76, 5.41, 4.33] \times 10^3$
Shear Modulus G_{12} [MPa]	4.31×10^3	\mathbf{q}_{12}^* [MPa]	$[2.56, 1.25, 0.80] \times 10^3$
Poisson's Ratio ν_{12}	0.33	\mathbf{q}_{66}^* [MPa]	$[4.31, 3.02, 2.41] \times 10^3$
Fiber angle θ [$^\circ$]	30		

Table 19 Incremental partition value of each strain quantity for numerical examples.

Parameter	Value
$\Delta\check{\varepsilon}_1^*$	3.00×10^{-4}
$\Delta\check{\varepsilon}_2^*$	6.00×10^{-4}
$\Delta\check{\varepsilon}_6^*$	1.00×10^{-3}

Figure 31 shows the boundary conditions and geometrical configuration of the specimen used in the numerical examples. A tensile loading is simulated on a square specimen, sized 100mm×100mm×3mm and approximated with 100 finite elements. The bottom of the specimen is fixed in all directions and the top of the specimen is fixed horizontally. Point-wise forces rang-

ing from 200N to 24000N were applied over 200 time steps and thus, 200 set of measurements were obtained from this experiment.

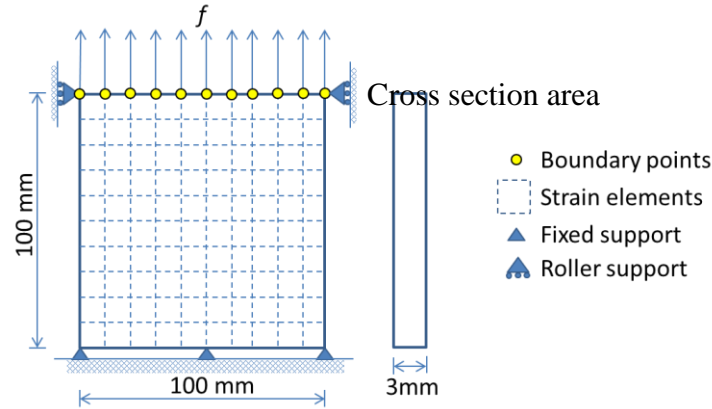


Figure 31 Boundary conditions and geometry details of the AS4D/9310 specimen.

6.3.1 Estimation of Multi-linear Coefficients (Example 1)

Example 1 solves the characterization of the multi-linear coefficients of in the finite element analysis by assuming the same three partitions with the ones set in the simulation, as described by the incremental partition values listed in Table 20. The aim of this study is to examine whether the characterization method can estimate the multi-linear coefficients under the influence of uncertainties. The noise used in the measurements, and the empirical knowledge of the measurement uncertainties are listed in Table 21. The prior knowledge on mean and covariance are additionally listed in Table 21. It is to be noted that the prior mean is set to be 50% more than the true multi-linear coefficients, and the prior covariance for each coefficient is set to be a constant value 5×10^{-10} .

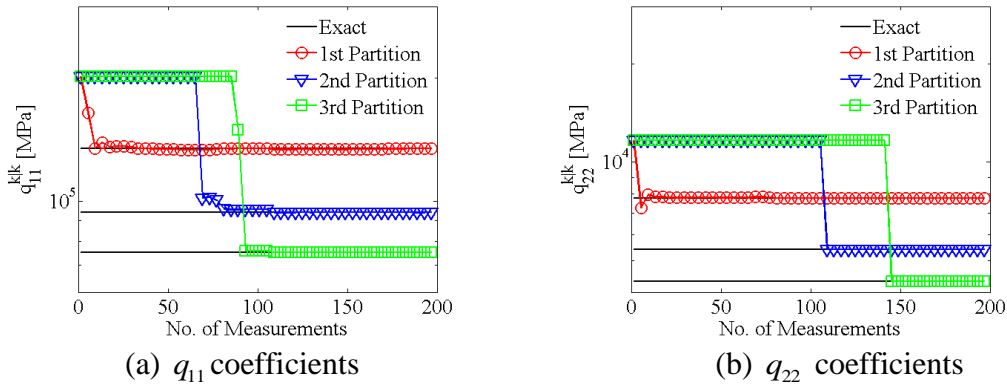
Table 20 Incremental partition values used for Example 1.

Parameter used in Simulation	Value	Parameter for Proposed Approach	Value
$\Delta\tilde{\varepsilon}_1^*$	3.00×10^{-4}	$\Delta\tilde{\varepsilon}_1$	3.00×10^{-4}
$\Delta\tilde{\varepsilon}_2^*$	6.00×10^{-4}	$\Delta\tilde{\varepsilon}_2$	6.00×10^{-4}
$\Delta\tilde{\varepsilon}_6^*$	1.00×10^{-3}	$\Delta\tilde{\varepsilon}_6$	1.00×10^{-3}

Table 21 Measurement covariance and prior knowledge used in Example 1 ($n_p=3$).

Parameter for Measurement	Value	Parameter for Proposed Approach	Value
P_e^*	1.00×10^{-5}	P_e	1.00×10^{-5}
P_w^*	1.00×10^{-11}	P_w	1.00×10^{-11}
$\mathbf{q}_M^{0 0}$			$1.5\mathbf{q}_M^*$
$P_{i,j}^{0 0}$			$5 \times 10^{10}, \forall i, j = \{1, 2, \dots, 4n_p\}$

Figures 32(a)-(d) show the transition of the estimated coefficients over the number of measurements. Although twelve-dimensional spaces are handled in the nonlinear characterization problem, the characterization method estimated adequate multi-linear coefficients after taking 200 measurements. It is shown that both q_{11} and q_{22} coefficients converged to the exact solutions at the very first few steps, where the strains are in their first partitions. This is unlike q_{12} and q_{66} coefficients, where these coefficients fluctuated before converging to the exact solutions. It is conjectured that the shear behavior and the correlation between the tensile and transverse behavior were not obvious in the first few measurements of the simulated tensile test. As more information about the rest of the partitions is observed, the coefficients are shown to have converged from the prior knowledge to the exact values. The recursive estimation mechanism of the prediction and correction processes made the estimation performed on-line at every acquisition of measurements. The identification after 200 measurements thus indicates the practical feasibility of the characterization method.



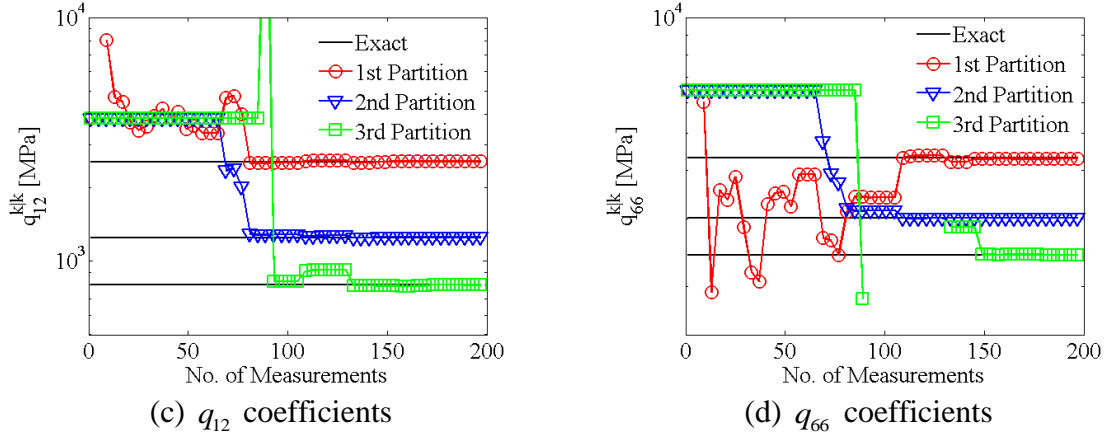
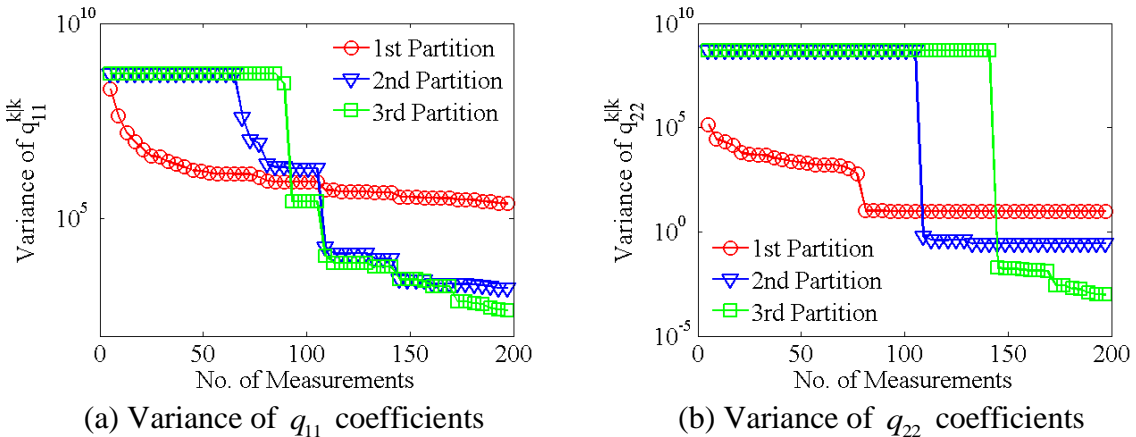
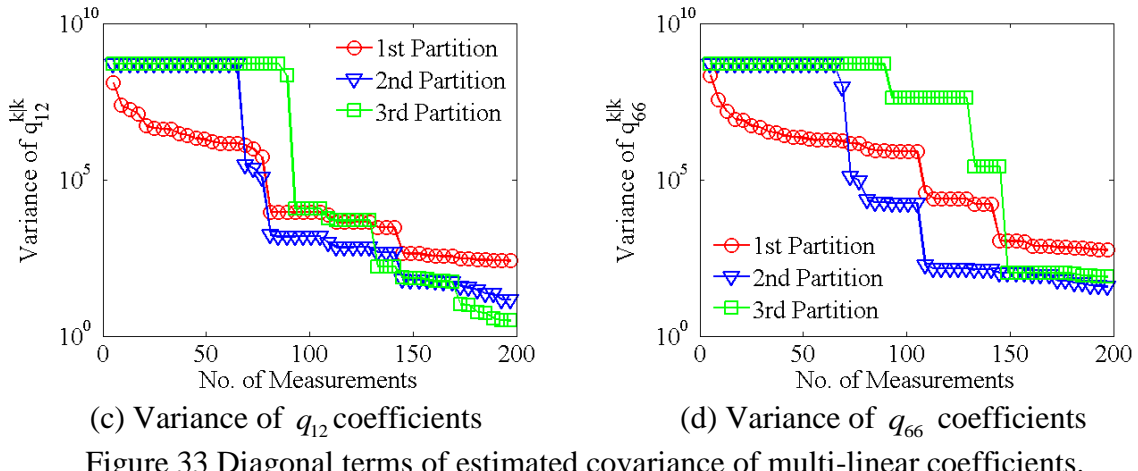


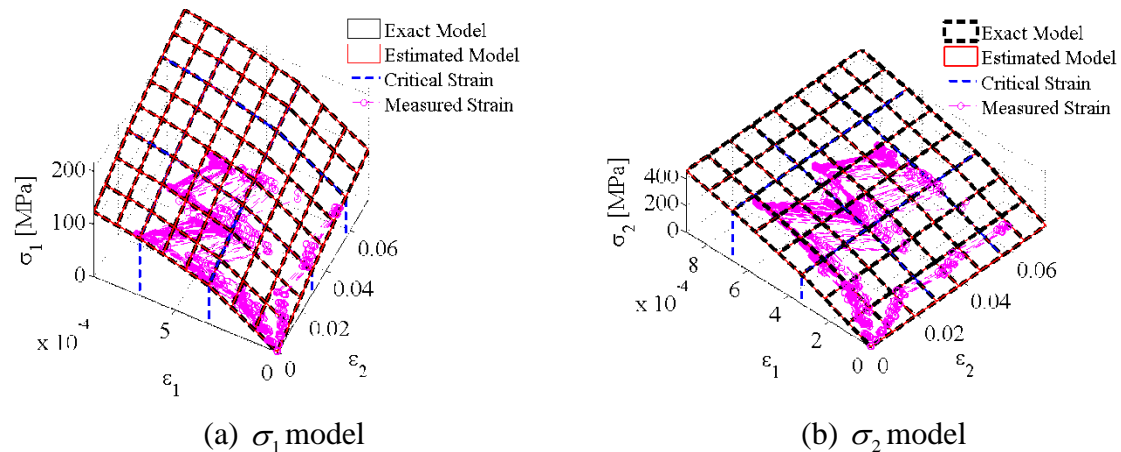
Figure 32 Transition of the estimated multi-linear coefficients using 3 partitions.

Figure 33 shows the certainty of each estimated multi-linear coefficient in terms of variances, and also the increase of certainty with the acquisition of measurements. The variance of a particular coefficient starts to converge to zero values whenever the measurements contain information on the partition. The decrease of the variances also indicates that the estimation of coefficients is being converging.





Figures 34(a)-(c) qualitatively show the comparison between the stress-strain relations, created by the estimated coefficients, and the relations computed from the exact coefficients, after 200 measurements. Note that the first stress-strain relations are shown as Exact Model and the later computed stress-strain relations are shown as Estimated Model. The measured strains are also plotted on each stress model. The critical strain further shows the interval between different partitions. It is shown in the figures that the final estimates of coefficients have created stress models that match the exact models, under the influence of uncertainties. Figure 34(d) shows the transition of the differential entropy. The convergence of differential entropy is as expected since the variances of each estimated coefficient decrease. This result demonstrates the differential entropy as the quantity to describe the uncertainty of the characterization results.



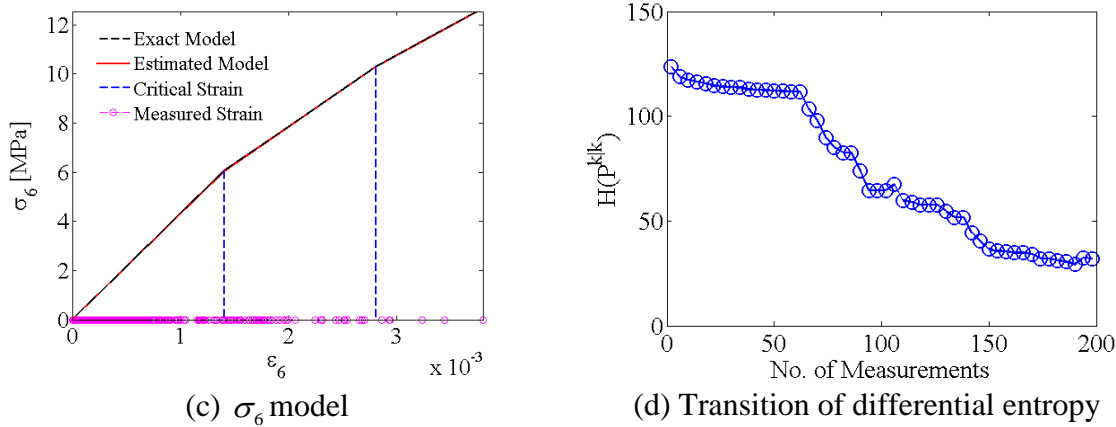


Figure 34 Comparison of the estimated stress-strain relations and the differential entropy of the first example.

6.3.2 Certainty of Multi-linear Coefficients under Various Noises (Example 2)

Example 2 investigates the noise minimization capabilities of the characterization method in identifying the multi-linear coefficients under various noise conditions. Table 22 lists the range of the noise added to the measurements, and the empirical and prior knowledge used in this example.

Table 22 Parameters for the reliability study of nonlinear characterization method.

Parameter for Meas- urement	Value	Parameter for Proposed Framework	Value
P_{ε}^*	$1.00 \times 10^{-6} \rightarrow 1.00 \times 10^{-4}$	P_{ε}	$1.00 \times 10^{-6} \rightarrow 1.00 \times 10^{-4}$
P_W^*	$1.00 \times 10^{-10} \rightarrow 1.00 \times 10^{-7}$	P_W	$1.00 \times 10^{-11} \rightarrow 1.00 \times 10^{-9}$
		$\mathbf{q}_M^{0 0}$	$1.5\mathbf{q}_M$
		$P_{i,j}^{0 0}$	$5 \times 10^{10}, \forall i, j = \{1, 2, \dots, 4n_p\}$

Figures 35(a) and (b) show the error percentage and the differential entropy under the studied ranges of measurement noise. It can be seen that the average absolute error increased from 0% to 5% by increasing the measurement noise in both full-field strain and external work. It is found that the characterization results become less certainty when measurement noise increases. When the uncertainties are different, the differential entropy is also influenced.

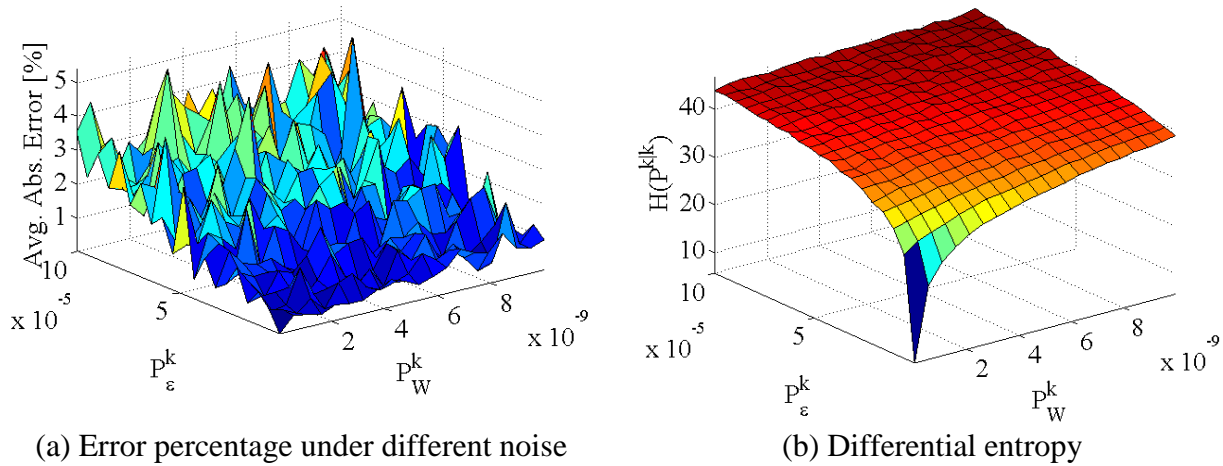


Figure 35 Comparison between the error analysis and information entropy of the estimation results at the 200th step.

6.4 Summary

The stochastic multi-linear characterization method is presented to approximate the nonlinear behavior of anisotropic materials on-line, under the assumptions that the materials are rate-, path- and temperature-independent. A multi-linear framework has been proposed for characterizing the multi-linear coefficients based on the full-field strains and external work. The modified Kalman filter, presented previously in the linear characterization method, is further generalized to determine the multi-linear coefficients of anisotropic materials. The differential entropy is utilized as a single quantity to evaluate the uncertainties associated with all the estimated coefficients. This allows the performance of the multi-linear characterization method to be evaluated against any source of uncertainties.

Two numerical studies were performed based on a FEA, which resemble a tensile test of an anisotropic material. The first study, investigating the transitional performance of the characterization results, shows that the characterization method is able to estimate the multi-linear well and steadily with reduced uncertainty under measurement noise. During the deformation, the mean of a new coefficient is identified on-line when strain values are observed in a new partition. This is confirmed by the transition of differential entropy that shows distinct levels of information content over the number of measurements when new partition is observed. The second study demon-

strates that the error is maintain at an average of 5% even under various measurement noise, if exact measurement covariance and prior knowledge is available, making the method to achieve optimal characterization effectively.

The stochastic linear and multi-linear characterization methods are subsequently experimentally evaluated in the next Chapter to demonstrate its on-line capability and validity in characterizing nonlinear behavior of materials.

Chapter 7

Experimental Studies

Stochastic linear and multi-linear characterization methods and a data fusion technique have been proposed in the previous three Chapters. This Chapter presents experimental studies of the proposed framework to the linear and nonlinear characterization of materials. Section 7.1 covers the experimental characterization procedures, which include the experimental modules and system, used for evaluating the performance of the proposed framework. Both modules and system utilize a digital camera and a load cell to acquire the full-field strains and external work, unlike the conventional method which utilizes contact sensors to obtain strain measurements. Section 7.2 covers the evaluation of the proposed framework in terms of applicability, efficiency and robustness. The experimental evaluation includes the characterization of elastic constants, performance under different image resolutions, and the characterization of material up to nonlinear region.

7.1 Experimental Characterization Procedures

An overall view of the experimental procedures that implement the stochastic linear and multi-linear characterization methods is presented in Figure 36. The main feature of the characterization procedures is the use of only a digital camera and a load cell in the sensing module to acquire all the essential measurements from the material testing, unlike the conventional standard mechanical testing methods that require embedded/contact strain sensors in material characterization. The energy-based characterization requires the measurements of the boundary displace-

ment and force and the full-field strain, which can be furnished by three different modules in the proposed method.

The full-field measurement module (see Appendix 2) derives the boundary displacement \mathbf{z}_u^k as well as the full-field strain \mathbf{z}_e^k based on the images supplied by the other modules, namely the sensing module and the preprocessing module. It is to be noted that although \mathbf{z}_u^k can also be measured by an external device, such as an internal displacement encoder, previous experimental analysis shows that the displacement is not correctly measured due to the slippage movement within the material testing grips. The resulted \mathbf{z}_u^k further derives the external work for the energy-based characterization by multiplying itself with the boundary force \mathbf{z}_w^k for the energy-based characterization measured by the load cell in the sensing module.

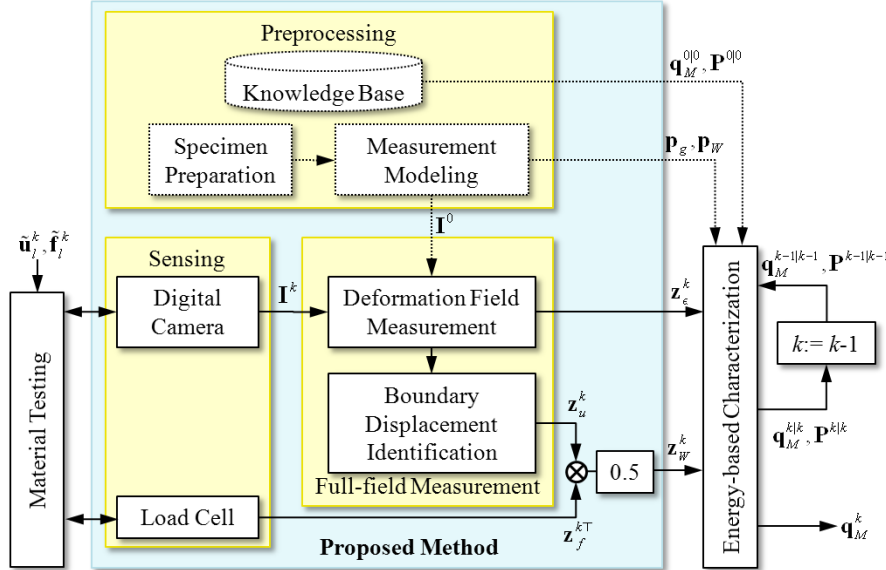


Figure 36 Overview of the experimental characterization procedures.

Prior to acquiring the measurements at step k , the preprocessing module (see Appendix 2) produces the prior knowledge on the mean $\mathbf{q}_M^{0|0}$ and the covariance $\mathbf{P}^{0|0}$ as well as the variances \mathbf{P}_g and P_w to the energy-based characterization at step $k = 0$. All in all, with the modeled prior knowledge and variances, the proposed framework hence performs on-line characterization of materials at every acquisition of measurements.

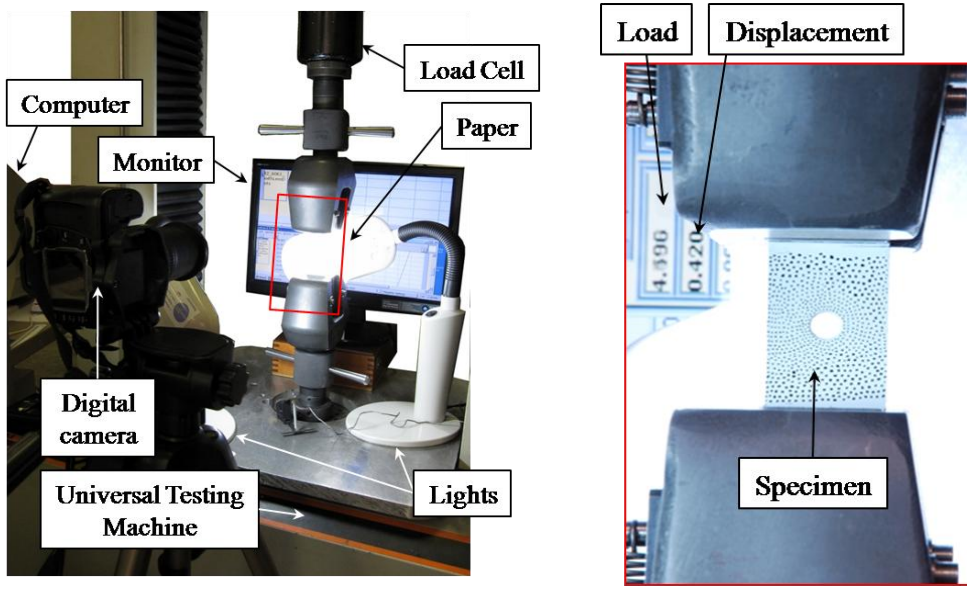
7.1.1 System

The system developed for implementing the proposed framework primarily consists of the hardware components and the specimen, which are shown in Figure 37(a) and (b). The digital camera used was a PointGrey Flea2 FL2G-50S5C CCD Camera. The load cell was an Instron A509-5 (Catalog No. 2512-401) model that can measure up to 150 kN load capacity. The testing machine used in the developed system was an Instron 4206 electromechanical universal testing machine that is displacement-controlled to deform specimen at a 0.2mm/min loading rate. The computer system hosting the user interfaces is a Dell Vostro 420 Minitower Computer with Pentium Core i5 and 2GB of RAM. The equipment models and their settings used in the developed system are summarized in Table 23. A user interface, created by a library of Labview functions, allows the user not only to maintain the synchronous acquisition of both load cell readings and digital images, but also to control the testing machine. The rest of the functions that perform the tasks in the proposed method are performed by a library of functions written in Matlab language.

Table 23 Equipment models and their settings used in the developed experimental system.

Equipment	Model	Settings/Specifications
Digital Camera	PointGrey FL2G-50S5C	5 MPixels
Load Cell	Instron A509-5	150kN capacity
Testing Machine	Instron 4206	150kN capacity, 0.2mm/min loading rate
Computer	Dell Vostro 420	Pentium Core i5, 2GB RAM

Figure 37(a) also shows the light condition that is controlled by two light sources that are each placed at the back and the front of the specimen. To minimize the shadow effect due to insufficient lights, papers are used to create more uniform distribution of lights on the specimen. The monitor placed behind the specimen shows not only the interfaces developed for the proposed framework, but also the load cell reading at the corresponding cross head displacement of the testing machine, for visual references. The specimen, located at the red frame shown in the figure, is enlarged in Figure 37(b). It is shown that a random distribution of black dots, with sizes between 4 and 6 pixels, are marked on the white non-reflective sprayed background.



(a) Hardware components

(b) Specimen

Figure 37 Developed experimental system for the proposed on-line nonlinear framework.

7.2 Experimental Results

This section investigates the results of the experimental studies of the proposed framework via the stochastic linear and multi-linear characterization methods. The first experiment solves a material characterization problem resembling the linear characterization based on full-field measurements. The continuum capability of the proposed framework is also examined with specimens of different shapes. After identifying the considerable effect of sensor accuracy to the proposed framework, the applicability of the proposed framework to determining the nonlinear behavior of material is described in the second experiment.

7.2.1 Stochastic Linear Characterization (Experiment 1)

Experiment 1 performs three tensile tests on isotropic aluminum T6061 specimens to investigate the effectiveness and validity of the stochastic linear characterization method. The material properties and the referenced elastic constants, computed by a plane stress model, are presented in Table 24. Due to material isotropy, two elastic constants, q_{11}^* and q_{22}^* , are identical. Figure 38 shows the test specimens that were cut into three different specimen shapes; they are open-hole,

single notch and double notch specimens, which are used for each test. Geometry details of these specimens are listed in Table 25.

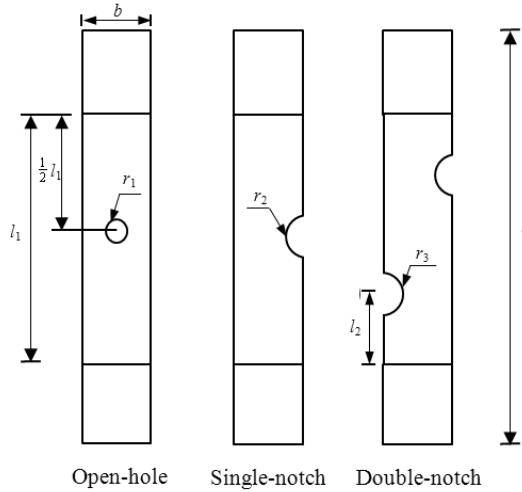


Figure 38 Types of specimen shape used in mechanical tests: Open-hole (Test 1), Single-notch (Test 2) and Double-notch (Test 3).

Table 24 Material parameters of the specimens (Experiment 1).

Material Property	Value	Referenced Elastic Constant	Value
Young's Modulus, E [MPa]	69.00×10^3	q_{11}^* [MPa]	77.43×10^3
Poisson's Ratio, ν	0.33	q_{22}^* [MPa]	77.43×10^3
		q_{12}^* [MPa]	25.55×10^3
		q_{66}^* [MPa]	25.94×10^3

Table 25 Geometry details of the specimens

Geometry	Value
Overall length, l_3 [mm]	204.00
Initial distance between the grip and one of the notches, l_2 [mm]	24.32
Initial distance between grips, l_1 [mm]	93.84
Radius of the open hole, r_1 [mm]	4.69
Radius of the side notch, r_2 [mm]	5.56
Radius of the two notches, r_3 [mm]	6.37
Width, b [mm]	38.27
Thickness, t [mm]	3.19

Finite element analyses were performed to provide comparison results to the experimental findings. Figures 39(a)-(c) show the boundary conditions of the specimen at each test, and the comparison of the derived boundary force-displacement and the finite element results. The boundary conditions shown in Figures 39(a)(i), (b)(i) and (c)(i) are modeled as tensile tests, where the bottom is fixed horizontally and vertically and the top is fixed horizontally with forces applied vertically. Based on the same boundary force, the results indicate a good agreement between the measured boundary displacement and the FEA solutions.

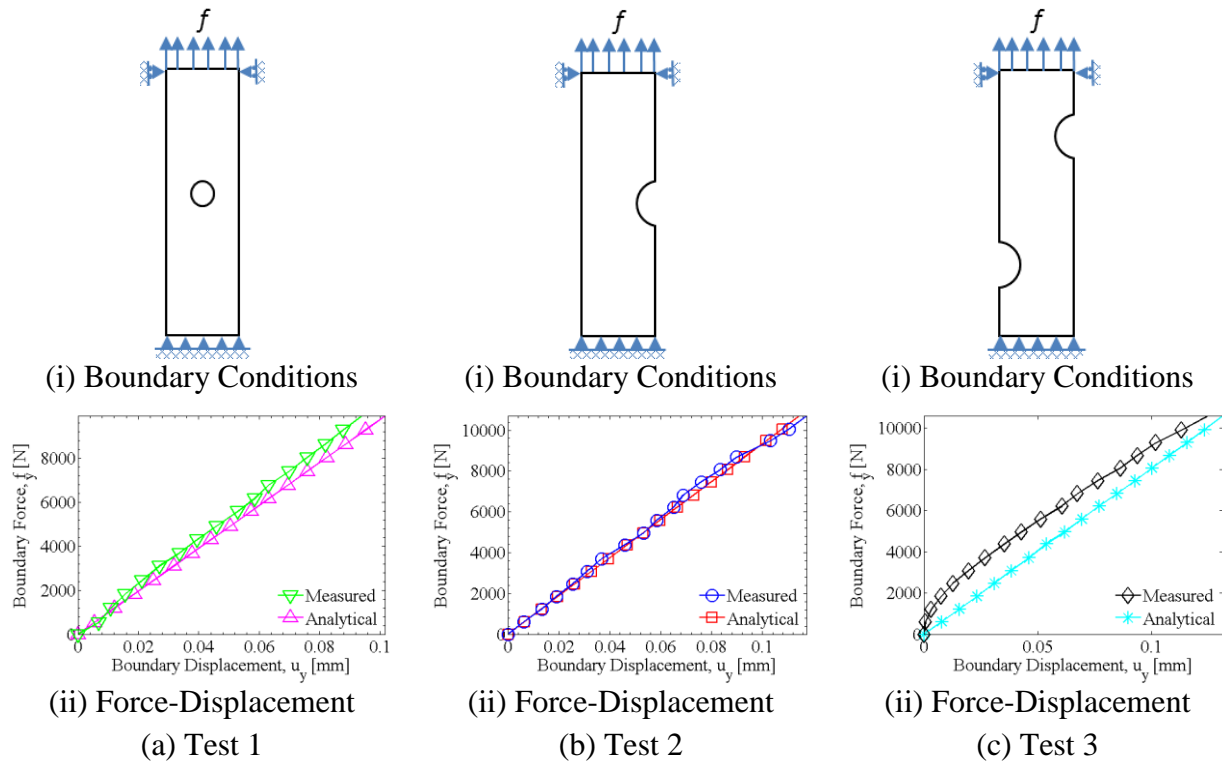


Figure 39 Boundary conditions of the specimen and the comparison between the measured force-displacement data and the FEA solutions.

Figures 40, 41 and 42 show the comparison between the full-field measurements and the FEA solutions at the last loading step. The certainty of the measurements with respect to the FEA results is additionally shown in the transition of the computed strain variances plotted in these figures. Figures 40(a)-(e) qualitatively show adequate strain and displacement distribution at the concentration areas. The results indicate that uncertainties exist in the experimental measurements contributed to the inconsistent match with finite element results. This is further confirmed

with the full-field strain and displacement results shown in Figures 41(a)-(e) and 42(a)-(e). The experimental measurements in Figures 40(d)-(e) also show that the specimen is rotated from the side as the displacements on the horizontal axis are exhibiting non-symmetrical deformation. Interestingly, the measured full-field displacements in Figures 41(d)-(e) and 42(d)-(e) confirm such rotation and it is suggested that such movement is caused by the slippage from the mechanical grips of the testing machine. Figures 40(f), 41(f) and 42(f), meanwhile, show that the strain variance exponentially increased over the loading steps. The computed variance is fed into the stochastic linear characterization method as part of the empirical knowledge.

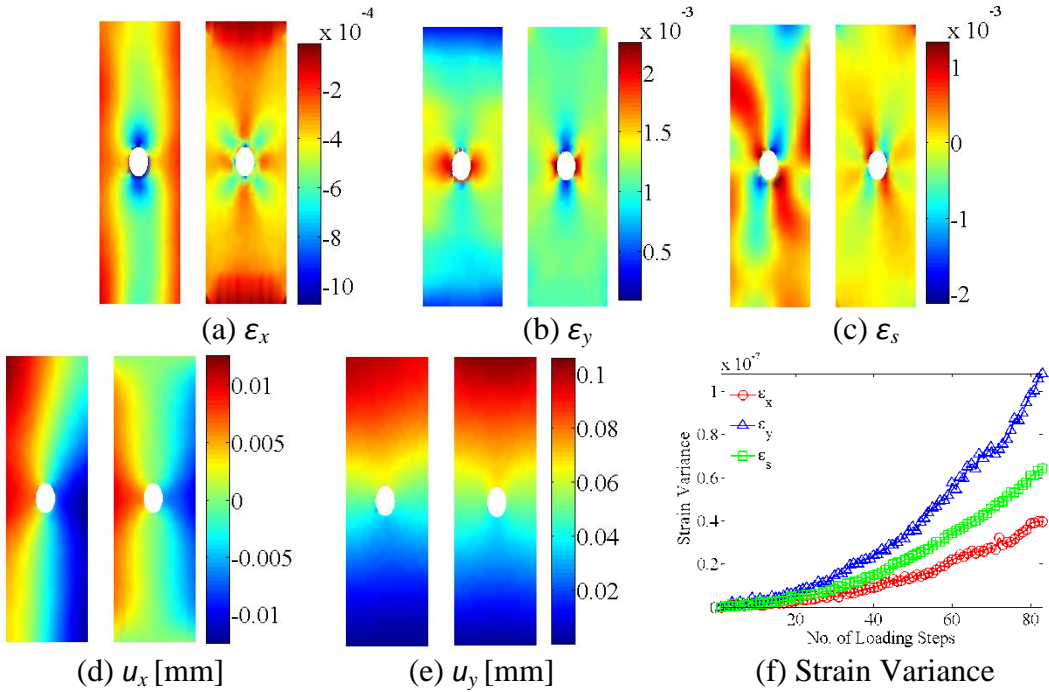
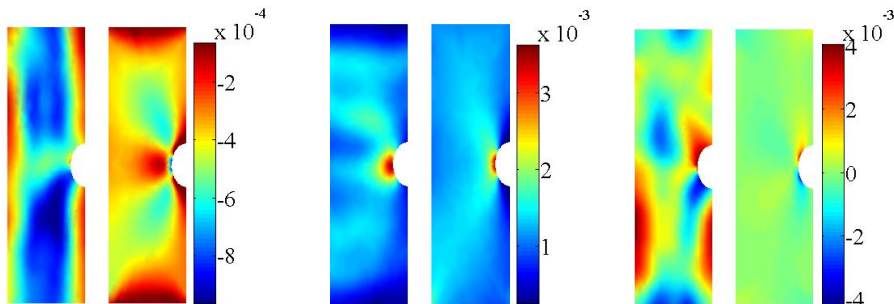


Figure 40 Test 1: Full-field measurements (left) and FEA solutions (right) after 83 loading steps, and the transition of computed strain variances.



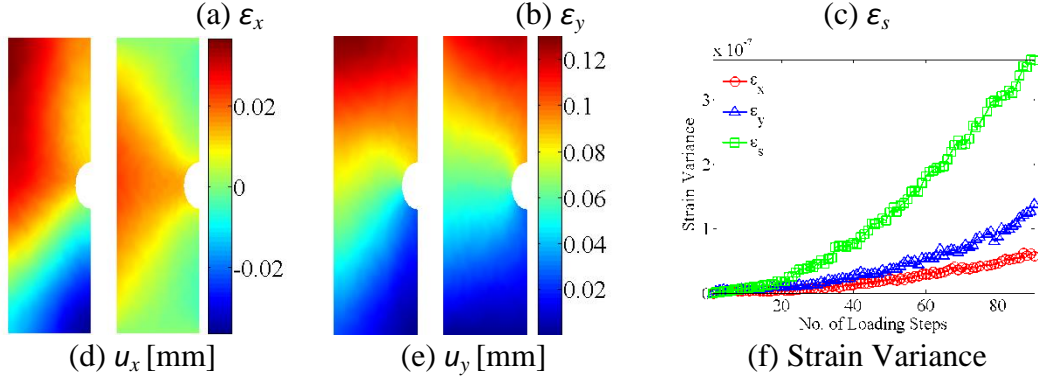


Figure 41 Test 2: Full-field measurements (left) and FEA solutions (right) after 89 loading steps, and the transition of computed strain variances.

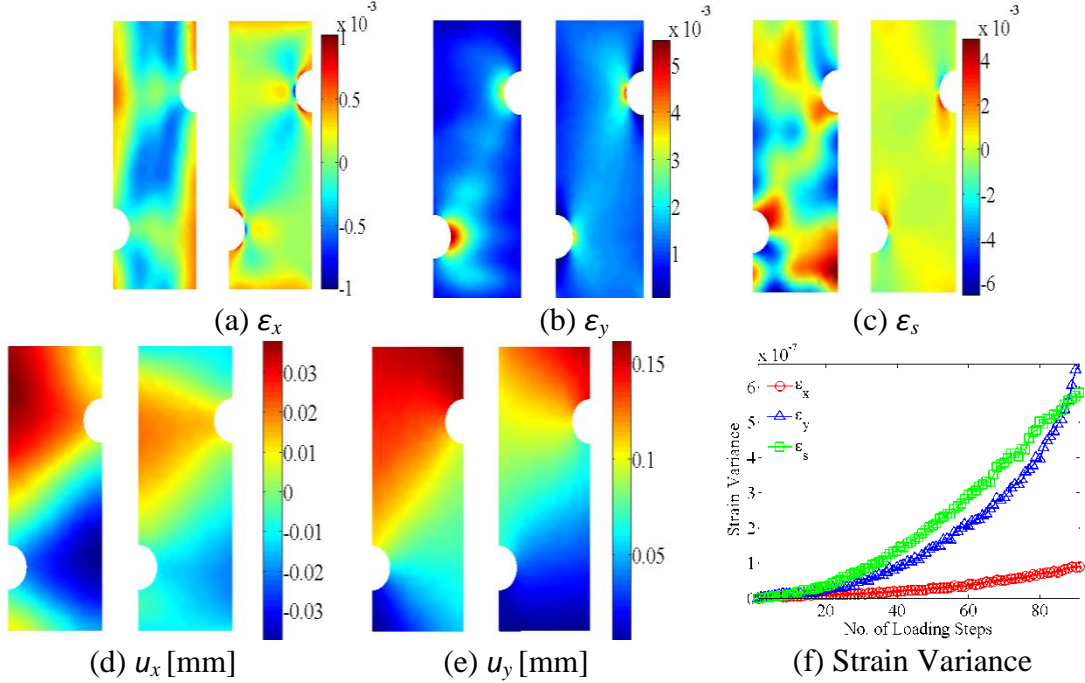


Figure 42 Test 3: Full-field measurements (left) and FEA solutions (right) after 91 loading steps, and the transition of computed strain variances.

6.4.1.1 Estimation of Elastic Constants

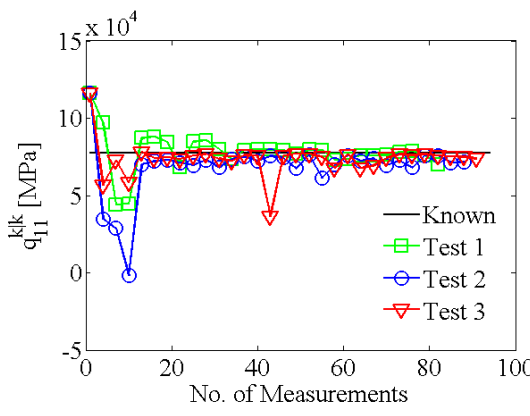
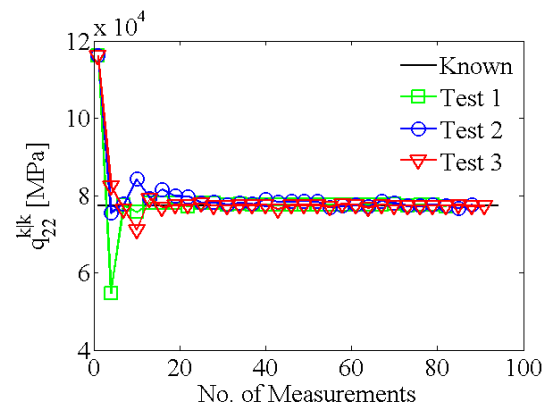
Having observed the transition of full-field measurements and strain variance in the loading steps,

Error! Reference source not found. lists the prior and empirical knowledge that was used in the on-line nonlinear framework. Figures 43(a)-(d) show the transition of the estimated elastic

constants plotted against the known values in each test. The transition shows that the estimated constants converged to the known values after 10 measurements. It is additionally show that test 1, 2 and 3 has the least, average and most convergence rate, respectively. Under the same testing environment with different specimen shape, it is found that changing the specimen shape also influenced the convergence rate. This is further confirmed in the differential entropy of each test plotted in Figure 44. The results exhibited that Test 1 has the least information content, Test 2 has a moderate information content, and Test 3 contains the most information content of the estimated constants, due to the higher covariance of the estimated constants that is exhibited in the fluctuating transition of constants. Although only the constants q_{11} and q_{66} would be sufficient for determining the elastic behavior of isotropic material, this experiment exhibits the capability of characterizing the multiple constants, derived from the energy-based characterization, in a single test. This is further confirmed with the convergence of the same constants q_{11} and q_{22} in Figures 43(a) and (b).

Table 26 Prior and empirical knowledge for Test 1, 2 and 3.

Prior Knowledge	Value	Empirical Knowledge	Value
Mean, $\mathbf{q}^{0/0}$ [MPa]	$1.5\mathbf{q}_M^*$	P_w^k	10
Covariance, $\mathbf{P}^{0/0}$	$\text{diag}([1,1,1,1]) \times 10^{10}$	\mathbf{p}_e^k	1×10^{-10}

(a) q_{11} (b) q_{22}

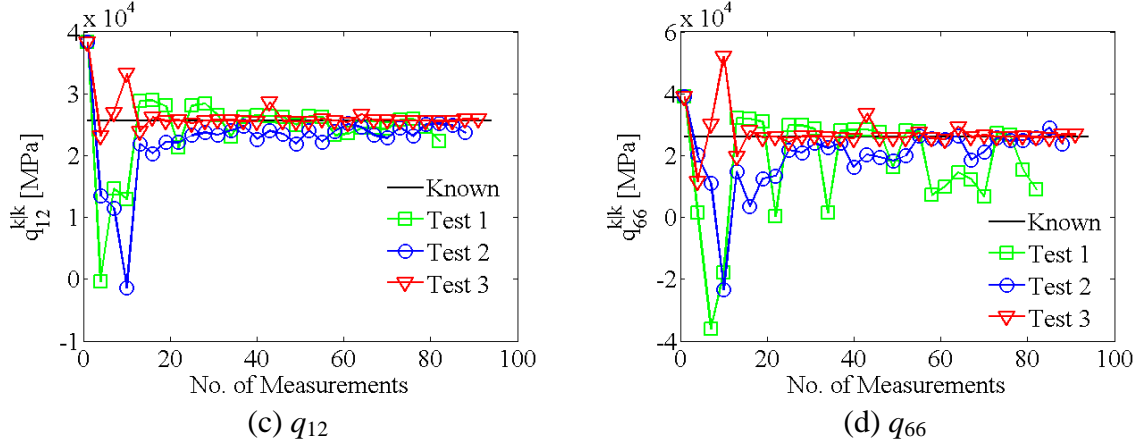


Figure 43 Transition of the estimated mean.

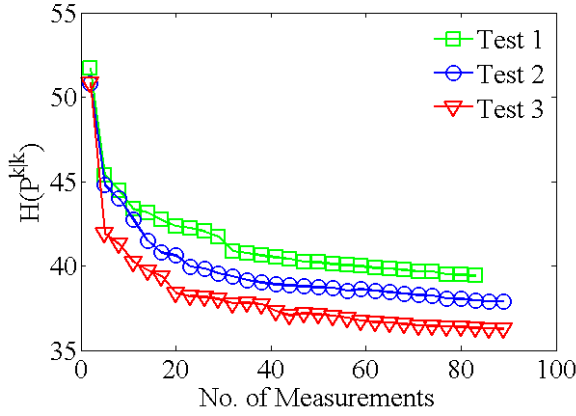


Figure 44 Differential entropy of each test.

Figures 45(a) and (b) show the transition of the two identified elastic moduli from each test. The linear method was shown to estimate the adequate Young's modulus and Poisson's ratio after 10 measurements. Since full-field measurements exhibit lateral and transverse strain simultaneously at each loading step, the stochastic linear characterization method could also reliably identifies the Poisson's ratio. Table 27 quantitatively lists the characterization results of each test in terms of the identified constants after taking their last measurements. The proposed framework settles to the known Young's modulus within 4% difference, and to the known Poisson's Ratio within 13%. The settling results from their prior knowledge on the mean, which is 150% from the known values, indicate that the uncertainty in both prior knowledge and empirical knowledge of the characterization results is recursively minimized through the linear method. Fluctuation of

results is observed in the first 20 measurements. This indicates that the Kalman filter requires initial few steps before an optimized Kalman gain is computed to minimize the random error.

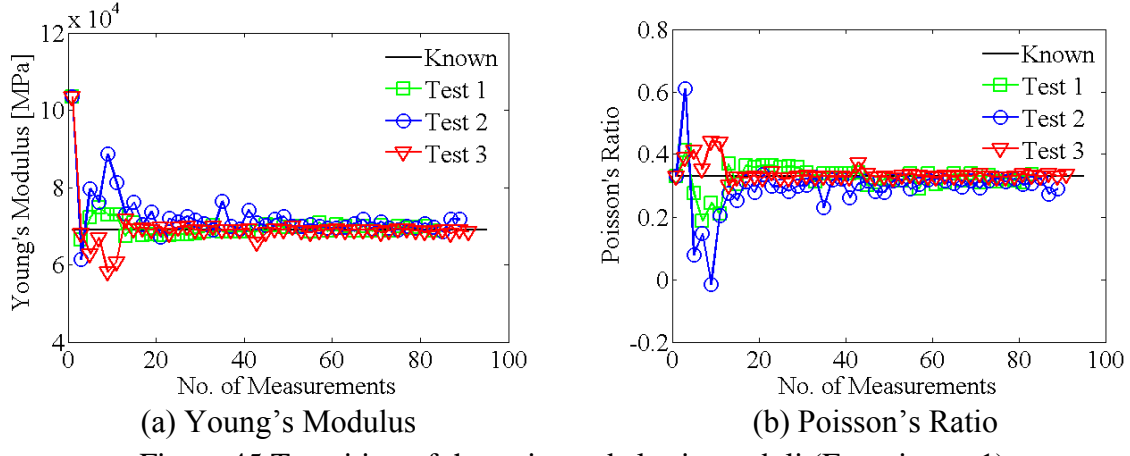


Figure 45 Transition of the estimated elastic moduli (Experiment 1).

Table 27 Error of the estimated elastic parameters in each test (Experiment 1).

Parameter	Test 1	Test 2	Test 3
Young's Modulus	0.33%	3.96%	0.61%
Poisson's Ratio	1.85%	12.30%	1.61%

6.4.1.2 Performance under Different Full-field Strain Noise

After identifying the effectiveness of the stochastic linear characterization method, the second experimental study focused on the effect of the contemporary full-field strain sensors' accuracies to the validity of the proposed framework. As described in Section 7.1, a digital camera system was utilized to measure the full-field strains. Table 29 lists the current widespread camera resolution that is equipped in most digital cameras and the full-field strain resolution that was studied in the experimental work of [141]. The experimental findings reported that standard deviations of full-field strain measurement, ranging from $12.3\mu\varepsilon$ to $36.2\mu\varepsilon$, were found when camera resolutions, ranging backwards from 15.1MPixels to 2.1MPixels, were used. Noise study, based on these available experimental data, was performed numerically to investigate the capability of the proposed framework under different camera resolutions. The anisotropic material used for this numerical study is the AS4D/9310 graphite/epoxy laminate, with the same material parameters listed in Section 6.4 of the previous Chapter. The experimental data is applied as measurement uncertainties to the same FE model shown in Section 6.4. The FE model is governed by the same

elastic constants and loaded from 0N to 12000N in the tensile direction. The prior knowledge, empirical knowledge, and studied noise range are listed in Table 29. Since this study focuses on the noise effect from full-field measurements, the external work is modeled deterministically with no noise.

Table 28 Standard deviations of full-field strains with respect to different camera resolutions (Experimental data obtained from [141]).

Camera Resolution [MPixels]	Full-field Strain Standard Deviation [$\mu\epsilon$]
2.1	36.2
3.1	25.4
5.0	20.1
8.0	17.0
12.0	13.0
15.1	12.3

Table 29 Parameters for the noise study ($\forall i \in \{1, 2, 6\}$).

Parameter for measurement	Value	Parameter for proposed framework	Value
$\sqrt{P_{\varepsilon_i}^*}$	$0\mu\epsilon \rightarrow 45\mu\epsilon$	$\sqrt{P_{\varepsilon_i}}$	$0\mu\epsilon \rightarrow 45\mu\epsilon$
P_w^*	0	P_w	0
		$\mathbf{q}^{0 0}$	$1.5\mathbf{q}_M^*$
		$P_{ii}^{0 0}$	1.00×10^{10}

Figures 46(a)-(d) show the percent error of the elastic constants under different strain measurement noise. The results were obtained based on the final estimates of the elastic constants after 100 measurements. Each final estimate was derived by averaging 50 sets of 100 measurements at each studied noise to reduce the effect of random error. The resulted data was fitted polynomial regression with a second order polynomial. Based on the polynomial regression models, it is shown that the error in the elastic constants ranges from 0% to 60% in the noise study, where q_{11} and q_{66} hold the most and least accurate results, respectively. Despite the random error is reduced by averaging the final estimates, the fluctuation of the gathered data can be attributed to the discretization error of the FE model and the truncation error in deriving the optimal Kalman gain.

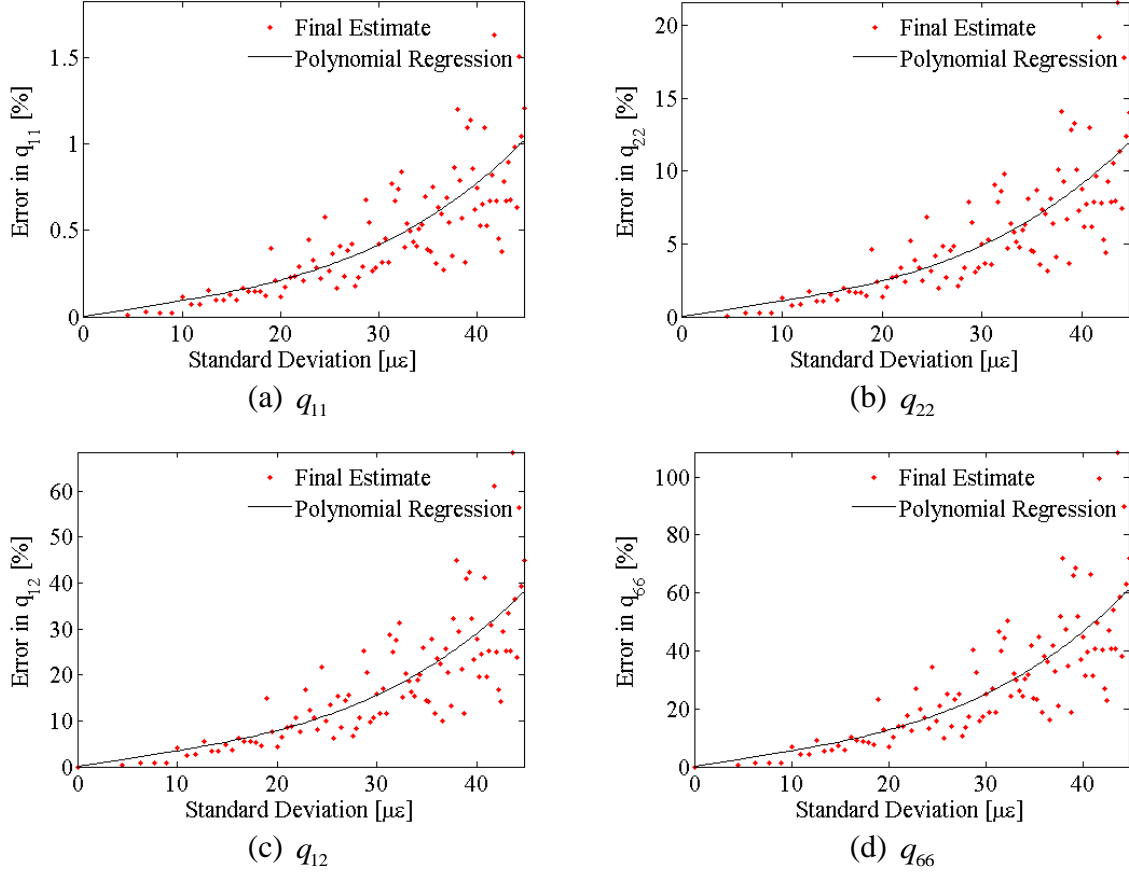


Figure 46 Performance of the proposed framework under different standard deviation of strains after 100 measurements.

Table 30 lists the maximum error of the proposed framework when the reported experimental data of strain standard deviations are modeled in the full-field strain measurements. The current reported strain error of fibre Bragg grating sensor is $30\mu\epsilon$ [142] and strain gage is $0.52\mu\epsilon$ [143]. Although the current camera system has a standard deviation that is 24% more than the strain gage error, the advancement of digital camera technology has allowed higher and affordable camera resolution, making the proposed framework to achieve higher accuracy.

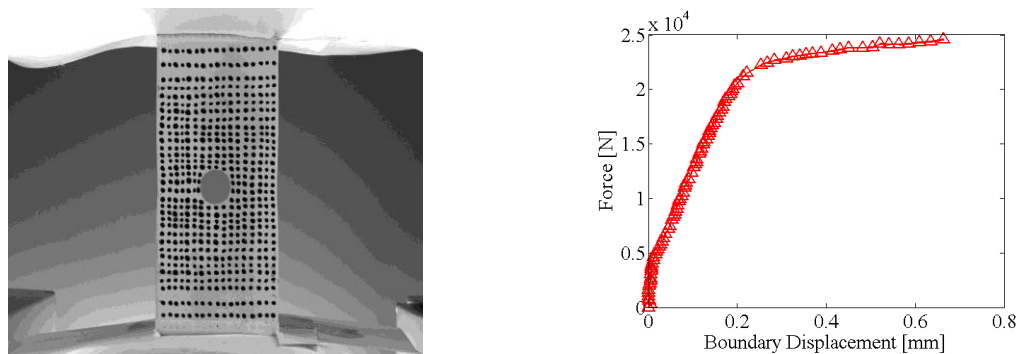
Table 30 Projected accuracy of the proposed framework with respect to different camera resolution.

Camera Resolution [MPixels]	Full-field Strain Standard Deviation* [$\mu\epsilon$]	Proposed Framework Maximum Error [%]
2.1	36.2	37.50
3.1	25.4	18.36
5.0	20.1	12.66
8.0	17.0	10.38
12.0	13.0	7.60
15.1	12.3	7.11

*Experimental data obtained from [141].

7.2.2 Stochastic Multi-linear Characterization (Experiment 2)

Experiment 2 applies forces to a open-hole specimen that has the same geometrical configurations with Test 1, until the specimen reaches the nonlinear region. The aim of this experiment is to investigate the effectiveness of the stochastic multi-linear characterization of materials up to the nonlinear region. Figure 47(a) shows the specimen that was deformed to 25000N after 190 measurements. The force and boundary displacement deformation, which were measured by a load sensor and derived from the full-field displacement calculations, respectively, are shown in Figure 47(b).



(a) Deformed specimen (b) Boundary force-displacement
Figure 47 Deformed specimen and the boundary force-displacement of Experiment 2.

Figures 48(a)-(c) show the full-field strains that were measured in Experiment 2 after 190 measurements. These strain measurements, together with the boundary force-displacements, are utilized for characterizing the nonlinear behavior, using the proposed framework.

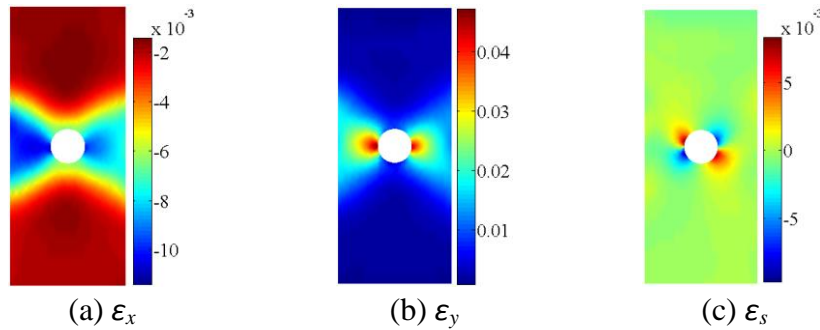
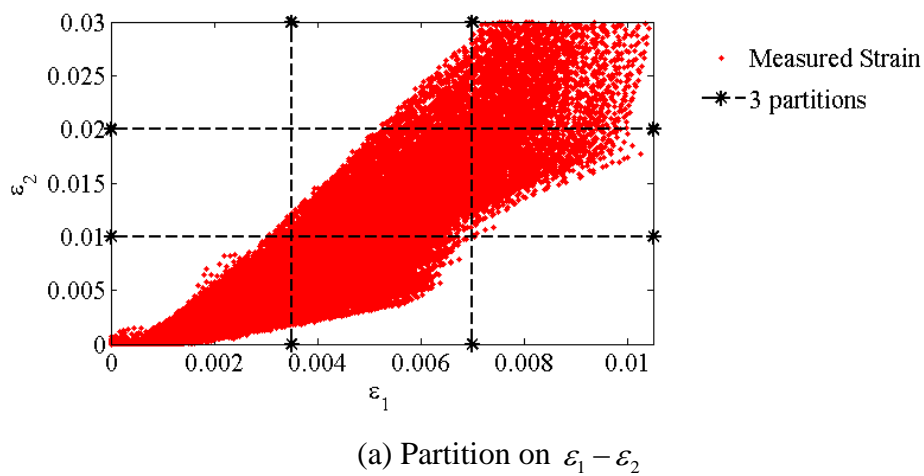


Figure 48 Full-field strain measurements after 190 measurements in Experiment 2.

To demonstrate the concept of the proposed framework, the measured strain values were divided to 3 partitions, as shown in Figures 49(a) and (b), with the incremental partition values listed in Table 31.

Table 31 Incremental partition values used for Example 2.

Incremental Partition	Value
$\Delta\check{\varepsilon}_1$	3.50×10^{-3}
$\Delta\check{\varepsilon}_2$	1.00×10^{-2}
$\Delta\check{\varepsilon}_6$	3.00×10^{-3}



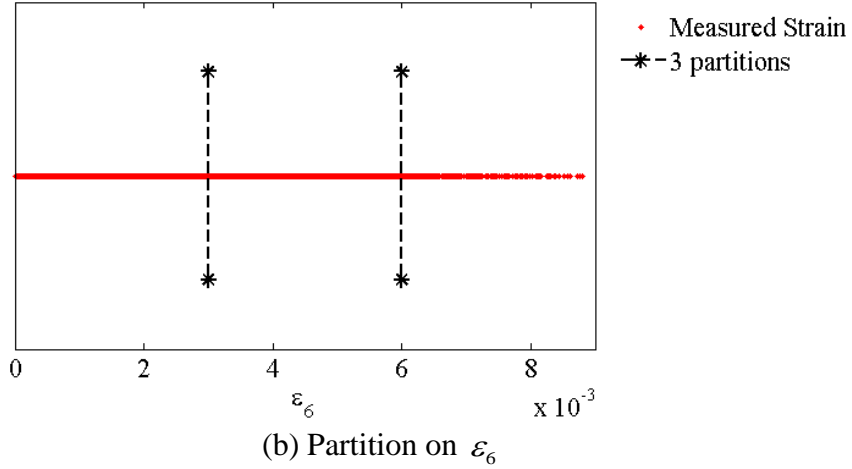


Figure 49 Number of partitions in Experiment 2.

Table 32 lists the prior knowledge of the means used in the stochastic multi-linear characterization method. Since the knowledge about multi-linear coefficients is not known, the prior knowledge of means applies 1.5 times the known elastic constants listed in Table 24. Table 32 also lists the prior knowledge of variance that is used by the multi-linear characterization method. Since limited information is known about the exact multi-linear coefficients, the empirical knowledge used in this experiment was set to large values $P_g^k = 7 \times 10^{-4}$ and $P_w^k = 1.5 \times 10^3$.

Table 32 Prior knowledge of means used in Experiment 2, where $n_p=3$.

Prior Knowledge on Means	Value	Prior Knowledge on Variance	Value
$q_{11}^{0 0}$	$[1,1,1] \times 1.5 q_{11}^*$	$[P_{(1,1)}^{0 0} \dots P_{(n_p, n_p)}^{0 0}]$	$[0.05, 1.2, 8] \times 10^8$
$q_{22}^{0 0}$	$[1,1,1] \times 1.5 q_{22}^*$	$[P_{(n_p+1, n_p+1)}^{0 0} \dots P_{(2n_p, 2n_p)}^{0 0}]$	$[0.08, 0.4, 3] \times 10^7$
$q_{12}^{0 0}$	$[1,1,1] \times 1.5 q_{12}^*$	$[P_{(2n_p+1, 2n_p+1)}^{0 0} \dots P_{(3n_p, 3n_p)}^{0 0}]$	$[0.2, 3, 4] \times 10^7$
$q_{66}^{0 0}$	$[1,1,1] \times 1.5 q_{66}^*$	$[P_{(3n_p+1, 3n_p+1)}^{0 0} \dots P_{(4n_p, 4n_p)}^{0 0}]$	$[0.12, 0.7, 1.3] \times 10^6$

Figure 50 shows the comparison between the estimated stress-strain of the results between the proposed framework and the reference values of a 2017-T451 aluminum alloy, which can be found in [136]. It is shown that the discrepancy of the proposed framework increases when the specimen starts to yield. The current three partitions numbers may not be sufficient to describe the transition between the elastic and inelastic region. It is shown that the second linear partition

approximated the yield point by averaging the transitional behavior. This indicates the importance of choosing the suitable number of partitions for representing the nonlinear behavior of the material. The selection of number of partitions will be discussed as part of the future work of this dissertation.

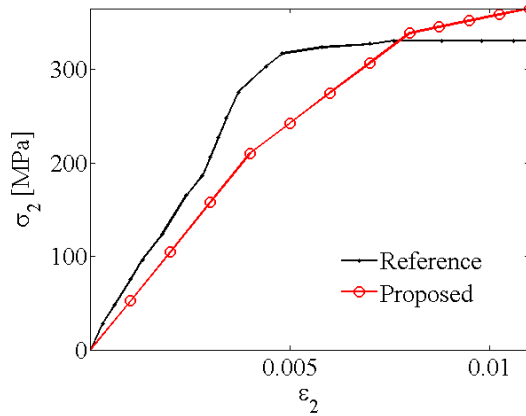


Figure 50 Comparison of the estimated and referenced [136] tensile stress-strain relations.

Figures 51(a)-(c) show the multi-linear stress-strain relations estimated by the stochastic multi-linear characterization method, after 190 measurements. The known linear stress-strain relations are used here as references for the estimated model. It is shown that linear stress-strain relations were well estimated by the proposed framework. Table 33 lists the final estimates of the proposed framework after 190 measurements. Figures 51(a) and (b) show that the estimated relations of $\sigma_1 - \varepsilon_1$ and the ones of $\sigma_2 - \varepsilon_1$ is different by 1.5 times. This is also reflected in Table 33, where the estimated coefficients \mathbf{q}_{11} and \mathbf{q}_{22} are generally 1.5 times different than each other. Since the material specimen is isotropic, it is found that the difference between \mathbf{q}_{11} and \mathbf{q}_{22} is contributed by amount of information exhibited in the loading. In this tensile test, the lack of transverse strain information has contributed to 22% difference of the first partition of q_{11} from the known value. The difference of the first partition q_{22} , i.e. 9%, is lesser since more tensile information is exhibited in the test. This can be improved if an optimal design of the specimen that maximizes both information is used in the test. Alternatively, the same square specimen can be loaded in an optimal path that maximizes both tensile and transverse information in measurements. The results additionally show the strain regions where yielding starts to occur in the mate-

rial. In general, the good agreement of linear stress-strain relations and the decreasing estimated multi-linear coefficients has qualitatively demonstrated an initial validation, and application of the proposed on-line nonlinear framework to the nonlinear characterization problem.

Table 33 Final estimates after 190 measurements (Experiment 2).

Estimated Coefficients	Value
$\mathbf{q}_{11} = [{}^1q_{11}, {}^2q_{11}, {}^3q_{11}]$	$[52.65, 32.12, 8.79] \times 10^3 \text{ MPa}$
$\mathbf{q}_{22} = [{}^1q_{22}, {}^2q_{22}, {}^3q_{22}]$	$[77.64, 55.97, 1.83] \times 10^3 \text{ MPa}$
$\mathbf{q}_{12} = [{}^1q_{12}, {}^2q_{12}, {}^3q_{12}]$	$[25.76, 15.35, 6.31] \times 10^3 \text{ MPa}$
$\mathbf{q}_{66} = [{}^1q_{66}, {}^2q_{66}, {}^3q_{66}]$	$[24.76, 12.90, 1.04] \times 10^3 \text{ MPa}$

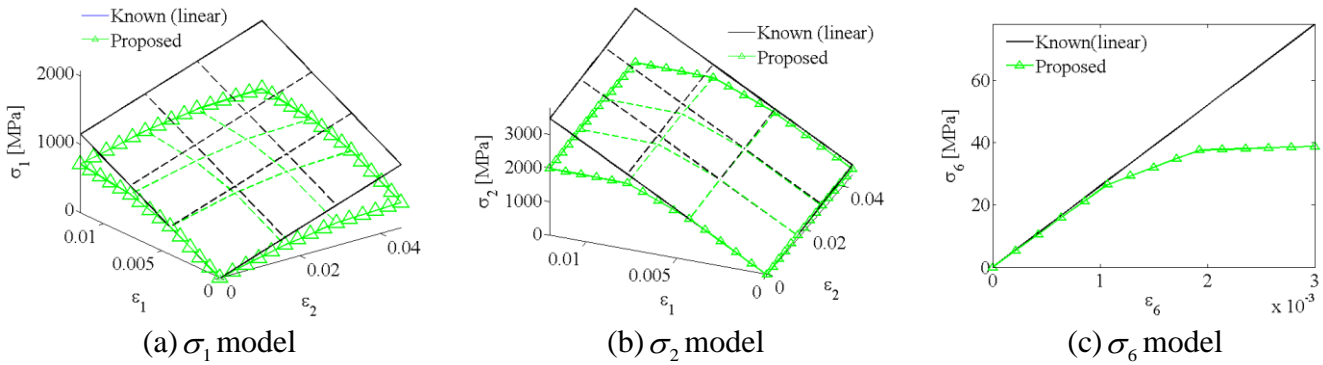


Figure 51 Multi-linear model estimated by the proposed framework (Experiment 2).

7.3 Summary

Experimental studies of the proposed framework have been performed to solve the linear and nonlinear characterization problems. Detailed experimental procedures, including the experimental system, that are used to evaluate the proposed framework have been presented in this Chapter.

The first experimental study demonstrates the applicability of stochastic linear characterization method to characterizing multi-axial stress-strain relations of aluminum specimen. Although isotropic materials are only governed by two elastic moduli, four elastic constants were used in the studies to resemble the characterization of anisotropic materials using energy-based characterization formulations. Specimens of three different geometries and shapes were investigated via three tensile tests using non-contact full-field measurements through developed modules. It was

found that the proposed framework effectively identified all four elastic constants in all tests, at every measurement. Based on the estimated constants, the proposed framework could estimate Young's modulus and Poisson's ratio, which are within 1.63% and 5.25% error from the known values, respectively. The performance of the proposed framework based on different camera resolution was also investigated based on the experimental data obtained from an ongoing work [141]. The accuracy of the proposed framework, with the advancement of digital camera technology, has shown the potential of the proposed framework in achieving accuracies that are comparable to the contemporary characterization methods that employ contact sensors. The final experimental study applied the proposed on-line stochastic framework to characterizing the aluminum specimen up to the nonlinear region. Experimental results have further confirmed the applicability of the proposed framework to the nonlinear characterization of anisotropic materials.

Chapter 8

Conclusions and Future Work

The conclusions of this dissertation are presented in this Chapter. This Chapter begins with a summary of the contributions and a discussion of the proposed on-line nonlinear characterization framework based on the numerical and experimental studies presented in Chapters 4 to 7. This is followed by suggestions for potential future work, and ends with closing remarks.

8.1 Conclusions

The proposed on-line nonlinear characterization framework, which is comprised of the stochastic linear and multi-linear characterization methods, has successfully achieved the objective stated at the beginning of this dissertation. The formulations of linear and multi-linear characterization problems have been shown to model the stress-strain relations of anisotropic materials up to the nonlinear region. The recursive mechanisms of the proposed framework in the measurement update process have been shown to enable the on-line characterization capability of the proposed framework. The derivation of stochastic equations from energy-based characterization formulations additionally showed its noise removing capability when handling noisy measurements. The Kalman gain, which is newly derived from the stochastic equations, has demonstrated its capability to achieve optimal characterization through variance minimization. The derivation of a multi-camera data fusion technique has further shown the improvement of full-field measurements in terms of certainty through the product of Gaussian distributions and a propagation of uncertainties method.

Numerical studies have demonstrated that the stochastic linear characterization method considerably minimizes the effect of noise by estimating elastic constants that are more accurate

than the ones computed by the conventional deterministic approach. Results show that the derivation of a new Kalman gain reduces the variances towards zero and results in the effective stochastic estimation of converging elastic constants. It was discovered that incorrect prior knowledge would result in slower convergence of the characterization results. The linear characterization method has also shown robustness to uncertainties in prior knowledge and ranges of measurement noise. The variances computed in the numerical studies were found to describe not only the certainty of estimation results but also the convergence rate of the characterization. The stochastic linear characterization method was finally applied to a composite specimen consisting of a cross-ply AS4/3506-1 composite laminate. Despite converging to the exact solution, the fluctuation of means was found to be attributed by the effect of randomness existing in the material characterization.

The stochastic multi-linear characterization method was applied to the characterization of an AS4D/9310 graphite epoxy laminate model, and was demonstrated successfully in characterizing the nonlinear properties of anisotropic materials on-line, under the influence of measurement noise. The numerical examples were performed by assuming good knowledge on the measurement covariance. This has enabled a good convergence of results at the initial steps. The mean and covariance of each coefficient were identified instantly when strain values were measured in a new partition. Parametric studies of the differential entropy show that the multi-linear characterization method is robust to the change of noise while maintaining the certainty of the results.

The multi-camera data fusion technique addresses this issue, providing more robust results through less noisy measurements as applied with the stochastic linear characterization method. The parametric studies have shown that the data fusion technique refines the measurements by estimating their means that are weighted by the covariance of each camera sensor. The probabilistic model is found to reliably represent the uncertainties propagated from the sensor covariance. Studies have validated that the product of probabilistic measurements yields the fused measurements that are more informative than the original measurements.

Experimental studies first demonstrated the on-line capability of the proposed framework in characterizing the elastic properties of isotropic materials of different geometries. While this particular material is well studied for its nonlinear behavior, the same material specimen was ap-

plied to the multi-linear characterization method. It was found that the proposed framework identifies elastic constants that are in good agreement with known values irrespective of the specimen geometry. Parametric study of the linear characterization method has demonstrated the limitation of the proposed framework with respect to the current camera technology. The results of the multi-linear characterization method were then compared to the known nonlinear stress-strain relations and found that at the expense of accuracy, the proposed framework is still capable of characterizing the nonlinear behavior on-line in a single test.

In this dissertation, a novel on-line nonlinear characterization framework that stochastically characterizes the behavior of anisotropic materials has been presented. However, the accuracy of the proposed framework is highly dependent on the image sensor resolution. The current resolution may not achieve the same accuracy as what the contact sensors can achieve. Such a situation can be improved through the rapid advancement of camera technology. The on-line nonlinear framework was developed and both numerically and experimentally studied, indicating that the objective has been achieved. At the expense of accuracy, it is concluded that the proposed framework can be very efficient in characterizing the nonlinear behavior of anisotropic materials on-line.

8.2 Future Work

One possible future extension of the proposed framework is the use of a non-Gaussian estimator as the measurement noise may not be well approximated as Gaussian under some experimental conditions. The actual uncertainty embedded inside the experimental data has yet to be investigated and would potentially require the proposed framework to be integrated with additional stochastic numerical techniques to deal with experimental data suffering from high signal noise. The multi-camera data fusion technique is the first step of the scalable sensors network to characterize anisotropic materials and can be extended in a variety of ways. The current formulation can be extended to handle out-of-plane deformation of structures. One indispensable step is the arrangement of field of views between multiple cameras, which allows the proposed technique to be usable and useful to the full-field monitoring of large structure at multi-resolution level.

The multi-linear characterization method is the first step to solve for the nonlinear characterization problem of anisotropic materials. The current method has been simplified by assuming that the materials are rate-, temperature- and path- independent. More complex nonlinear behavior that is rate-, temperature-, and/or path- dependent will be described in combination with the other work of colleagues [134, 135]. Energy loss is inevitable in most of the deforming process. It is also important to include energy from other physical fields, such as thermal and electrical energy, in the proposed framework to be robust under different environmental conditions.

Despite numerical studies that have been performed on anisotropic materials, the experimental studies will be extended to the application of composite specimens once they become available to the author. Currently, the proposed framework is being implemented onto uniaxial and multi-axial testing machines available to the author's group for the characterization of actual materials [107, 108]. Any extension from the proposed framework will be validated experimentally by the machines.

8.3 Closing remarks

The interest in employing high performance materials for different engineering applications has been increasingly prolific in our community, owing primarily to their customizable directional properties introduced by their anisotropic makeup. The ongoing research certainly yields new and fast insights into material behaviors and further contributes to the development of new types. Along with the foreseeable outcome in the near future, the works presented here provide alternative methods for estimating material constitutive behavior in an efficient and robust manner.

With the advancement of camera technology, the proposed framework has the potential to achieve the accuracy of the current conventional testing methods. The difference is that the proposed framework will be capable of characterizing nonlinear behavior of anisotropic materials on-line without cutting any specimen on the structures and testing specimens in the laboratory. The fast characterization technology will provide a new platform to characterize the complex behavior of new materials efficiently, and further prepare ourselves to embrace the next significant finding of unknown materials and towards a new era of materials.

Bibliography

- [1] Daniel IM and Ishai O. *Engineering mechanics of composite materials*, Oxford University Press, New York, 2006.
- [2] Lauwagie T. Vibration-based methods for the identification of the elastic properties of layered materials. *Doctoral Thesis* 2005; Katholieke Universiteit Leuven.
- [3] Erwins DJ. *Modal Testing: Theory, Practice and Application*, Wiley, 2001.
- [4] Rao SS. *Mechanical Vibrations*, Prentice Hall, 4th Ed., 2003.
- [5] Zimmerman AT, Shiraishi M, Swartz RA, Lynch JP. Automated modal parameter estimation by parallel processing within wireless monitoring systems, *Journal of Infrastructure System* 2008; **14**: 102-113.
- [6] Gibson RF. Modal vibration response measurements for characterization of composite materials and structures, *Composites Science and Technology* 2000; **60**: 2769-2780.
- [7] Zhuang Li, Vibration and acoustical properties of sandwich composite materials, *PhD Dissertation*, Auburn University, 2006.
- [8] Alfano M, Pagnotta L. Determining the elastic constants of isotropic materials by modal vibration testing of rectangular thin plates, *Journal of Sound and Vibration* 2006; **293**: 426-439.
- [9] ASTM. Standard Test Method for Tensile Properties of Polymer Matrix Composite Materials, *ASTM Standard* 2008; ASTM D3039 / D3039M-08.
- [10]ASTM. Standard test method for in-plane shear properties of polymer matrix composite materials by the rail shear method, *ASTM Standard* 2001; D4255/D4255m-01.
- [11]ISO. Test conditions for unidirectional fibre-reinforced plastic composites, *ISO Standard* 2009; 527-5:2009.
- [12]ASTM. Standard test method for in-plane shear response of polymer matrix composite materials by tensile test of a $\pm 45^\circ$ laminate, *ASTM Standard* 2007; D3518/D3518M-94.
- [13]ASTM. Standard test method for shear properties of composite materials by the V-notched beam method, *ASTM Standard* 2005; D5379/D5379M-05.
- [14]ASTM. Standard Test Method for Shear Modulus of Wood-Based Structural Panels, *ASTM Standard* 2006; D3044-94.
- [15] Hwang SF, Chang CS, Determination of elastic constants of materials by vibration testing, *Composite Structures* 2000; **49**: 183-190.
- [16] De Silva CW. Vibration and shock handbook, CRC Press, 2005.

- [17] Yang S, Gibson RF, Crosbie GM. Vibration characteristics and comparisons of automotive engine valves made from conventional and non-conventional materials, *Journal of Sound and Vibration* 1996; **191**: 986-992.
- [18] Cheng SH, Hwu Chyanbin, On-line measurement of material properties for composite wing structures, *Composites Science and Technology* 2006; **66**: 1001-1009.
- [19] Inman DJ, "Vibration with Control", Wiley 2006.
- [20] Lauwagie T, Sol H, Heylen W. Handling uncertainties in mixed numerical-experimental techniques for vibration based material identification, *Journal of Sound and Vibration* 2006; **291**: 723-739.
- [21] Araújo AL, Mota Soares CM, Moreira de Freitas MJ, Pedersen P, Herskovits J. Combined numerical-experimental model for the identification of mechanical properties of laminated structures, *Composite Structures* 2000; **50**: 363-372.
- [22] ASTM Standard. Standard Test Method for Dynamic Young's Modulus, Shear Modulus, and Poisson's Ratio by Impulse Excitation of Vibration, *Book of Standards* 2001; E1876-01.
- [23] ASTM Standard. Standard Test Method for Dynamic Young's Modulus, Shear Modulus, and Poisson's Ratio by Sonic Resonance, *Book of Standards* 2001; E1875-00e1.
- [24] Zhang C, Lessard LB, Nemes JA. A closed-form solution for stresses at curved free edges in composite laminates: A variational approach, *Composites Science and Technology* 1997; **57**: 1341-1354.
- [25] Ip KH, Tse PC, Lai TC. Material characterization for orthotropic shells using modal analysis and Rayleigh-Ritz models, *Composites Part B* 1998; **29**: 397-409.
- [26] Subramanian P. Dynamic analysis of laminated composite beams using higher order theories and finite elements, *Composite Structures* 2006; **73**: 342-353.
- [27] Kang SW, Lee JM. Application of free vibration analysis of membranes using the non-dimensional dynamic influence function, *Journal of Sound and Vibration* 1999; **234**: 455-470.
- [28] Hwang W, Han KS. Finite element analyses of specific damping capacity and undamped/damped forced motion of composite plate using modified 16-node solid elements, *Key Engineering Materials* 2000; **183**: 469-474.
- [29] Kang SW, Lee JM. Free vibration analysis of arbitrarily shaped plates with clamped edges using wave-type functions, *Journal of Sound and Vibration* 2000; **242**: 9-26.
- [30] Basar Y, Omurtag MH. Free-vibration analysis of thin/thick laminated structures by layer-wise shell models, *Computers & Structures* 2000; **74**: 409-427.
- [31] Kuttenkeuler J. A finite element based modal method for determination of plate stiffnesses considering uncertainties, *Journal of Composite Materials* 1999; **33**: 695-711.

- [32] Pasa Dutra VF, Maghous S, Campos Filho A, Pacheco AR. A micromechanical approach to elastic and viscoelastic properties of fiber reinforced concrete 2010; **40**: 460-472.
- [33] Searcy CR. A multiscale model for predicting damage evolution in heterogeneous viscoelastic media 2004; PhD Dissertation, Texas A&M University.
- [34] Schapery RA, nonlinear viscoelastic and viscoplastic constitutive equations based on thermodynamics, *Mechanics of Time-dependent Materials* 1997; **1**: 209-240.
- [35] Papanicolaou GC, Zaoutsos SP, Cardon AH. Prediction of the non-linear viscoelastic response of unidirectional fiber composites, *Composites Sciences and Technology* 1999; **59**: 1311-1319.
- [36] Jiang Z, Han J, Liu X, Dynamic Compressive Response and Failure Behavior of CFRP Composites at High Strain Rates, *Advanced Materials Research* 2010; **152**: 988.
- [37] Melo JDD, Radford DW. Viscoelastic characterization of transversely isotropic composite laminae, *Journal of Composite Materials* 2003; **37**: 129-145.
- [38] Khaled AT, Weltsman YJ. A strain-based formulation for the coupled viscoelastic/Damage behavior, *Journal of Applied Mechanics* 2001; **68**: 304-311.
- [39] Horstemeyer MF, Bamman DJ. Historical review of internal state variable theory for inelasticity, *International Journal of Plasticity* 2010; **26**: 1310-1334.
- [40] Lonetti P, Zinno R, Greco F, Barbero EJ. Interlaminar damage model for polymer matrix composites, *Journal of Composite Materials* 2003; **37**: 1485-1504.
- [41] Kumar RS, Talreja R. A continuum damage model for linear viscoelastic composite materials, *Mechanics of Materials* 2003; **35**: 463-480.
- [42] Petit PH and Waddoups ME, A method of predicting the nonlinear behavior of laminated composites, *Journal of Composite Materials* 1969; **3**: 2-19.
- [43] Blaiszik BJ, Baginska M, White SR, Sottos NR. Autonomic recovery of fiber/matrix interfacial bond strength in a model composite, *Advanced Functional Materials* 2010; **20**: 3547-3554.
- [44] BS. Methods of testing plastics, glass reinforced plastics and measurement of hardness by means of a Barcol impressor, *BS Standard* 1977; BS2182-10.
- [45] Curtis PT. CRAG test methods for the measurement of the engineering properties of fibre reinforced plastics, *Royal Aerospace Establishment Technical Report 88 012*, New Farnborough 1988.
- [46] Tairova LP, Tsvetkov SV. Specific features of strain measurement in composite materials, *Mechanics of Composite Materials* 1993; **28**: 489-493.
- [47] Wu CT. Transverse sensitivity of bonded strain gages, *Experimental Mechanics* 1962; **2**: 338-344.

- [48] Hassan YE, Machi KE. Transverse sensitivity errors in rectangular rosettes, *Strain* 1978; **14**: 47-51.
- [49] Vishay Micro-Measurements. Errors due to transverse sensitivity in strain gages, *Tech Note* 2007; **TN-509**: 91-99.
- [50] Hahn HT, Tsai SW. Nonlinear elastic behavior of unidirectional composite laminae, *Composite Materials* 1973; **7**: 102-118.
- [51] Hahn HT, Tsai SW. Nonlinear behavior of laminated composites, *Composite Materials* 1973; **7**: 257-271.
- [52] Nuismer RJ, Whitney JM. Uniaxial failure of composite laminates containing stress concentrations, *ASTM special technical publication* 1975; **593**: 117-142.
- [53] Chib A. Parametric study of low velocity impact analysis on composite tubes, *MS Thesis*, Wichita State University, 2006.
- [54] Lim WK, Jeong WK. Failure of fibrous anisotropic materials under combined loading, *Composites Part B: Engineering* 2010; **41**: 94-97.
- [55] Maimi P, Mayugo JA, Camanho PP. A three-dimensional damage model for transversely isotropic composite laminates, *Composite Materials* 2008; **42**: 2717-2745.
- [56] Sun CT, Chen JL. A micromechanical model for plastic behavior of fibrous composites, *Composites Science and Technology* 1991; **40**, 115–129.
- [57] Sun CT, Chen JL, Sha GT, Koop WE. An investigation of the mechanical behavior of SCS-6/Ti-6-4 metal-matrix composite at elevated temperatures, *Composites Science and Technology* 1993; **49**, 183–190.
- [58] Wang C, Sun CT. Experimental characterization of constitutive models for PEEK thermoplastic composite at heating stage during forming, *Journal of Composite Materials* 1997; **31**, 1480–1506.
- [59] Chevalier L, Calloch S, Hild F, Marco Y. Digital image correlation used to analyze the multiaxial behavior of rubber-like materials, *European Journal of Mechanics - A/Solids* 2001; **20**: 169-187.
- [60] Lopez-Anido R, El-Chiti F, Muszynski L, Dagher H, Thompson L, Hess, P. Composite material testing using a 3-D digital image correlation system, *Composites 2004, American Composites Manufacturers Association*, Tampa, Florida, 7pp.
- [61] Tuttle ME, Brinson HF. Resistance-foil strain-gage technology as applied to composite materials, *Experimental Mechanics* 1984; **24**: 54-65.
- [62] Ajovalasit A. Advances in strain gauge measurement on composite materials, *Strain* 2010; DOI: 10.1111/j.1475-1305.2009.00691.x.

- [63] Milani AS, Nemes JA, Abeyaratne RC, Holzapfel GA. A method for the approximation of non-uniform fiber misalignment in textile composites using picture frame test, *Composites Part A: Applied Science and Manufacturing* 2007; **38**: 1493-1501.
- [64] Pieczyska EA, Pecherski RB, Gadaj SP. Experimental and theoretical investigations of glass-fibre reinforced composite subjected to uniaxial compression for a wide spectrum of strain rates, *Arch. Mech.* 2005; **58**: 273-291.
- [65] Pandita SD, Nishiyabu K, Verpoest I. Strain concentrations in woven fabric composites with holes, *Composite Structures* 2003; **59**: 361-368.
- [66] Lomov SV, Willems A, Barburski M, Stoilova TZ, Verpoest I, Zhu Y. Picture frame test of woven composite reinforcements with a full-field strain registration, *Textile Research Journal* 2006; **76**: 243-252.
- [67] Kim JH, Pierron F, Grédias M, Wisnom MR. A procedure for producing reflective coatings on plates to be used for full-field slope measurements by a deflectometry technique, *Strain* 2007; **43**: 138-144.
- [68] Andrianopoulos NP. Full-field displacement measurement of a speckle grid by using a mesh-free deformation function, *Strain* 2006; **42**: 265-271.
- [69] Zhang L, Huang Y, Chen JY, Hwang KC. The mode III full-field solution in elastic materials with strain gradient effects, *International Journal of Fracture* 1998; **92**: 325-348.
- [70] Sutton MA, Turner JL, Bruck HA, Chae TA. Full-field representation of discretely sampled surface deformation for displacement and strain analysis, *Experimental Mechanics* 1991; **31**: 168-177.
- [71] Weissman EM, Post D. Full-field displacement and strain rosettes by moiré interferometry, *Experimental Mechanics* 1982; **22**: 324-328.
- [72] Michopoulos JG, Iliopoulos AP. A computational workbench for remote full field 2d displacement and strain measurements, *Proceedings of the ASME 2009 International Design Engineering Technical Conferences & Computers and Information in Engineering Conference IDETC/CIE 2009*; San Diego, USA, Paper ID: DETC2009/CIE-86900, 9pp.
- [73] Pan B, Asundi A, Xue H, Gao J. Digital image correlation using iterative least squares and pointwise least squares for displacement field and strain field measurements, *Optics and Lasers in Engineering* 2009; **47**: 865-874.
- [74] Tong W. An evaluation of digital image correlation criteria for strain mapping applications, *Strain* 2005; **41**: 167-175.
- [75] Zhou P, Goodson KE. Subpixel displacement and deformation gradient measurement using digital image/speckle correlation, *Optical Engineering* 2001; **40**: 1613-1620.

- [76] Liu XY, Tan QC, Li RL. Study on digital image correlation using artificial neural networks for subpixel displacement measurement, Book chapter in: *Advances in Neural Network Research and Applications* 2010; **67**: 405-412.
- [77] Wang YH, Jiang JH, Wanintrudal C, Du C, Zhou D, Smith LM, Yang LX. Whole field sheet metal tensile test using digital image correlation, *Experimental Techniques* 2009; **34**: 54-59.
- [78] Orteu J, Rotrou Y, Sentenac T, Robert L. An innovative method for 3-D shape, strain and temperature full-field measurement using a single type of camera: principle and preliminary results, *Experimental Mechanics* 2008; **48**: 163-179.
- [79] Wang ZY, Li HQ, Tong JW, Shen M, Aymerich F, Priolo P. Dual magnification digital image correlation based strain measurement in CFRP laminates with open hole, *Composites Science and Technology* 2008; **68**: 1975-1980.
- [80] Sutton MA, Wolters WJ, Peters WH, Ranson WF, McNeill SR. Determination of displacements using an improved digital correlation method, *Image and Vision Computing* 1983; **1**: 133-139.
- [81] Barone S, Berghini M, Bertini L. Grid pattern for in-plane strain measurements by digital image processing, *The Journal of Strain Analysis for Engineering Design* 2001; **36**: 51-59.
- [82] Wang Z, Cárdenas-García JF, Han B. Inverse method to determine elastic constants using a circular disk and moiré interferometry, *Experimental Mechanics* 2006; **45**: 27-34.
- [83] Grédiac M. Stress analysis and identification with full-field measurements, *Advances in Experimental Mechanics IV* 2005; **3-4**: 9-14.
- [84] Avril S, Pierron F, Yan J, Sutton M.A. Identification of viscoplastic parameters and characterization of Lüders behaviour using Digital Image Correlation and the Virtual Fields Method, *Mechanics of Materials* 2008; **40**: 729-742.
- [85] Grédiac M, Pierron F. Applying the Virtual Fields Method to the identification of elasto-plastic constitutive parameters, *International Journal of Plasticity* 2006; **22**: 602-627.
- [86] Chalal H, Avril S, Pierron F, Meraghni F. Experimental identification of a nonlinear model for composites using the grid technique coupled to the virtual fields method, *Composites Part A: Applied Science and Manufacturing* 2006; **37**: 315-325.
- [87] Giraudeau A, Guo B, Pierron F. Stiffness and damping identification from full field measurements on vibrating plates. *Experimental Mechanics* 2006; **46**: 777-787.
- [88] Promma N, Raka B, Grédiac M, Toussaint E, Le Cam JB, Balandraud X, Hild F. Application of the virtual fields method to mechanical characterization of elastomeric materials, *International Journal of Solids and Structures* 2009; **46**: 698-715.
- [89] Chalal H, Meraghni F, Pierron F, Grédiac M. Direct identification of the damage behaviour of composite materials using the virtual fields method, *Composites Part A: Applied Science and Manufacturing* 2004; **35**: 841-848.

- [90] Avril S, Pierron F. General framework for the identification of constitutive parameters from full-field measurements in linear elasticity, *International Journal of Solids and Structures* 2007; **44**: 4978-5002.
- [91] Pagnotta L, Stigliano G. Elastic characterization of isotropic plates of any shape via dynamic tests: Practical aspects and experimental applications, *Mechanics Research Communications* 2009; **36**: 154-161.
- [92] Pagnacco E, Moreau A, Lemosse D. Inverse strategies for the identification of elastic and viscoelastic material parameters using full-field measurements,
- [93] Claire D, Hild F, Roux S. A finite element formulation to identify damage fields: the equilibrium gap method, *International Journal for Numerical Methods in Engineering* 2004; **61**: 189-208.
- [94] Farhat C, Hemez F. Updating finite element dynamics models using an element-by-element sensitivity methodology, *AIAA* 1993; **31**: 1702-1711.
- [95] Pagnacco E, Moreau A, Lemosse D. Inverse strategies for the identification of elastic and viscoelastic material parameters using full-field measurements, *Materials Science and Engineering: A* 2007; **452-453**: 737-745.
- [96] Allemand RJ. Investigation of some multiple input/output frequency response function experimental modal analysis techniques, PhD thesis, *University of Cincinnati* 1980.
- [97] Bui H, Constantinescu A, Maigre H. Numerical identification of linear cracks in 2d elastodynamics using the instantaneous reciprocity gap, *Inverse Problems* 2004; **20**: 993-1001.
- [98] Pagnacco E, Lemosse D. A coupled FE based inverse strategy from displacement field measurement subject to an unknown distribution of forces, *Photomechanics* 2006; Clermont-Ferrand, 10-12 July 2006.
- [99] Bruno L, Furgiuele FM, Pagnotta L, Poggialini A. A full-field approach for the elastic characterization of anisotropic materials, *Optics and Lasers in Engineering* 2002; **37**: 417-431.
- [100] Bruno L, Felice G, Pagnotta L, Poggialini A, Stigliano G. Elastic characterization of orthotropic plates of any shape via static testing, *International Journal of Solids and Structures* 2008; **45**: 908-920.
- [101] Lecompte D, Smits A, Sol H, Vantomme J, Hemelrijck DV. Mixed numerical-experimental technique for orthotropic parameter identification using biaxial tensile tests on cruciform specimens. *International Journal of Solids and Structures* 2007; **44**: 1643-1656.
- [102] Ienny P, Caro-Bretelle A, Pagnacco E. Identification from measurements of mechanical fields by finite element model updating strategies: A review, *European Journal of Computational Mechanics* 2009; **18**: 353-376.
- [103] Molimard J, Le Riche R, Vautrin A, Lee JR. Identification of the four orthotropic plate stiffnesses using a single open-hole tensile test, *Experimental Mechanics* 2005; **45**: 404-411.

- [104] Florentin E, Lubineau G. Identification of the parameters of an elastic material model using the constitutive equation gap method, *Computational Mechanics* 2010; DOI: 10.1007/s00466-010-0496-y, 11pp.
- [105] Gouttebroze C, Louf F, Champaney L. Multiple model updating using the finite element method over a polynomial algebra, *Inverse Problems* 2010; **26**: 13pp.
- [106] Beluch W. Evolutionary identification of material constants in composites, *Mechanics of Advanced Materials and Structures* 2007; **14**: 677-686.
- [107] Furukawa T, Michopoulos JG. Online planning of multiaxial loading path for elastic material identification, *Computer Methods in Applied Mechanics and Engineering* 2008; **197**: 885-901.
- [108] Furukawa T, Michopoulos JG. Computational design of multiaxial tests for anisotropic material characterization, *International Journal for Numerical Methods in Engineering* 2007; **74**: 1872-1895.
- [109] Furukawa T, Michopoulos JG, Kelly DW. Elastic characterization of laminated composites based on multiaxial tests, *Composite Structures* 2008; **86**: 269-278.
- [110] Mast PW, Nash GE, Michopoulos JG, Thomas R, Badaliance R, Wolock I. Characterization of strain-induced damage in composites based on the dissipated energy density part I. Basic scheme and formulation, *Theoretical and Applied Fracture Mechanics* 1995; **22**: 71-96.
- [111] Mast PW, Nash GE, Michopoulos JG, Thomas R, Badaliance R, Wolock I. Characterization of strain-induced damage in composites based on the dissipated energy density part II. Composite specimens and naval structures, *Theoretical and Applied Fracture Mechanics* 1995; **22**: 97-114.
- [112] Mast PW, Nash GE, Michopoulos JG, Thomas R, Badaliance R, Wolock I. Characterization of strain-induced damage in composites based on the dissipated energy density Part III. General material constitutive relation, *Theoretical and Applied Fracture Mechanics* 1995; **22**: 115-125.
- [113] Nishioka T, Kurio K, Nakabayashi H. An intelligent hybrid method to automatically detect and eliminate experimental measurement errors for linear elastic deformation fields, *Experimental Mechanics* 2000; **40**: 170-179.
- [114] Réthoré J, A fully integrated noise robust strategy for the identification of constitutive laws from digital images, *International Journal for Numerical Methods in Engineering* 2010; ID: 10.1002/nme.2908, 30pp.
- [115] Lal S, Chandra M, Upadhyay GK. Noise removal algorithm for images corrupted by additive gaussian noise, *International Journal of Recent Trends in Engineering* 2009; **2**: 199-206.

- [116] Avril S, Grédiac M, Pierron F. Sensitivity of the virtual fields method to noisy data, *Computational Mechanics* 2004; **34**: 439-452.
- [117] Patterson E, Hack E, Brailly P, Burguete R, Saleem Q, Siebert T, Tomlinson R, Whelan M. Calibration and evaluation of optical systems for full-field strain measurement, *Optics and Lasers in Engineering* 2007; **45**: 550-564.
- [118] Patterson E, Brailly P, Burguete R, Hack E, Siebert T, Whelan M. A challenge for high-performance full-field strain measurement systems, *Strain* 2007; **43**: 167-180.
- [119] Bornert M, Brémand F, Doumalin P, Dupré JC, Fazzini M, Grédiac M, Hild F, Mistou S, Molimard J, Orteu JJ, Robert L, Surrel Y, Vacher P, Watrissé B. Assessment of digital image correlation measurement errors: Methodology and results, *Experimental Mechanics* 2009; **49**: 353-370.
- [120] Yun GJ, Ghaboussi J, Elnashai AS. Self-learning simulation method for inverse nonlinear modeling of cyclic behavior of connections, *Computer methods in applied mechanics and engineering* 2008; **197**: 2836-2857.
- [121] Jung S, Ghaboussi J. Neural network constitutive model for rate-dependent material, *Computers and Structures* 2006; **84**: 955-963.
- [122] Aquino W, Brigham JC. Self-learning finite elements for inverse estimation of thermal constitutive models, *International Journal of Heat and Mass Transfer* 2006; **49**: 2466-2478.
- [123] Liu GR, Han X. Computational inverse techniques in nondestructive evaluation, *CRC Press* 2003.
- [124] Liu GR, Han X, Xu YG, Lam KY. Material characterization of functionally graded material by means of elastic waves and a progressive-learning neural network, *Composites Science and Technology* 2001; **61**: 1401-1411.
- [125] Bhat C, Bhat MR, Murthy CRL. Characterization of failure modes in CFRP composites — An ANN approach, *Journal of Composite Materials* 2008; **42**: 257-276.
- [126] Al-Haika MS, Garmestani H, Savranc A. Explicit and implicit viscoplastic models for polymeric composite, *International Journal of Plasticity* 2004; **20**: 1875-1907.
- [127] Hashash YMA, Jung S, Ghaboussi J. Numerical implementation of a neural network based material model in finite element analysis, *International Journal for Numerical Methods in Engineering* 2004; **59**: 989-1005.
- [128] Ghaboussi J, Pecknold DA, Zhang M, Haj-Ali R. Autoprogressive training of neural network constitutive models, *International Journal for Numerical Methods in Engineering* 1998; **42**: 105-126.
- [129] Pidaparti RMV, Palakal MJ. Material model for composites using neural networks, *AIAA Journal* 1993; **31**: 1533-1535.

- [130] Al-Haik MS, Hussaini MY, Rogan CS. Artificial intelligence techniques in simulation of viscoplasticity of polymeric composites, *Polymer Composites* 2008; **30**: 1701-1708.
- [131] Haj-Ali R, Kim HK. Nonlinear constitutive models for FRP composites using artificial neural networks, *Mechanics of Materials* 2007; **39**: 1035-1042.
- [132] Ghaboussi J. Advances in Neural Networks in Computational Mechanics and Engineering, *Advances of Soft Computing in Engineering* 2010; **512**: 191-236.
- [133] Kessler BS, El-Gizawy AS, Smith DE. Incorporating Neural network material models within finite element analysis for rheological behavior prediction, *Transactions of the ASME* 2007; **129**: 58-65.
- [134] Sul JH, Prusty BG, Pan JW. "A fatigue life prediction model for CSM GRP", *Fatigue & Fracture Engineering Materials & Structures*, 2010; **33**: 513-521.
- [135] Man H, Furukawa T, Pan JW, Iliopoulos AP, Michopoulos JG, Orifici A, Hermanson J, Experimentally validated neural network constitutive modeling using energy-based characterization, *Experimental Mechanics*, under review
- [136] Stress-strain relationships – tensile testing, *Lecture notes of OPTI 222 Mechanical Design in Optical Engineering*, Fall 2008, University of Arizona, 17-23.
- [137] Kassimali A, *Structural Analysis*, 3rd Edition, Thomson, 2004, p.312.
- [138] Zienkiewicz OC, Taylor RL, Zhu JZ, *The Finite Element Methods – Its Basis & Fundamentals*, 6th Edition, Elsevier, 2005, p.36.
- [139] Hartley R, Zisserman A. Multiple view geometry in computer vision, 2nd edn. Cambridge University Press, New York 2003.
- [140] Shannon CE. Prediction and entropy of printed English, *The Bell System Technical Journal* 1951; **30**: 50-64.
- [141] Furukawa T, Cheng JQ, Wada Y. Full-field strain measurements and grey level of accuracy, 2010, in preparation.
- [142] Giaccari P, Dunkel GR, Humbert L, Botsis J, Limberger HG, Salathé RP. On a direct determination of non-uniform internal strain fields using fibre Bragg gratings, *Smart Materials and Structures* 2005; **14**: 127-136.
- [143] Linzell DG. The role of computer models in full-scale bridge laboratory tests, *Computer-Aided Civil and Infrastructure Engineering* 2001; **16**: 431-443.
- [144] Bucher I, Ewins DJ. Modal analysis and testing of rotating structures. *Phil. Trans. R. Soc. Lond. A* 2001; **359**, 61-96.
- [145] Busby HR, Nopporn C, Singh R. Experimental modal analysis of non-linear systems: A feasibility study, *Journal of Sound and Vibration* 1986; **180**: 415-427.

- [146] Worden K, Tomlinson GR. Nonlinearity in experimental modal analysis, *Phil. Trans. R. Soc. Lond. A* 2001; **359**:113-130.
- [147] Hemez F, Doebling S. Review and assessment of model updating for nonlinear, transient dynamics, *Mechanical Systems and Signal Processing* 2000; 45-74.
- [148] Kerschen G, Golinval JC, Vakakis AF, Bergma LA. The method of proper orthogonal decomposition for dynamical characterization and order reduction of mechanical systems: An overview, *Nonlinear Dynamics* 2005; **41**: 147-169.
- [149] Doebling SW, Farrar CR, Prime MB. A summary review of vibration-based damage identification methods, *The Shock and Vibration Digest* 1998; **30**: 91-105.
- [150] Sadeghian P, Rahai AR, Ehsani MR. Effect of fiber orientation on nonlinear behavior of CFRP composites, *Journal of Reinforced Plastics and Composites* 2009; **28**: 2261-2272.
- [151] Tyson J. Optical 3D Deformation and Strain Measurement, In Davies MG, Lumsden AB, Kline WE, Kakadiaris I (Eds.), Pumps and Pipes: Proceedings of the Annual Conference 2011: 147-164, NY: Springer.

Appendix 1

Kalman Filter

A1.1 State Transition Model and Measurement Model

The Kalman filter (KF), also known as the linear quadratic estimator, estimates the state of a dynamical system from a series of noisy measurements. Prior to its operation, the KF requires the construction of two linear probabilistic models with Gaussian noises, which approximate the system behavior; the state transition model and the measurement model. The state transition model, which describes the state of the system at step k from that at step $k-1$, is given by

$$\mathbf{x}^k = \mathbf{A}^{k-1} \mathbf{x}^{k-1} + \mathbf{B}^{k-1} \mathbf{u}^{k-1} + \mathbf{w}^{k-1} \quad (\text{A1.1})$$

where \mathbf{x}^{k-1} and \mathbf{u}^{k-1} are the state and the control input of the system, respectively, \mathbf{A}^{k-1} and \mathbf{B}^{k-1} are the system and the input matrices, respectively and \mathbf{w}^{k-1} is a process noise given by a normal distribution, i.e. $\mathbf{w}^{k-1} \sim N(\mathbf{0}, \mathbf{S}_w^{k-1})$. The measurement model describes the measured data \mathbf{z}^k with respect to the true state \mathbf{x}^k and is given by

$$\mathbf{z}^k = \mathbf{C}^k \mathbf{x}^k + \mathbf{v}^k \quad (\text{A1.2})$$

where \mathbf{C}^k is the output matrix and the measurement noise also follows a normal distribution, $\mathbf{v}^k \sim N(\mathbf{0}, \mathbf{S}_v^k)$. Having the models established, the KF recursively carries out two processes, prediction and correction, to update the estimation of the state.

A1.2 Prediction

The prediction updates the estimation in time by predicting the mean and the covariance of the elastic constants at step k , $\mathbf{x}^{k|k-1}$ and $\mathbf{S}^{k|k-1}$, from those estimated at time $k-1$, $\mathbf{x}^{k-1|k-1}$ and $\mathbf{S}^{k-1|k-1}$. Through the substitution of Equation (A1.1), the state expected at step k is given by

$$\begin{aligned} E\langle \mathbf{x}^k \rangle &:= E\langle \mathbf{A}^{k-1}\mathbf{x}^{k-1} + \mathbf{B}^{k-1}\mathbf{u}^{k-1} + \mathbf{w}^{k-1} \rangle \\ &:= \mathbf{A}^{k-1}E\langle \mathbf{x}^{k-1} \rangle + \mathbf{B}^{k-1}\mathbf{u}^{k-1}. \end{aligned} \quad (\text{A1.3})$$

As a result, the mean of the state at step k predicted from step $k-1$ is written as

$$\mathbf{x}^{k|k-1} = \mathbf{A}^{k-1}\mathbf{x}^{k-1|k-1} + \mathbf{B}^{k-1}\mathbf{u}^{k-1}. \quad (\text{A1.4})$$

Meanwhile, the prediction of covariance commences with the derivation of difference from the predicted state through the substitutions of Equations (A1.1) and (A1.4):

$$\begin{aligned} \mathbf{e}^{k|k-1} &\equiv \mathbf{x}^k - \mathbf{x}^{k|k-1} \\ &= \mathbf{A}^{k-1}(\mathbf{x}^{k-1} - \mathbf{x}^{k-1|k-1}) + \mathbf{w}^{k-1}. \\ &= \mathbf{A}^{k-1}\mathbf{e}^{k-1|k-1} + \mathbf{w}^{k-1} \end{aligned} \quad (\text{A1.5})$$

By definition, the covariance is written in terms of the difference as

$$\begin{aligned} E\langle \mathbf{e}^{k|k-1}\mathbf{e}^{k|k-1^\top} \rangle &= E\langle (\mathbf{A}^{k-1}\mathbf{e}^{k-1|k-1} + \mathbf{w}^{k-1})(\mathbf{A}^{k-1}\mathbf{e}^{k-1|k-1} + \mathbf{w}^{k-1})^\top \rangle \\ &= \mathbf{A}^{k-1}E\langle \mathbf{e}^{k-1|k-1}\mathbf{e}^{k-1|k-1^\top} \rangle \mathbf{A}^{k-1^\top} + E\langle \mathbf{w}^{k-1}\mathbf{w}^{k-1^\top} \rangle. \end{aligned} \quad (\text{A1.6})$$

This results in the prediction of the covariance matrix, which is given by

$$\mathbf{P}^{k|k-1} = \mathbf{A}^{k-1}\mathbf{P}^{k-1|k-1}\mathbf{A}^{k-1^\top} + \mathbf{P}_{\mathbf{x}}^{k-1}, \quad (\text{A1.7})$$

where

$$\mathbf{P}^{k|k-1} \equiv E\langle \mathbf{e}^{k|k-1}\mathbf{e}^{k|k-1^\top} \rangle \text{ and } \mathbf{P}_{\mathbf{x}}^{k-1} \equiv E\langle \mathbf{w}^{k-1}\mathbf{w}^{k-1^\top} \rangle. \quad (\text{A1.8})$$

A1.3 Correction

The correction updates the estimation via measurement, by correcting the mean and the covariance of the elastic constants at step k , $\mathbf{x}^{k|k}$ and $\mathbf{P}^{k|k}$, from the predicted $\mathbf{x}^{k|k-1}$ and $\mathbf{P}^{k|k-1}$ and the measurement at step k , $\bar{\mathbf{z}}^k$. For the mean correction, KF updates the mean by adding a feedback component

$$\begin{aligned} E\langle \mathbf{x}^k \rangle &:= E\langle \mathbf{x}^k + \mathbf{K}^k(\bar{\mathbf{z}}^k - \mathbf{z}^k) \rangle \\ &:= E\langle \mathbf{x}^k \rangle + E\langle \mathbf{K}^k(\bar{\mathbf{z}}^k - \mathbf{C}^k\mathbf{x}^k - \mathbf{v}^k) \rangle, \\ &:= E\langle \mathbf{x}^k \rangle + \mathbf{K}^k(\bar{\mathbf{z}}^k - \mathbf{C}^k E\langle \mathbf{x}^k \rangle) \end{aligned} \quad (\text{A1.9})$$

where \mathbf{K}^k is the so-called Kalman gain. With the output variables \mathbf{z}^k , this results in the generalized representation of the mean correction as

$$\mathbf{x}^{k|k} = \mathbf{x}^{k|k-1} + \mathbf{K}^k (\mathbf{z}^k - \mathbf{C}^k \mathbf{x}^{k|k-1}). \quad (\text{A1.10})$$

Similarly to the prediction, the correction of covariance commences with the derivation of difference through the substitutions of Equations (A1.2) and (A1.9):

$$\mathbf{e}^{k|k} = \mathbf{x}^k - \mathbf{x}^{k|k} = (\mathbf{I} - \mathbf{K}^k \mathbf{C}^k) \mathbf{e}^{k|k-1} - \mathbf{K}^k \mathbf{v}^k. \quad (\text{A1.11})$$

The covariance is expressed in terms of the difference as

$$\begin{aligned} E\langle \mathbf{e}^{k|k} \mathbf{e}^{k|k^\top} \rangle &= E\left\langle \left[(\mathbf{I} - \mathbf{K}^k \mathbf{C}^k) \mathbf{e}^{k|k-1} - \mathbf{K}^k \mathbf{v}^k \right] \left[(\mathbf{I} - \mathbf{K}^k \mathbf{C}^k) \mathbf{e}^{k|k-1} - \mathbf{K}^k \mathbf{v}^k \right]^\top \right\rangle \\ &= (\mathbf{I} - \mathbf{K}^k \mathbf{C}^k) E\langle \mathbf{e}^{k|k-1} \mathbf{e}^{k|k-1^\top} \rangle (\mathbf{I} - \mathbf{K}^k \mathbf{C}^k)^\top + \mathbf{K}^k E\langle \mathbf{v}^k \mathbf{v}^{k^\top} \rangle \mathbf{K}^{k^\top}. \end{aligned} \quad (\text{A1.12})$$

Hence, the covariance matrix is corrected as

$$\begin{aligned} \mathbf{P}^{k|k} &= (\mathbf{I} - \mathbf{K}^k \mathbf{C}^k) \mathbf{P}^{k|k-1} (\mathbf{I} - \mathbf{K}^k \mathbf{C}^k)^\top + \mathbf{K}^k \mathbf{P}_z^k \mathbf{K}^{k^\top} \\ &= \mathbf{P}^{k|k-1} - \mathbf{P}^{k|k-1} \mathbf{C}^{k^\top} \mathbf{K}^{k^\top} - \mathbf{K}^k \mathbf{C}^k \mathbf{P}^{k|k-1} + \mathbf{K}^k (\mathbf{C}^k \mathbf{P}^{k|k-1} \mathbf{C}^{k^\top} + \mathbf{P}_z^k) \mathbf{K}^{k^\top}, \end{aligned} \quad (\text{A1.13})$$

where $\mathbf{P}_z^k \equiv E\langle \mathbf{v}^k \mathbf{v}^{k^\top} \rangle$.

Now, the issue remaining in the correction is the determination of the Kalman gain. The KF, as the linear quadratic estimator, seeks to minimize the expected value of the square of the difference, which is equivalent to minimizing the trace of the corrected covariance matrix

$$\frac{\partial \text{Tr}(\mathbf{P}^{k|k})}{\partial \mathbf{K}^k} = -2(\mathbf{C}^k \mathbf{P}^{k|k-1})^\top + 2\mathbf{K}^k \{ \mathbf{C}^k \mathbf{P}^{k|k-1} \mathbf{C}^{k^\top} + \mathbf{P}_z^k \} = 0, \quad (\text{A1.14})$$

which yields the Kalman gain as

$$\mathbf{K}^k = \mathbf{P}^{k|k-1} (\mathbf{C}^k)^\top \left\{ \mathbf{C}^k \mathbf{P}^{k|k-1} (\mathbf{C}^k)^\top + \mathbf{P}_z^k \right\}^{-1}, \quad (\text{A1.15})$$

The rearrangement of Equation (A1.15) gives

$$\mathbf{K}^k \left\{ \mathbf{P}^{k|k-1} \mathbf{C}^k (\mathbf{C}^k)^\top + \mathbf{P}_z^k \right\} \mathbf{K}^{k^\top} = \mathbf{P}^{k|k-1} (\mathbf{C}^k)^\top \mathbf{K}^{k^\top}. \quad (\text{A1.16})$$

Substitution of Equation (A1.16) into Equation (A1.13) further simplifies the expression of the corrected covariance matrix:

$$\mathbf{P}^{k|k} = (\mathbf{I} - \mathbf{K}^k \mathbf{C}^k) \mathbf{P}^{k|k-1}. \quad (\text{A1.17})$$

Since the operation of KF consists of the recursive usage of the prediction and the correction, the application of KF essentially corresponds to the determination of the system, input and output matrices and subsequently the determination of the Kalman gain and the prediction and correction models.

Appendix 2

Experimental Modules

A2.1 Preprocessing Module

The preprocessing module provides the prior knowledge of the elastic constants and derives the noise properties in each measurement for the energy-based characterization before the specimen is loaded. The module also applies the preparation needed for the specimen and sends out an image of the undeformed specimen, to the full-field measurement module. At time step $k = 0$, the prior knowledge on mean and covariance $\mathbf{q}_M^{0|0}$ and $\mathbf{P}^{0|0}$, are first determined by a knowledge base that can be contributed from any available material database or the knowledge/experience of the user. After providing the prior knowledge for the energy-based characterization, the specimen is prepared by applying a random distribution of black dots on a white background. The necessity of the black and white contrast is required by the full-field measurement module to reliably identify the centroid of each dot from the background. The prepared specimen is then fixed in a testing machine for the next component to perform measurement modeling. Based on the measured force, a finite element model that is created with respect to the boundary conditions is created based on the forces measured from the experiment.

A2.2 Full-field Measurement Module

The full-field measurement module, which mainly consists of the deformation field measurement and boundary displacement identification components, is presented in Figure 52. The first component derives the deformation fields at every image \mathbf{I}^k acquired from the sensing module. In this component, the first task, which is to derive the displacement and strain fields, \mathbf{z}_u^k and \mathbf{z}_e^k at step k , by measuring the centroids from \mathbf{I}^k and compare them with the ones derived from \mathbf{I}^0 , which is captured from the preprocessing module. The full-field strain measurements and the

boundary displacements are bounded by the most outer centroids. The second task extrapolates the field values of \mathbf{z}_u^k and \mathbf{z}_ϵ^k to cover the rest of the unmarked areas, by using a simple polynomial extrapolation algorithm.

The boundary displacement identification component then performs the displacement-field extrapolation via two functions. The first function extrapolates \mathbf{z}_u^k and computes the full-field displacement by applying the extrapolation algorithm. The second function subsequently uses the extrapolated full-field displacement, $\tilde{\mathbf{u}}^k$, to extract the boundary displacement \mathbf{z}_u^k from the deforming boundary. Substitution of \mathbf{z}_u^k and the measured boundary force \mathbf{z}_f^k yields the measured external work z_w^k for the energy-based characterization.

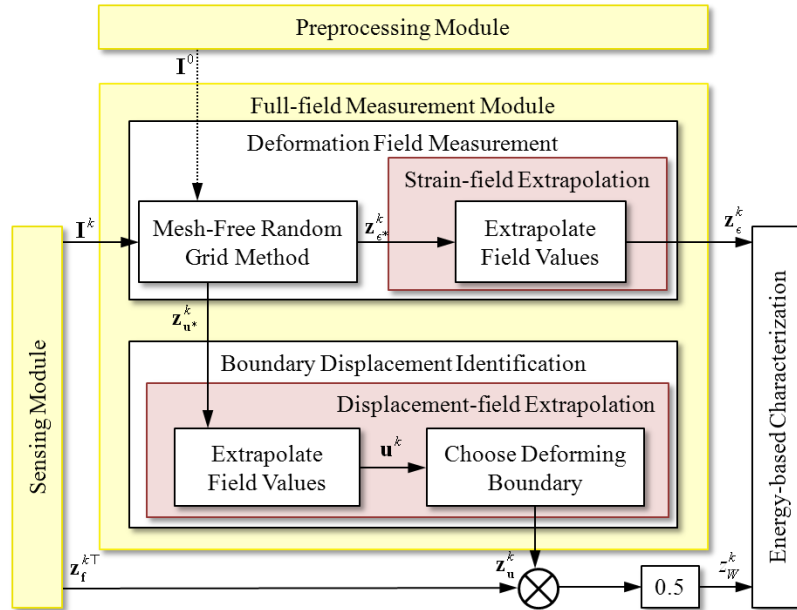


Figure 52 Full-field measurement module in the developed experimental method.